

# **Characterization and Microstructure-based Modeling of Magnetorheological Elastomers**

Mostafa Asadi Khanouki

A Thesis  
In the Department  
of  
Mechanical, Industrial, and Aerospace Engineering

Presented in Partial Fulfillment of the Requirements  
For the Degree of  
Doctor of Philosophy (Mechanical Engineering) at  
Concordia University  
Montreal, Quebec, Canada

March 2021

© Mostafa Asadi Khanouki, 2021

# CONCORDIA UNIVERSITY

## School of Graduate Studies

This is to certify that the thesis was prepared

By: **Mostafa Asadi Khanouki**

Entitled: **Characterization and Microstructure-based Modeling of Magnetorheological Elastomers**

and submitted in partial fulfilment of the requirements for the degree of

DOCTOR OF PHILOSOPHY (Mechanical Engineering)

complies with the regulations of the University and meets the accepted standards with respect to originality and quality.

Signed by the final examining committee:

_____	Chair
Dr. Anjan Bhowmick	
_____	External Examiner
Dr. Norman Wereley	
_____	External to Program
Dr. Ali Nazemi	
_____	Examiner
Dr. Subhash Rakheja	
_____	Examiner
Dr. Sivakumar Narayanswamy	
_____	Supervisor
Dr. Ramin Sedaghati	

Approved by

\_\_\_\_\_  
Dr. Ivan Contreras, Graduate Program Director

March 25, 2021

\_\_\_\_\_  
Dr. Mourad Debbabi, Dean

Gina Cody School of Engineering and Computer Science

# ABSTRACT

## Characterization and Microstructure-based Modeling of Magnetorheological Elastomers

Mostafa Asadi Khanouki, PhD.

Concordia University, 2021.

Multi-functional magnetorheological elastomers (MREs) with magnetic-controlled properties offer great potential for enabling new technologies in a diverse range of industry sectors, such as automotive, aerospace, civil, and biomedical applications. The main objective of this research dissertation is to develop analysis models for magneto-mechanical properties of smart MREs and to propose design optimization strategies to optimally design a novel sandwich beam-type MRE-based adaptive tuned vibration absorber. The dissertation comprises three major interrelated parts. In the first part, a quasi-static microstructure-based model has been proposed to investigate the magneto-elastic properties of MREs. The elastic response of the MREs at zero magnetic field is initially studied by comparing the results of three hyperelastic material models. Then, a microscale model is developed for predicting the quasi-static response of MREs under an external magnetic field. The model considers magnetic interaction between particles distributed in the carrier elastomeric matrix according to regular lattice models for isotropic MREs and according to chain-like structure for anisotropic MREs. Several lattice models are proposed, and performance of each lattice is compared with their counterparts. Detailed explanation is provided on the characteristics of the proposed lattices and on the resulting changes in the microstructure properties of the MREs. The simulation results for different lattice models are then compared with the experimental measurements for both isotropic and anisotropic MRE samples using an advanced rheometer equipped with a magnetorheological (MR) device.

In the second part, the dynamic magneto-mechanical properties of MREs are investigated. For this purpose, a dynamic physic-based model considering the microstructure of MREs is developed to accurately predict the frequency- and field-dependent linear viscoelastic properties of the material. The proposed model considers a cubic particle network in which magnetic particles are located at the junctures and connected with elastic springs. Using Langevin dynamics, the governing equations of motion of particles are derived to evaluate the relaxation spectrum associated with particles' motion in parallel and normal directions with respect to the applied magnetic field. A dipole magnetic saturation model is also implemented to derive the storage and loss moduli of the MREs in terms of frequency and magnetic flux density. The material parameters in the proposed dynamic microstructure-based model have been identified using experimental

tests. For this purpose, oscillatory shear tests were performed using the magneto-rheometer in linear viscoelastic region under a wide range of excitation frequency varying from 2 Hz to 100 Hz in presence of various levels of applied magnetic fields ranging from 0.0 T to 1.0 T. The viscoelastic properties, namely storage and loss moduli of both isotropic and anisotropic MREs, were subsequently measured and compared with those obtained using the developed model to quantitatively evaluate its performance.

The third part of the present dissertation aims to investigate the application of MREs in developing a novel sandwich beam-shaped MRE-based adaptive tuned vibration absorber (MRE-ATVA). An MRE-ATVA comprised of a light-weight sandwich beam treated with an MRE core layer and two electromagnets installed at both free ends is proposed. The MRE-ATVA is designed to have a lightweight and compact structure and the electromagnets provide the magnetic field required to activate the MRE layer while also act as the resonator of the absorber. The finite element (FE) model of the proposed MRE-ATVA and magnetic model of the electromagnets with three different potential designs are developed and combined to evaluate the frequency range of the absorber under varying magnetic field intensity. The results of the developed models are validated in multiple stages with available analytical and simulation data. The developed models are then utilized to formulate the multidisciplinary design optimization problem to maximize the operating frequency range of the MRE-ATVA while respecting constraints of weight, size, mechanical stress, and sandwich beam deflection. The optimization problem is solved combining the gradient based sequential quadratic programming (SQP) technique and stochastic based genetic algorithm (GA) to accurately obtain the global optimum solution. The performance of the optimal MRE-ATVAs with three potential designs are finally compared.

## **Dedication**

*This thesis is dedicated to my mother Nayereh and to my wife  
Haneieh*

for their endless love, support, and encouragement in completion of this work

## **Acknowledgement**

First, I would like to gratefully acknowledge and thank Prof. Ramin Sedaghati for his great supervision and constructive suggestions from the beginning of the thesis as well as providing me continuous support and encouragement throughout the research. I believe that without his advice and guidance this research would not have been possible.

Also, I would like to thank the technical staff, program advisors, and faculty members of the Department of Mechanical, Industrial, and Aerospace Engineering at Concordia University particularly my committee members.

Finally, I would like to express my sincere thanks and gratitude to my wife, my parents, my in-laws, sisters, brothers and friends for their pure love and supports during my studies.

# TABLE OF CONTENT

LIST OF FIGURES .....	x
LIST OF TABLES.....	xiv
NOMENCLATURE .....	xv
<b>CHAPTER 1 : INTRODUCTION AND SCOPE OF THE DISSERTATION .....</b>	<b>1</b>
1.1 Introduction.....	1
1.2 Fabrication and Characterization of MREs .....	2
1.3 Modeling of MREs .....	6
1.4 Application of MREs in Adaptive Tuned Vibration Absorbers .....	9
1.5 Motivation and Objectives .....	11
1.6 Organization of the Manuscript-Based Dissertation.....	13
<b>CHAPTER 2 : EXPERIMENTAL CHARACTERIZATION AND MICROSCALE MODELING OF ISOTROPIC AND ANISOTROPIC MAGNETORHEOLOGICAL ELASTOMERS .....</b>	<b>16</b>
2.1 Introduction.....	16
2.2 Experimental Study .....	17
2.2.1 Fabrication of MRE samples .....	17
2.2.2 Experimental characterization .....	20
2.3 Elastic Response of the Filled Elastomer .....	23
2.4 Quasi-Static Microscale Modeling of Magneto-Mechanical Properties of MREs .....	26
2.4.1 Total potential energy .....	26
2.4.2 Isotropic particle distribution.....	28
2.4.3 Anisotropic particle distribution .....	37
2.4.4 Discussion on the properties of lattices .....	40

2.5 Comparison of Model Results with Experiments.....	45
2.5.1 Isotropic MREs.....	45
2.5.2 Anisotropic MREs.....	52
2.6 Conclusions.....	54

**CHAPTER 3 : ADAPTIVE DYNAMIC MODULI OF MAGNETORHEOLOGICAL ELASTOMERS: FROM EXPERIMENTAL IDENTIFICATION TO MICROSTRUCTURE-BASED MODELING .....55**

3.1 Introduction.....	55
3.2 Magneto-Dynamic Microstructure-based Modeling .....	57
3.2.1 Defining Ideal Distribution of Particles in Cubic Network.....	57
3.2.2 Dynamic Equations of Motion.....	60
3.2.3 Storage and Loss Moduli of MRE.....	72
3.3 Materials and Experimental Methods.....	74
3.3.1 Preparation of MRE Samples .....	74
3.3.2 Microstructure Imaging.....	75
3.3.3 Characterization.....	77
3.4 Results and Discussion .....	78
3.4.1 Dynamic Moduli of Isotropic MREs.....	78
3.4.2 Dynamic Moduli of Anisotropic MREs .....	83
3.5 Conclusions.....	88

**CHAPTER 4 : MULTI-DISCIPLINARY DESIGN OPTIMIZATION OF A NOVEL SANDWICH BEAM-BASED ADAPTIVE TUNED VIBRATION ABSORBER FEATURING MAGNETORHEOLOGICAL ELASTOMER.....90**

4.1 Introduction.....	90
4.2 Configuration of the Proposed MRE-Based ATVA.....	92



4.3 Mechanical and Magnetic Properties of Materials .....	94
4.4 Finite Element Modeling of the Three-Layer Sandwich Beam.....	97
4.4.1 Validation of the developed FE model .....	102
4.5 Magnetostatic Modeling and Analysis of the Electromagnets .....	103
4.6 Multidisciplinary Design Optimization of the Proposed MRE-Based ATVAs.....	107
4.7 Optimization Results and Discussion .....	110
4.8 Conclusions.....	113
<b>CHAPTER 5 : CONTRIBUTIONS, CONCLUSIONS AND RECOMMENDATIONS FOR FUTURE WORKS .....</b>	<b>115</b>
5.1 Major Contributions and Achievements.....	115
5.2 Major Conclusions.....	117
5.3 Recommendations for the future works.....	121
<b>References.....</b>	<b>123</b>
<b>Appendix A.....</b>	<b>133</b>
<b>Appendix B.....</b>	<b>135</b>

## LIST OF FIGURES

Figure 1.1 (a) schematic pictures and (b) microscopic images [18] of isotropic and anisotropic distribution of solid particles in MRE samples .....	4
Figure 1.2 Different cases regarding the direction of the applied magnetic field, particle chains and the direction of the mechanical loading in characterization of MREs [15]. .....	5
Figure 1.3 MRE-ATVAs operating in (a) shear, (b) longitudinal, and (c) squeeze modes [67].....	10
Figure 1.4 Schematic design of a MRE-ATVA operating in squeeze mode [68].....	10
Figure 2.1 Samples 1 to 4 (a) in a cylindrical plexiglass mold in curing stage and (b) after curing.....	19
Figure 2.2 Microstructure images of fabricated MRE samples taken by Confocal microscopy ( $\phi$ is the volume fraction of iron particles); (a) Sample 1, (b) Sample 2, (c) Sample 3, (d) Sample 4, (e) Sample 5, and (f) Sample 6.....	19
Figure 2.3 Left: Rheometer device system used for experimental testing; Right: Closer view of the position of MRE specimen on top of the magneto-rheology accessory.....	21
Figure 2.4 Shear stress versus strain for Samples 1 to 4 at different levels of magnetic flux density; (a) Sample 1 ( $\phi = 5\%$ ), (b) Sample 2 ( $\phi = 15\%$ ), (c) Sample 3 ( $\phi = 25\%$ ), and (d) Sample 4 ( $\phi = 40\%$ ).....	22
Figure 2.5 Experimental and theoretical results of the shear stress versus shear strain for the isotropic MRE samples at zero magnetic field; (a) Sample 1, (b) Sample 2, (c) Sample 3, and (d) Sample 4. ....	25
Figure 2.6 Infinitesimal element of an MRE sample in undeformed (left) and deformed (right) situations under simple shear loading (within x-y plane) and an external magnetic field (along y axis). ....	27
Figure 2.7 Graphical illustration for idealization of particles distribution with structured predetermined particle networks. Left: real isotropic dispersion of particles in an MRE sample, Right: schematic idealized network of particles with exaggerated particle size. ....	28
Figure 2.8 Unit cell of lattice models considered for isotropic distribution of particles.....	29
Figure 2.9 2D (in-plane) view of a network of particles made by placing one unit cell at each corner of the origin (a) SC, and (b) BCC lattices. ....	32
Figure 2.10 Total potential energy density for MRE material with $\phi = 5\%$ under various flux densities assuming particle distribution according to different lattice models; (a) SC, (b) BCC, (c) FCC, (d) ECC, (e) BECC, (f) FECC, and (g) BFECC( $k = 1, s = 1$ ).....	35
Figure 2.11 Comparison of total energy density of the proposed lattices for $\phi = 5\%$ under applied flux density of $B=0.6$ T ( $k = 1, s = 1$ ).....	35
Figure 2.12 Comparison of shear modulus as a function of applied magnetic field for the proposed lattices with $\phi = 5\%$ ( $k = 1, s = 0.3$ ). ....	36

Figure 2.13 Schematic arrangement of particles in (a) isotropic configuration ( $ax_0 = ay_0 = az_0$ ) and (b) anisotropic (chain-like) configuration ( $ay_0 < ax_0 = az_0$ ).	38
Figure 2.14 Total energy density versus strain for different values of $\beta$ under 0.6 T magnetic flux density ( $k = 1, s = 1, \phi = 5\%$ ).	39
Figure 2.15 Total potential energy density versus strain under different levels of applied magnetic flux density and $\beta = 0.9$ ( $k = 1, s = 1, \phi = 5\%$ ).	39
Figure 2.16 Shear modulus versus applied magnetic flux density for different values of $\beta$ ( $k = 1, s = 0.3, \phi = 5\%$ ).	40
Figure 2.17 Two dipoles are located in the 3D space under an external magnetic field.	41
Figure 2.18 A pair of dipoles in three spatial positions; a) dipoles' centerline is parallel to the direction of field ( $\theta=0$ ), b) dipole's centerline is normal to the direction of field ( $\theta= 90^\circ$ ), and c) dipole's centerline is oblique to the direction of field ( $0 < \theta < 90^\circ$ ).	41
Figure 2.19 Value of function $f\theta, R_{12}$ versus distance between two dipoles for the two situations illustrated in Figures 2.18 (a) and (b).	42
Figure 2.20 (a) Change in the sign of function $f$ with the angle $\theta$ between dipoles' centerline and field direction. $f < 0$ means two dipoles tend to attract each other (attraction zone) and $f > 0$ means two dipoles tend to repel each other (repulsion zone). (b) Change in the value of function $f$ with respect to angle $\theta$ .	43
Figure 2.21 Magnetic interaction energy of particle network for MRE with $\phi = 5\%$ arranged according to different lattice types ( $B= 0.1$ T, $k = 1, s = 1$ ).	44
Figure 2.22 Two unit-cells of BCC lattice in undeformed (left) and deformed (right) situations.	45
Figure 2.23 Comparison between the experimental data and model results using SC lattice for four isotropic MRE samples with different volume fraction of particles (a) Sample 1 ( $\phi = 5\%$ ), (b) Sample 2 ( $\phi = 15\%$ ), (c) Sample 3 ( $\phi = 25\%$ ), and (d) Sample 4 ( $\phi = 40\%$ ).	46
Figure 2.25 Error between lattice models prediction, $G_m$ , and experiment data, $G_{exp}$ , for four isotropic MRE Samples 1, 2, 3, and 4.	52
Figure 2.26 Comparison of the model and experimental results of the shear modulus versus magnetic flux density for isotropic (Sample 5) and anisotropic (Sample 6) MREs.	53
Figure 3.1 Ideal arrangement of magnetic particles in (a) equally spaced isotropic configuration (b) chain-like anisotropic configuration.	58
Figure 3.2 Spectrum of eigenvalues, $\lambda$ , in terms of $\theta$ for isotropic dispersion of particles at various magnetic field induction: (a) $\phi = 15\%$ , $G_0 = 31.77$ kPa, and $B = 0.2$ T, (b) $\phi = 15\%$ , $G_0 = 31.77$ kPa, and $B = 0.4$ T, (c) $\phi = 25\%$ , $G_0 = 48.19$ kPa, and $B = 0.2$ T, and (d) $\phi = 25\%$ , $G_0 = 48.19$ kPa, and $B = 0.4$ T.	69
Figure 3.3 Spectrum of eigenvalues, $\lambda$ , in terms of $\theta$ for anisotropic chain-like distribution of particles with $\phi = 15\%$ , $G_0 = 31.77$ kPa, and $B = 0.2$ T, for (a) $\beta = 0.8$ and (b) $\beta = 0.6$ .	70

Figure 3.4 Critical flux density, $B_{cr}$ , in tesla versus anisotropy parameter, $\beta$ , and volume fraction of magnetic particles, $\phi$ (%), ( $s = 1$ ).....	71
Figure 3.5 An element of MRE material under oscillating shear deformation where magnetic field is normal to the shear direction. ....	72
Figure 3.6 Electromagnet device used for applying magnetic field on MRE fabrication mold. ....	75
Figure 3.7. Microstructure images of fabricated MRE samples ( $\phi$ is the volume fraction of iron particles). (a) Sample 1, (b) Sample 2, (c) Sample 3, (d) Sample 4.....	76
Figure 3.8 Left: Different parts of the rotary rheometer used for dynamic characterization; Right: direction of the magnetic field and shear deformation applied on MRE sample. ....	78
Figure 3.9 Results of dynamic moduli obtained from model and experiment for an MRE with $\phi = 15\%$ at several magnetic flux densities; (a) Storage modulus, $G'$ , versus frequency, and (b) Loss modulus, $G''$ , versus frequency.....	81
Figure 3.10 Results of dynamic moduli obtained from model and experiment for an MRE with $\phi = 25\%$ at several magnetic flux density values (a) Storage modulus, $G'$ , versus frequency, and (b) Loss modulus, $G''$ , versus frequency.....	83
Figure 3.11 Results of dynamic moduli in terms of frequency obtained from model and experiments for an anisotropic MRE with $\phi = 15\%$ at several magnetic flux density values; (a) Storage modulus, $G'$ , and (b) Loss modulus, $G''$ .....	86
Figure 3.12 Results of dynamic moduli in terms of frequency obtained from model and experiment for an anisotropic MRE with $\phi = 25\%$ at several magnetic flux density values (a) Storage modulus $G'$ , and (b) Loss modulus $G''$ .....	87
Figure 4.1 Schematic of the proposed MRE-based sandwich beam type ATVA. ....	92
Figure 4.2 Three electromagnet designs considered for the ATVA; (a) H-shaped electromagnet, (b) C-shaped electromagnet, and (c) U-shaped electromagnet. ....	93
Figure 4.3 Schematics of the assembled ATVAs structure with three different electromagnet designs; (a) H-shaped electromagnet, (b) C-shaped electromagnet, and (c) U-shaped electromagnet.....	94
Figure 4.4 Storage modulus in terms of flux density for isotropic MRE sample with 40% volume fraction of CIPs. ....	95
Figure 4.5 The B-H curve of MRF-132DG from Lord Corporation.....	96
Figure 4.6 The B-H curve of 1008 steel.....	97
Figure 4.7 Schematic of the sandwich beam structure with MRE-core layer.....	98
Figure 4.8 Comparison of the results of developed FE model with the analytical results of Mead and Markus [106]. ....	103

Figure 4.9 The H-shaped electromagnet with the path of magnetic flux penetration discretized by letters for magnetic analysis. ....	105
Figure 4.10 Magnetic analysis of the H-shaped electromagnet using FEMM software. ....	106
Figure 4.11 Performance of the SQP method when starting from different initial points. ....	110
Figure 4.12 Frequency shift versus input current for the three optimal MRE-ATVAs. ....	113

## LIST OF TABLES

Table 2.1 Fabricated MRE samples and their constituents .....	18
Table 2.2 Values of parameters of Neo-Hookean, one-term Ogden and two-term $I_1$ -based models.....	24
Table 2.3 Values of constant parameters used in the model. ....	49
Table 2.4 Values of the shear modulus at different magnetic flux densities obtained using different lattice models and comparison with the experimental data. ....	50
Table 2.5 Optimal values of the parameters used in the model. ....	53
Table 2.6 Shear modulus at zero field and the experimental and predicted range of change of modulus. ....	54
Table 3.1 Constituents of the MRE samples. ....	75
Table 3.2 Values of constant parameters for isotropic MREs.....	79
Table 3.3 Average values of coefficient of determination ( $R^2$ ) for isotropic and anisotropic MREs. ....	83
Table 3.4 Values of constant parameters for anisotropic MREs. ....	84
Table 4.1 Comparison of flux density values at the center of the air-gap of the H-shaped electromagnet obtained by analytical magnetic circuit model (Eqs. (4.33) to (4.38)) and FE model. ....	107
Table 4.2 Optimization results of the MRE-ATVA with the three different electromagnets. ....	112

## NOMENCLATURE

<b>Symbol</b>	<b>Definition</b>
$a$	Edge length of the unit cell
$a_x^0, a_y^0, a_z^0, a_0$	Distances between neighboring particles
$A_t, A_c, A_b$	Cross section area of beam layers
$B$	Magnetic flux density
$B_{cr}$	Critical magnetic flux density
$C_{nn}$	Connectivity parameter
$e_{12}$	Potential energy of a dipole pair
$E_{el}$	Elastic strain energy
$E_{diss}$	Dissipative term of the energy
$E_T$	Total potential energy
$E_m$	Magnetic potential energy
$E_t, E_c, E_b$	Elastic modulus of beam layers
$F_n^{(Br)}$	Brownian force on a particle
$F_n^{(Ext)}$	External force on a particle
$[F^e]$	Element force vector
$[F]$	System load vector
$(f)_{B_i}$	Natural frequency at magnetic field $B_i$
$G$	Shear modulus
$G_0$	Shear modulus of elasticity at zero field
$G_m$	Theoretical shear modulus from model
$G_{exp}$	Experimental shear modulus from experiment
$G_{xy}(t)$	Relaxation modulus in x-y plane
$G_{xy}^{(eq)}$	Static shear modulus in x-y plane
$G_{xy}^*(\omega)$	Dynamic complex modulus
$G'_{xy}$	Storage modulus

$G''_{xy}$	Loss modulus
$G''_{f_0}$	Initial loss modulus at starting frequency
$G_c^*$	Complex dynamic modulus of core layer
$G'_c$	Storage modulus of the core layer
$G''_c$	Loss modulus of the core layer
$H_{MRE}$	Magnetic field intensity in MRE
$H_{steel}$	Magnetic field intensity in MRE
$H$	Magnetic field intensity
$H_i$	Magnetic field intensity in section $i$
$h_i$	Thickness of layers
$I_1$	First principal invariant of the right Cauchy-Green deformation tensor
$\hat{I}$	Unit matrix
$I_t, I_b$	Second moment inertia of beam layers
$I_i$	Input current to the coils of section $i$
$J^*$	Model parameter
$J_p$	Particle polarization
$J_s$	Saturation polarization
$k_B$	Boltzmann constant
$K_x, K_y, K_z, K_0$	Elasticity constants of springs
$[K^e]$	Element stiffness matrix
$[K]$	System stiffness matrix
$L$	Lagrangian
$L$	Length of beam
$L_e$	Length of element
$L_i$	Length of section $i$
$\mathbf{m}_i, \mathbf{m}_j$	Magnetic moment of particles (dipoles)
$[M^e]$	Element mass matrix
$[M]$	System mass matrix



$m_p$	Particle mass
$N$	Total number of particles
$N_i$	Number of turns of wire for section $i$
$N_{ut}, N_{ub}, N_w$	Shape functions
$i, j, n$	Subscript indices
$\mathbf{n}, \hat{\mathbf{n}}, \mathbf{k}$	Vector indices in the model
$\tilde{Q}_n$	Generalized force of particle motion
$\mathbf{Q}$	Normal coordinates
$q^e$	Elemental displacement vector
$q^1, q^2$	Nodal displacement vector
$\mathbf{R}_{ij}$	Spatial vector between two dipoles
$\mathbf{R}_i$	Spatial vector of a particle position
$\mathbf{R}_i^0$	Initial space vector of particles position
$r$	Particle radius
$\mathbf{r}_i$	Dimensionless vector of coordinates of particles
$\mathbf{r}_n = (r_{n_x}, r_{n_y}, r_{n_z})$	Particle position vector
$\mathbf{r}_n^{(0)}$	Average value of $\mathbf{r}_n$
$\delta \mathbf{r}_n$	Variation in the value of $\mathbf{r}_n$
$s, k$	Constants of the quasi-static model
$t$	Time
$T(\mathbf{r}_n)$	Kinetic energy of a particle
$\bar{T}$	Absolute temperature
$T_{ax}, T_{tran}$	Axial and transverse kinetic energies
$u_i, v_i, w_i \quad (i = t, c, b)$	Displacement of beam layers
$U_{elast}$	Elastic energy of particle
$U_{magn}$	Magnetic energy of particle
$U$	Total potential energy of particle
$V$	Volume of the sample

$V_t, V_b, V_c$	Strain energy of beam layers
$\nabla U_{magn}$	Gradient vector of magnetic energy
$H_{magn}$	Hessian matrix of magnetic energy
$\mu_i, \alpha_i$	Constants of the elastic response models
$\hat{\beta}$	Loss factor of beam core layer
$\beta$	Anisotropy parameter of particle network
$\boldsymbol{\theta} = (\boldsymbol{\theta}_x, \boldsymbol{\theta}_y, \boldsymbol{\theta}_z)$	Phase shift vector
$\hat{\phi}$	Magnetic flux
$\mu_0$	Vacuum permeability
$\mu_1$	Relative permeability
$\hat{\zeta}$	Number of particles in a unit cell
$\lambda_1, \lambda_2, \lambda_3$	Principal extension ratios (stretches)
$\rho_t, \rho_c, \rho_b$	Density of beam layers per unit length
$\tau$	Shear stress
$\hat{t}, \hat{t}_x, \hat{t}_y, \hat{t}_z$	Relaxation times
$\tau_0$	Minimal relaxation time
$\omega$	Angular frequency
$\phi$	Volume fraction of particles
$\zeta$	Friction coefficient
$\lambda, \lambda_x, \lambda_y, \lambda_z$	Eigenvalues
$v_0$	Volume of particle
$\gamma$	Shear strain

# CHAPTER 1

## INTRODUCTION AND SCOPE OF THE DISSERTATION

### 1.1 Introduction

Intelligent smart fluids and elastomers known as magnetorheological fluids (MRF) and magnetorheological elastomers (MRE), respectively, have received particular attention for the development of semi-active adaptive devices due to their fast response, fail-safe feature and low energy consumption [1]. MRFs consist of dispersion of micron-sized ferromagnetic particles into a fluid carrier such as silicon oil. With the application of an external magnetic field, the suspended ferromagnetic particles become polarized and tend to align along the direction of the magnetic field thus forming clusters of particles in form of chains. The resulting particle chains restrict movement of fluid perpendicular to the magnetic flux direction and thereby yield higher apparent viscosity and yield strength of the fluid. Changes in the rheological behavior of MRFs such as apparent viscosity and yield strength occur instantly and reversibly with the changes in the applied magnetic field, which can be effectively utilized to design adaptive devices with variable damping.

MREs are basically the solid analog of MRFs and are composed of micron-sized ferromagnetic particles dispersed as the filler into a non-magnetic polymeric medium. Carbonyl iron powder (CIP), due to its high saturation limit, and silicon rubber, because of its hyper elastic behavior, are commonly used as magnetizable filler and non-magnetic polymeric medium, respectively. Applying an external magnetic field on the material will magnetize the embedded particles and produce inter-particle magnetic forces. Magnetic interaction between particles results in variation in shape, size, stiffness, and damping of the material. This unique feature of rapid and reversible change in properties, makes MREs a feasible solution for a wide range of technological applications ranging from soft actuators and sensors to medical devices, and high-bandwidth adaptive vibration neutralizer systems [1]–[3]. Although MRFs may provide greater improvement in mechanical properties and MR effect, MREs are less contaminating for the ecosystem and do not have the sedimentation of particles and sealing issues often encountered in MRFs. Moreover, while damping properties of MRFs are mainly affected under the application of an external magnetic field, both the stiffness and damping properties of MREs could be controlled by varying applied magnetic field which makes MREs ideal candidates for the development of next generation of broadband adaptive tuned vibration absorbers and isolators.

Vibration and noise control have been one of the most important concerns in design of structures in automotive, aerospace and marine vehicles and an inseparable part of the engineering research studies since the onset of 20<sup>th</sup> century. The first tuned vibration absorber (TVA) invented by Frahm in 1911 [4] had a simple configuration comprised of mass, spring, and damper elements. Afterwards, several types of TVAs have been proposed by different researchers over many years. Solid viscoelastic materials are passive damping materials that have been widely used for passive TVAs and vibration control applications due to their simplicity, low cost, and ease of installation. The effectiveness of passive vibration absorbers is mainly limited to a specific narrow range of frequency due to the fixed stiffness and damping properties of conventional viscoelastic materials which are identified at the early design stage. Once the working frequency of the primary vibrating system changes with time, passive vibration absorbers may lose their effectiveness and might even cause the amplification of the vibrations due to the mistuned conditions [5]. Alternatively, smart magneto-active elastomers with controllable stiffness and damping properties, offer unique potential to adaptively attenuate the vibration and noise over a broad-band frequency range [6]. Adaptive vibration absorbers having smart magneto-active materials can yield superior vibration attenuation performance compared with passive vibration absorbers. For instance, it is reported in the literature that up to 47% of the structure's acceleration can be reduced by using MRE as the spring element of an adaptive absorber compared to that of a passive absorber using viscoelastic material [7]. Moreover, smart magneto-active elastomer-based structures exhibit greater stability region under different loading conditions compared to devices with passive viscoelastic core layer [8].

The present dissertation mainly aims at investigating the quasi-static and dynamic properties of MREs operating in shear mode using a microstructure approach based on magnetic interaction between particles in the material's microstructure. Viscoelastic properties of MREs, namely storage and loss moduli, are investigated under various loading conditions and different levels of applied magnetic field experimentally. Then, physics-based microstructural models are proposed to predict the magneto-induced quasi-static and viscoelastic dynamic properties of MREs. Finally, the application of the MREs in developing a novel sandwich beam-shaped MRE-ATVA is presented. In the following, a systematic literature review on the pertinent research studies is presented, which is then followed by the motivations, objectives, and organization of the dissertation.

## **1.2 Fabrication and Characterization of MREs**

Fabrication of MRE consists of three major steps, including 1. Mixing of ingredients, 2. Degassing of mixture using vacuum chamber, and 3. Curing the specimens in a mold. In the mixing stage, the polymeric

matrix materials which are initially in fluid phase are blended with the required amount of magnetic particles for a specified time period. Then, the mixture is placed into a vacuum chamber to remove the air bubbles trapped inside the mixture. Finally, the product is transferred into a desired mold to be cured.

The curing process could be done in absence or presence of the applied magnetic field. Curing the mixture in the absence of magnetic field will result in isotropic/non-oriented MRE in which the magnetic particles have been uniformly distributed inside the matrix [9]. Applying magnetic field during the curing before the crosslinking phase of the carrier matrix causes the magnetic particles to form a chain-like structure inside the elastomeric matrix and produce anisotropic/oriented MRE [10], [11]. Figure 1.1 shows the schematic and microscopic images of isotropic and anisotropic distribution of solid particles within the matrix of MRE samples. It should be noted that the curing could happen at room temperature or at higher temperatures in an oven, the latter will accelerate the curing process and the MRE would require less time to solidify.

The type and spatial distribution of magnetizable particles inside the elastomeric matrix are among the most important parameters that affect magneto-mechanical properties of MREs [12]. Magnetic particles of various shapes and sizes are used in the fabrication of MREs. Spherical micron-sized CIPs with narrow hysteresis loop is one of the most common ferromagnetic material for this purpose. Soft magnetic behavior and spherical shape of such particles facilitate the dispersion of particles within the host polymer. Several studies have experimentally investigated the influence of particles shape, size, loading percentage, and distribution on the properties of MR materials such as viscoelastic and magnetostriction properties and MR effects [13]–[17].

Lu et al. [13] have investigated the rheological and mechanical properties of isotropic and anisotropic MRE composites containing micron-sized CIPs and poly (styrene-ethylene-butylene-styrene) (SEBS) tri-block copolymer utilized as the thermoplastic matrix rubber. Larger shear modulus was observed for both isotropic and anisotropic composites compared to the pure SEBS matrix not only in the presence of magnetic field but also in the absence of magnetic excitation. The increase of modulus at zero magnetic excitation was explained as a result of the filler effect in the matrix (including uniformly dispersed CIPs in isotropic samples and aligned chain-like structure of the particles in anisotropic samples). Meharthaj et al. [16] have studied the effect of the size of spherically shaped particles on the properties of the MR gels prepared using magnetite ( $\text{Fe}_3\text{O}_4$ ) nanoparticles and/or carbonyl iron (CI) micro-particles dispersed in a polymer gel. The results indicated an increase in the storage modulus and saturation magnetization of the prepared samples of magnetic gel with the decrease in the size of the particles. The experiments revealed an increase in the storage modulus up to 28% for the MR gels prepared with 20% by weight of magnetite nanoparticles.

Under high strength magnetic field, magnetizable particles become magnetically saturated, beyond which, no further change in the properties can be achieved by increasing the magnetic field. The extent of variation in the material properties from zero magnetic excitation up to magnetic saturation is typically called the MR effect which is another important feature of MREs. MR effect depends on several factors such as concentration of iron particles, distribution and orientation of particles, physical properties of matrix material, and magnetic properties and percentage of filler particles [12], [18]–[20].

Recently, dot-patterned MREs have been fabricated using 3D printing technology without applying a magnetic field during the fabrication process [21]–[23].

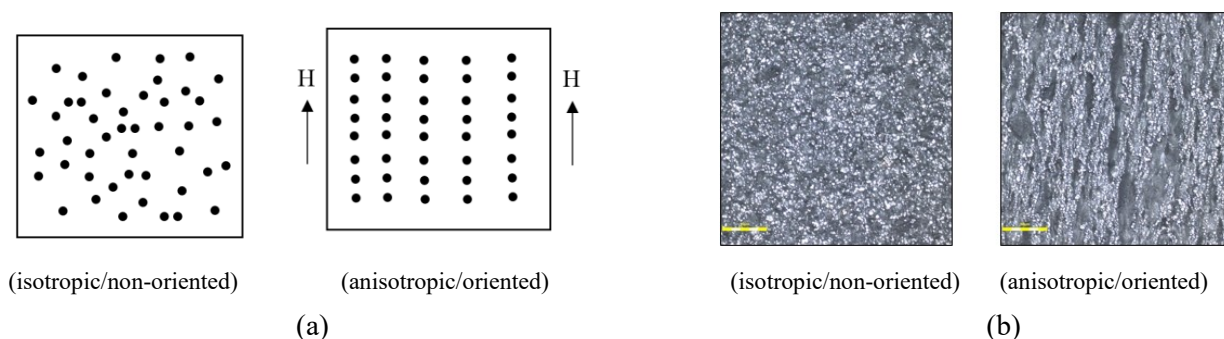


Figure 1.1 (a) schematic pictures and (b) microscopic images [18] of isotropic and anisotropic distribution of solid particles in MRE samples.

Variation in MRE properties, particularly in the stiffness and damping, under an applied magnetic field can be characterized using different experimental testing devices such as servo-hydraulic material testing machine [24], dynamic mechanical analyzer (DMA) [13], and rheometers [25]. Testing might be performed in different modes of mechanical excitation including uniaxial tension and compression [26], translational shear [9], rotational shear [27], or a combination of these modes [28], [29]. While under quasi-static mechanical loading and an applied magnetic field, MREs generally behave like hyperelastic materials with linear/nonlinear magneto-elastic response, MREs show a strong magneto-viscoelastic response under dynamic loading which is observable from the hysteresis loops [1], [27].

Many research studies have been conducted on experimental characterization of MREs under various excitation modes under low frequency quasi-static [30], [31] or dynamic loading [25], [32]–[34] conditions. At low frequency quasi-static conditions, Coquelle et al. [35] obtained the stress-strain curves in a quasi-static tension test for elastomers filled with iron powders arranged in isotropic and anisotropic distribution. The elastic modulus of the samples with chain-like arrangement of particles was 750 kPa while for the isotropic samples was found to be 370 kPa. Varga et al. [15] investigated the effect of particle concentration and distribution, and magnetic field intensity on the improvement of field-induced elastic modulus. They

showed both the magnetic field and volume content of iron particles have a considerable impact on the improvement of the elastic modulus. They considered several cases depending on the direction of the applied magnetic field, the direction of particle chains, and the direction of the applied force as illustrated in Figure 1.2. The most significant MR effect was found to occur for anisotropic sample where the direction of the field is parallel to the particle alignment and to the direction of the mechanical loading. Bodelot et al. [30] have studied the magneto-mechanical properties of fabricated MRE samples using a dedicated experimental setup. The custom-designed test setup is able to bring the sample in the field and allows for the application of low rate cyclic tensile loadings while monitoring in-situ mechanical and magnetic quantities. The experiments revealed that isotropic samples exhibit significant magnetostriction along the direction of the applied field while samples with field-structured particles experience insignificant magnetostriction.

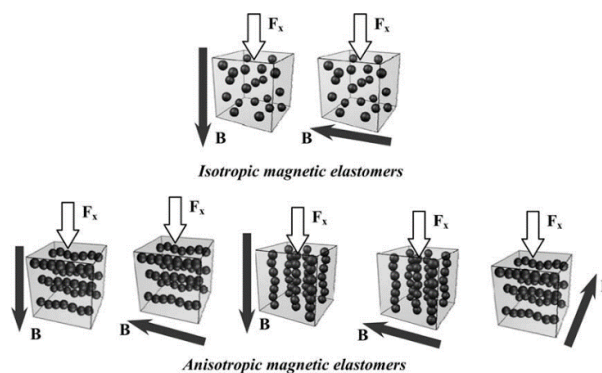


Figure 1.2 Different cases regarding the direction of the applied magnetic field, particle chains and the direction of the mechanical loading in characterization of MREs [15].

Experiments under quasi-static excitation are useful to determine some mechanical properties of MREs such as magneto-hyperelasticity and also to develop modeling approaches for estimation of the MR effect. However, due to working conditions in most practical applications, dynamic loading is much closer to the real situation of excitations [36]. As an early research work in this area, Ginder et al. [37] developed MREs made of CIPs embedded in natural rubber to show the ability of increasing the dynamic storage and loss moduli under applied magnetic field. By applying shear harmonic deformation on the samples, they showed that both stiffness and damping can be increased by increasing the magnetic flux density. Gong et al. [32] studied the relationship between microstructure and dynamic mechanical properties of the isotropic MREs by altering the percentage of the constituents in the fabrication process. For a sample composed of 70 wt% iron particles, 20 wt% silicone oil, and 10 wt% silicone rubber, a considerable increase in the storage modulus (51%) was achieved at the resonance frequency of the sample.

Li et al. [27] studied the viscoelastic properties of MREs by applying harmonic loading under various strain amplitudes and frequencies via a parallel plate rheometer device. For strain amplitudes under 10% and

the frequency under 10 Hz, the stress-strain curves of the anisotropic samples showed fully elliptical loops, which represents a linear viscoelastic behavior. The magneto-mechanical properties of MREs with thermoplastic elastomer matrix containing 60  $\mu\text{m}$  iron particles of irregular shape was also studied by Kaleta et al. [33] using cyclic shearing load along with the applied magnetic field intensity up to 100 kA/m. They considered change in the area of the hysteresis loops and stress amplitude as an indication of the MR effect which is shown to be larger for the anisotropic samples. Dargahi et al. [9] have conducted extensive experimental characterization on six isotropic MRE samples in shear mode. Using a table top Bose Electro-Force test system equipped with arrangement of permanent magnets, they experimentally evaluated static characteristics as well as dynamic properties of the MRE samples. They applied up to 450 mT magnetic flux density and reported around 1700% increase in the storage modulus.

### 1.3 Modeling of MREs

Along with the experimental characterization, development of models that could accurately predict the response of MREs as a function of applied magnetic field, driving frequency, strain amplitude and other operating and environmental conditions, is of paramount importance in utilization of MREs in practical adaptive devices. These models once validated can practically replace costly and time-consuming experimental tests and thus provide essential guidance for design optimization of MRE-based adaptive devices [38], [39].

There are generally three types of modeling techniques for the MREs namely continuum-based, phenomenological, and microstructure-based modeling approaches. In continuum mechanics approach, the MRE is assumed to be a continuous medium in which the effect of iron particles is smeared into the elastomeric carrier. The macroscopic behavior of this continuous medium is then studied using the coupled equations of elasticity and magnetism, based on the physical principles of continuum mechanics, hyperelasticity, viscoelasticity and magnetism [40]–[47]. For instance, Borcea and Bruno [45] have used minimum energy principle of magneto-elasticity to study the macroscopic behavior of composite elastomers with isotropic dispersion of magnetic particles. They obtained the overall deformation and stress-strain relations through complex mathematical formulations. Dorfmann and Ogden [43] have derived the constitutive relations for magneto-sensitive elastic solids and applied them for a special case of circular cylindrical sample under a radial magnetic field and subjected to axial shear deformation. The model showed the effect of the magnetic field in stiffening the shear response of the material but it was unable to predict the saturation of the shear stress at higher fields. Brigadnov and Dorfmann [42] have also used a simple strain energy function to find a closed form solution for the Cauchy stress function followed by the calculation of



the shear stress for an isotropic MRE under simple shear deformation. They compared the results of mathematical modeling with experimental data and obtained an acceptable agreement.

The phenomenological or parametric-based models may be described as a specific configuration of spring and damper elements which are used to represent damping and stiffness of the MRE materials. Different studies have investigated the performance of parametric models in predicting the viscoelastic response of MREs [24], [27], [48]–[50]. Li et al. [27] used a four parameter spring-dashpot viscoelastic model to find the storage and loss moduli of a MRE. They used the experimental data generated by a parallel plate rheometer to identify the stiffness and damping parameters of the model through curve-fitting process. The parameters were then obtained for different magnetic flux densities to predict the hysteresis loops and storage and loss moduli. Chen and Jerrams [50] presented a parametric model which took into account the nonlinear viscoelastic effects in the dynamical properties of MREs as well. They considered three parts in their model, i.e. a standard linear model, a stiffness variable spring, and a spring-Coulomb friction slider to account for viscoelasticity of the polymer composite, magnetic field-induced properties, and the interfacial slippage between the matrix and particles, respectively. Unlike the other parametric models, this model considered also the volume fraction of particles in the second part of the model. Norouzi et al. [24] introduced a modified Kelvin-Voigt model including five parameters in the formulation of shear storage modulus and viscosity of the MRE. Modulus and viscosity were written as functions of strain frequency, strain amplitude, and magnetic flux density using the unknown parameters. The unknown parameters were then calculated by a nonlinear regression method of minimizing the error between experimental and theoretical results.

While parametric viscoelastic models could not consider the difference in arrangement of particles for isotropic and anisotropic MRE samples, microscale models which are based on the microstructure of MREs can address the isotropic or anisotropic distribution of particles in the host matrix. This modeling approach considers magnetic interaction between embedded magnetic fillers and their corresponding effect on the polymeric matrix which is the main reason behind the change of properties under an applied magnetic field. Several attempts have been made since the last decade of 20<sup>th</sup> century to develop and improve microstructure-based modeling approach. Jolly et al. [51], [52] presented a quasi-static dipole model to predict field-induced elastic modulus of anisotropic MREs. By considering magnetic interaction between two adjacent dipoles (magnetized particles inside the material), they obtained a formula for field induced shear modulus as a function of the applied magnetic field density, and iron particles concentration. Based on the previous progresses in the modeling of MR fluids [53], [54], Davis [55] presented a model based on interaction of dipoles to predict the mechanical behavior of MREs with/without the presence of a magnetic field. The Ogden strain potential was utilized to express elastic properties of an unfilled elastomer. Then a finite element

method based on a previous work [53] was utilized to predict shear modulus of a filled elastomer in the absence of a magnetic field. Finally, a relation was presented to predict maximum increase of shear modulus (once saturation of MRE is occurred) as a function of saturation magnetization and volume fraction of filler particles. The optimum volume fraction of iron particles was reported to be 27% to achieve the maximum relative MR effect. The model proposed by Davis [55] has also been used in some other studies to obtain the operating frequency range of the MRE-based devices [56], [57].

In the studies performed by Jolly et al. [51], [52] and Davis [55], magnetic interactions between only two adjacent particles have been considered which is far from the real situation. Later, some researchers have tried to develop models capable of considering interactions of all particles in a chain [31] or between multiple chains [58]. Shen et al. [31] have proposed a quasi-static model for predicting stress-strain curves of MREs made of polyurethane and natural rubber matrix materials. The model assumes a chain-like distribution of magnetic particles and takes into account the dipole interactions between all particles in a chain. The total stress developed in the MRE is then assumed to be due to two sources. One due to mechanical interaction of particles and matrix at zero magnetic field, and the other due to magnetic interaction between dipoles in a chain. The developed model could be used only at low magnetic fields since it cannot predict properties near saturation region.

In more recent researches, some regular or periodic structures have been used as idealized spatial dispersion of particles in the matrix to analyze magnetostriction effect or mechanical properties of MREs [59]–[61]. In a series of publications Ivaneyko et al. [62]–[64] proposed a microstructure model for investigation of magnetostriction phenomenon and magneto-elastic properties of both isotropic and anisotropic MREs, called magneto-sensitive elastomers (MSEs) in their study, by considering interactions between all the particles in the network. They used three lattice models i.e. simple cubic (SC), body-centered cubic (BCC), and hexagonal close-packed (HCP) to represent arrangement of particles [62] and also expressed magnetic energy as a function which depends on the spatial distribution of particles (lattice type). The total energy is finally defined as the summation of elastic energy of host matrix and magnetic energy of particle network. The stress and modulus of MRE are subsequently calculated by taking derivation of the energy function. Based on their theoretical results [62], the elastic tensile modulus of isotropic MREs based on SC and BCC lattice models decreases with the applied magnetic field, which is obviously in contradiction with experimental observations. Ivaneyko et al. [65], [66] have also worked on a coarse-grained dipole-spring network model which takes into account the influence of interactions between magnetic particles on the dynamic-mechanical properties of magneto-sensitive elastomers with isotropic and anisotropic distribution of particles. In their model, the particles are assumed as beads located at the joints of the cross-links and

arranged in a cubic network. Particles are connected by elastic springs where each particle has a friction coefficient. The motion of particle network is formulated to find the frequency-dependent storage and loss moduli of MREs in terms of the particle magnetization, particle volume fraction, and the polymer matrix elasticity.

#### **1.4 Application of MREs in Adaptive Tuned Vibration Absorbers**

The applications of MRE devices with adjustable stiffness are vast ranging from construction, aerospace, automotive to biomedical industries [1], [67], [68]. A semi-active adaptive tuned vibration absorber which uses MREs as tunable viscoelastic elements is named here as MRE-ATVA. While a passive tuned vibration absorber (TVA) is a simple and reliable way to attenuate vibration around a specific tuned frequency, an MRE-ATVA can adaptively change its natural frequency in response to the change in external excitations due to unpredicted environmental conditions and thus can effectively attenuate vibration over a broad frequency range.

Over the years, various MRE-based adaptive vibration absorbers, isolators, and dampers have been proposed by researchers. Lerner and Cunefare [69] designed three types of MRE-ATVAs working in shear, squeeze, and longitudinal modes as shown in Figure 1.3. For the shear mode, the direction of mechanical excitation is perpendicular to the direction of applied magnetic field, whereas they are parallel in the compression and squeeze working modes. In this work, the absorber devices were aimed to be used as tuned vibration absorbers for ATR 42 and 74 aircraft fuselages. Results suggested that the squeeze mode device has the largest frequency range of 57-347 Hz under the applied magnetic field intensity ranging from 0kA/m to 20 kA/m.

Sun et al. [70] designed and prototyped a squeeze working mode MRE-ATVA. Schematic of this absorber and its components are illustrated in Figure 1.4 in which red arrows represent the direction of the generated magnetic field which is parallel to the direction of mechanical excitation. The modulus of the MRE and subsequently the natural frequency of the absorber vary by changing the strength of the applied magnetic field. The natural frequency of the designed squeeze mode MRE-ATVA was reported to vary from 37 Hz to 67 Hz by changing the magnetic field intensity from 0 kA/m to 250 kA/m, respectively.

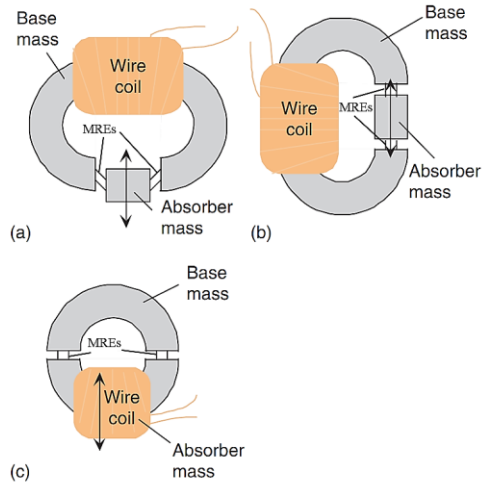


Figure 1.3 MRE-ATVAs operating in (a) shear, (b) longitudinal, and (c) squeeze modes [69].

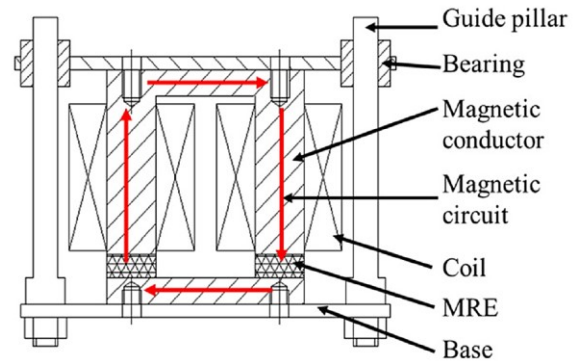


Figure 1.4 Schematic design of a MRE-ATVA operating in squeeze mode [70].

Sun and coworkers [71] have also designed, fabricated, and tested two MRE-ATVAs working in squeeze and shear modes. Results showed that the squeeze working mode absorber has a larger range of tunable natural frequency (62 to 127 Hz) than that of the shear mode absorber (32 to 62 Hz). In another work [56], they have introduced a multilayered MRE dynamic vibration absorber which can operate at low frequencies in the range of 3.2 Hz to 19 Hz. A MRE-based dynamic vibration absorber was also introduced by Xin et al. [72] for powertrain mount systems of automobiles. This device consists of a vibration absorption unit, which uses MRE as a spring with variable stiffness and a passive vibration isolation unit which includes a rubber spring.

Chen et al. [38] proposed a method for design and optimization of a bearing that contains laminated MREs. Their model integrates MRE material parameters into the magneto-mechanical characteristics of the bearing components. After analytical modeling and optimization, a laminated MRE bearing with four layers of MRE was fabricated and tested with MTS test bench in shear mode. Using MRE samples incorporating 11% volume fraction of iron particles, the best performance of the laminated MRE bearing i.e. the maximum adjustable range of stiffness for the bearing was achieved under input power of 58.5 W. Yang et al. [28] presented a compact MRE isolator capable of working in shear and compression modes simultaneously using two pieces of MREs in the structure. The shift of the stiffness coefficient of this mixed mode isolator device (329.63%) was significantly higher in comparison with a similar single shear mode isolator (17.57%) [73]. A recent detailed review on MRE devices have been also provided in Ref. [36].

## 1.5 Motivation and Objectives

While phenomenological and parametric-based modeling of field-dependent properties of MREs under quasi-static and dynamic loadings have been widely studied, very limited number of studies have been conducted on the modeling of MREs' magneto-mechanical properties using microstructure-based theories capable of addressing the distribution of particles in MREs and explaining their microstructure properties. These models are of paramount importance as they not only can provide physical insight to investigate the effect of magnetic particles and their arrangements on physical properties of MREs, but also, can be effectively utilized to design MREs with enhanced properties, rather than conducting expensive ad-hoc experimental tests. As discussed in Section 1.3, Ivaneyko et al. [62], [64] provided a basis to describe the relation between the microstructure of MREs and their mechanical properties in quasi static loading condition. However, the lack of explanation on different characteristics of the proposed lattice models makes it difficult to understand the physical interpretation of the relation between particles distribution and changes in the modulus of MRE under magnetic induction. They also investigated the elastic shear response of MREs with isotropic, chain-like and layer-like arrangement of particles [64], however, the proposed formulation describes the shear modulus as a function of samples' magnetization and could not explicitly relate the modulus to the applied magnetic flux density which is necessary for any practical application.

In the case of dynamic properties, generally, theoretical description of the dynamic behavior of polymers is a complicated task as the dynamic properties depend strongly on the structure of the polymer chains [74], [75]. This becomes even more complex for the composite polymers containing magnetic particles considering the magnetic interaction of particles as well as the viscoelastic interactions between polymeric chains. While the coarse-grained network model proposed by Ivaneyko et al. [65], [66] can describe the dynamics of magneto sensitive elastomers from a microscale basis, the formulated dynamic moduli in terms of particles magnetization cannot be directly measured in practice; thus, hindering the practical realization of the model. Moreover, magnetic saturation of MREs occurred by the increase of magnetic field intensity has not been addressed in the formulation and the model can only be used for a limited range of the applied magnetic field.

Moreover, while MREs application in various areas including biomedical [2], [76], automotive [72], [77], and specifically for ATVAs [57], [68] have been investigated through the years, there are limited studies focused on the multidisciplinary design optimization of the MRE-based devices in order to maximize their operating range. In this subject, research studies on the MR vibration absorber devices employing continuous sandwich structures are very limited. Particularly, no studies have been reported on the development of design optimization strategies for these MRE-based sandwich adaptive devices. Hirunyapruk et al. [78] proposed a three-layer beam-like tuned vibration absorber which was treated with MRF in the core layer. Two

electromagnets were considered on the beam to provide the required magnetic field on the MRF layer. They showed that the natural frequency of the device could vary from 106 to 149 Hz. While this work is very useful for demonstrating the feasibility and operation of MRF beam-like absorber devices, the optimal design problem of the absorber has not been addressed. To the best of our knowledge, there have been no study conducted on the development and multidisciplinary design optimization of adaptive vibration absorbers featuring multilayer MRE-based sandwich structures.

Although considerable research work has been conducted on development of MREs, constitutive models for MREs, and MRE-based vibration absorbers as discussed in the previous sections, however, the topic is still in its infancy and much work is required to advance this enabling technology. The present research advances the state of knowledge on the MREs by proposing microstructure-based models in both quasi-static and also dynamic loading conditions which are validated using experimental data obtained by examining the in-house prepared MRE samples. Moreover, a novel sandwich beam-shaped adaptive tuned vibration absorber is developed and the design optimization problem is formulated and solved to obtain an optimal adaptive vibration absorber with wide-bandwidth and adaptable frequency range.

Considering the research gap, the specific objectives considered for the present dissertation are summarized as follows:

- i. Comparing the performance of three hyperelastic theories, i.e. Neo-Hookean, one term Ogden model, and a two term  $I_1$ -based model in presenting the zero-field elastic response of the prepared MREs.
- ii. Investigating different types of lattice models representing the distribution of magnetic fillers in the polymeric matrix. Studying the quasi-static magneto-mechanical properties of MREs and obtaining the elastic shear modulus of MREs in terms of external magnetic flux density and particle participation using an energy approach for both of isotropic and anisotropic MREs. Validating the performance of the model in predicting the elastic shear modulus by comparing the results with those measured experimentally. Evaluating the efficiency of the selected lattices quantitatively by comparing their performance in prediction of experimental results.
- iii. Improving the coarse-grained network models by deriving a frequency- and magnetic flux-dependent microstructure-based model for predicting the dynamic moduli of MREs in a broad range of excitation frequency and magnetic field up to the saturation point. Validating the dynamic model with experimental results for several isotropic and anisotropic MRE samples with different volume fraction of solid particles.

- iv. Proposing three different novel configurations for sandwich beam-shaped MRE-ATVA. Developing a finite element model of the proposed MRE-ATVA and magnetic model of the three types of electromagnets. Developing a multidisciplinary design optimization framework to maximize the frequency bandwidth of the MRE-ATVA under constraints of mass, maximum stress, and static deflection.

## 1.6 Organization of the Manuscript-Based Dissertation

The present dissertation is prepared in manuscript-based format following the instruction described in “Thesis Preparation and Thesis Examination Regulation” booklet of the School of graduate Studies of Concordia University. The dissertation includes five chapters which address the objectives outlined in Section 1.5.

Chapter 1 presents an introduction to the research dissertation including the introduction on MR materials and their features and applications, literature review, motivations and objectives, and organization of the dissertation. Thereafter, Chapters 2, 3, and 4 are presented based on the three articles that are extracted from this research dissertation. All these articles have been published in high ranked and prestigious scientific journals. These chapters are organized in sequential manner which describe the methodologies to address the objectives of the dissertation and discussion on the obtained results. Finally, the main conclusions extracted from the research dissertation are summarized in the Chapter 5 together with recommendations for the future works. It should be mentioned that some repetitions in the developed formulations and the experimental study in some chapters cannot be avoided since they are required to present the integrity of the articles and to illustrate the entire developed methodology. In the following, the summary of each chapter is presented.

Chapter 2 presents the following article published in the “Journal of Composites Part B: Engineering”:

Asadi Khanouki M., Sedaghati R., and Hemmatian M. "Experimental characterization and microscale modeling of isotropic and anisotropic magnetorheological elastomers." *Composites Part B: Engineering*, 176 (2019): p. 107311.

In this article, a systematic study is conducted on the sample preparation, characterization and microscale modeling of MREs with isotropic and anisotropic particle distributions in quasi-static condition. Different MRE specimens with silicone rubber as the matrix material and varying content of carbonyl iron particles as magnetizable fillers are fabricated. The quasi-static properties of the samples are characterized experimentally using an advanced rheometer equipped with a MR device. The elastic response of the MREs at zero magnetic field is first investigated theoretically and experimentally. A microscale modeling approach

is then used for predicting the response of the MREs under an external magnetic flux density. The approach is based on the idealized distribution of particles inside the matrix according to the regular lattice models or chain-like structure for isotropic and anisotropic particle dispersions, respectively. Several lattice types are proposed, and performance of each lattice is compared with their counterparts. Detailed explanation is provided on the behavior of the proposed lattices and changes in the properties of the MREs are described from the microstructure point of view by considering the magnetic interaction between particles. The performance of different lattice models are quantitatively demonstrated by comparing the model results with the experimental data for both isotropic and anisotropic MRE samples.

Chapter 3 presents the following article published in the “Journal of Material Science and Engineering B”:

Asadi Khanouki M., Sedaghati R., and Hemmatian M. "Adaptive Dynamic Moduli of Magnetorheological Elastomers: from Experimental Identification to Microstructure-based Modeling." *Journal of Material Science and Engineering B*, 267 (May 2021): p. 115083.

This research paper aims at the development of a dynamic physic-based model considering the microstructure of isotropic and anisotropic MREs to accurately predict their field-dependent viscoelastic properties. A cubic network in which magnetic particles are located at the junctures and connected with elastic springs has been utilized to derive the dynamic governing equations of motion of the particles to evaluate their relaxation spectrum while moving parallel and normal to the field direction. A dipole magnetic saturation model is subsequently implemented to derive the field-dependent dynamic storage and loss moduli of the MREs. An experimental test has also been designed to identify few constant material parameters in the model and also to validate the developed model. Isotropic and anisotropic MRE samples with 15% and 25% volume fraction of particles are fabricated and the isotropic and anisotropic distribution of particles in the matrix are verified through microstructure images. MRE samples are subsequently tested under oscillatory torsional shear mode using an advanced rotary rheometer in a wide range of excitation frequency varying from 2 Hz to 100 Hz and magnetic fields up to 1 T. Results for storage and loss moduli are finally compared with those of experiment in a wide range of excitation frequency and magnetic field up to the saturation. It has been shown that there is a good agreement between experiment and theoretical results. The developed model can provide essential guidance for the development of high-bandwidth MRE based adaptive devices at early stages of design.

Chapter 4 presents the following article published in the “Journal of Materials”:



Asadi Khanouki, M.; Sedaghati, R.; Hemmatian, M. "Multidisciplinary Design Optimization of a Novel Sandwich Beam-Based Adaptive Tuned Vibration Absorber Featuring Magnetorheological Elastomer." *Materials* 13 (2020): p. 2261.

This study concerns with investigating the dynamic performance and design optimization of a novel MRE-ATVA. The proposed MRE-ATVA consists of a light-weight sandwich beam treated with an MRE core layer and two electromagnets installed at both free ends. Three different design configurations are proposed for the electromagnets including U-shape, H-shape, and C-shape designs. The finite element (FE) model of the proposed MRE-ATVA and magnetic model of the electromagnets are developed and combined to evaluate the frequency range of the absorber under varying magnetic field intensity. The results of the developed model are validated in multiple stages with available analytical and simulation data. A multidisciplinary design optimization strategy has been formulated to maximize the frequency range of the proposed MRE-ATVA while respecting constraints of weight, size, mechanical stress, and sandwich beam deflection. The optimal solution is obtained and compared for the three proposed ATVA configurations. The optimal ATVA with a U-shaped electromagnet shows more than 40% increase in the natural frequency while having a total mass of 596 g.

## CHAPTER 2

# EXPERIMENTAL CHARACTERIZATION AND MICROSCALE MODELING OF ISOTROPIC AND ANISOTROPIC MAGNETORHEOLOGICAL ELASTOMERS

### 2.1 Introduction

MREs are smart elastomeric materials with controllable mechanical and viscoelastic properties through the application of external magnetic field. MREs essentially consist of micron-sized ferromagnetic particles dispersed into a non-magnetic polymeric medium. Different types of filler particles and host matrix material could be used in fabrication of MREs that will obviously results in different final properties [12], [79]. Once a magnetic field is applied, the stiffness and damping of the material changes within a few milliseconds as a result of magnetic interaction between the filler particles. MREs are utilized as the adaptable viscoelastic element in a range of applications such as adaptive vibration absorbers[69], [80], seismic isolators [7], [81], automotive suspension [72], [77], sensing devices and actuators [82], [83] to name a few. Many research studies have been conducted in the past on fabrication, experimental characterization, and modeling of quasi-static properties of MREs [13]–[17], [31], [39], [51], [55]. The proposed modeling methods in the literature as addressed in Chapter 1 are either applicable only for a limited range of magnetic flux density thus unable to predict the magnetic saturation or suffer from the lack of physical understanding between the microstructure and magneto-mechanical properties. Therefore, accurate physic-based models are required to accurately analyze the variation in the properties of MRE samples with different constituents and under wide range of applied magnetic field.

In the present chapter, quasi-static properties of MREs are analyzed theoretically and experimentally. A microscale model is presented which considers a complete set of different types of lattice models to represent the distribution of magnetic fillers in the matrix. For the isotropic MREs, seven lattices are considered including simple cubic (SC), body centered cubic (BCC), face centered cubic (FCC), edge centered cubic (ECC), body & edge centered cubic (BECC), face & edge centered cubic (FECC), and body & face & edge centered cubic (BFEC). Such a comprehensive investigation of lattice models has not been covered in any research study yet. For the anisotropic MREs, chain-like structure of particles is used as idealized dispersion. Shear modulus of MREs is obtained in terms of external magnetic flux density via an energy approach for the idealized distribution of particles according to the considered lattices for both isotropic and anisotropic cases. With the results taken from the model, different characteristics of the proposed lattices are explained with in-depth physical and mathematical discussion based on magnetic interaction of particles in the network.

This physical explanation clarifies the microstructure-property relationship for the smart MRE materials which cannot be well understood from the discussions presented in the literature. The results of shear modulus from model are also compared with the experimental data and the efficiency of the selected lattices are evaluated quantitatively by comparing the resulting error values of each lattice.

In the following, first the experimental study related to fabrication of different types of isotropic and anisotropic MRE samples using two types of silicone rubber matrix and varying contents of ferromagnetic particles is presented. Samples are then characterized experimentally in rotational shear mode using advanced rotary rheometer equipped with an MR device. The influence of magnetic field intensity, particles content, and particles arrangement on the mechanical properties of MREs are thoroughly investigated and discussed. Then, the performance of three hyperelastic theories, including the Neo-Hookean, one term Ogden model, and a two term  $I_1$ -based model in presenting the shear stress-strain curves of the prepared elastomeric composites at zero magnetic field are evaluated. The selected model is subsequently combined with field-dependent microscale model to predict magneto-mechanical response of MREs under applied magnetic field. A particle saturation model is employed that relates the magnetization of particles to the applied magnetic flux density. As a result, shear modulus is calculated as a function of magnetic flux density from low field up to high field values where magnetic saturation occurs. Results of this chapter clearly describes the quasi-static behavior of MREs with respect to the applied magnetic field in a microstructure framework and provides a clear pathway to the researchers in selecting and utilizing the proposed lattices in the microscale modeling of MREs. The developed knowledge on microstructure modeling paves the way for design optimization of MREs and promotes the use of this intelligent materials in practical applications.

## **2.2 Experimental Study**

### **2.2.1 Fabrication of MRE samples**

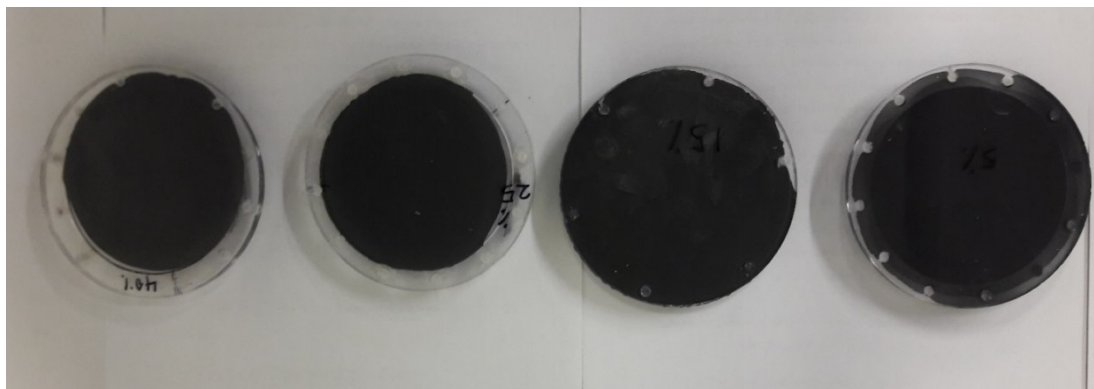
Table 2.1 presents the composition of six types of the MRE samples that have been fabricated. In order to fabricate the MREs, Ecoflex™ 00-20 (density = 1.04 g/cm<sup>3</sup>, viscosity = 3000 cps), and Ecoflex™ 00-50 (density = 1.04 g/cm<sup>3</sup>, viscosity = 8000 cps) silicone rubber were used as the elastomeric matrix material. The low viscosity of this rubber facilitates the distribution of particles in the matrix and ensures easy mixing and degassing. BASF SQ\* spherical shape CIPs with average diameter of 3.9 to 5 μm and density of 7.87 g/cm<sup>3</sup> were used as the magnetic fillers.

The fabrication process has three steps. First, the required amounts of the silicone rubber and CIPs were mixed together for about 4 min. The mixture was then degassed by placing it inside a vacuum chamber under

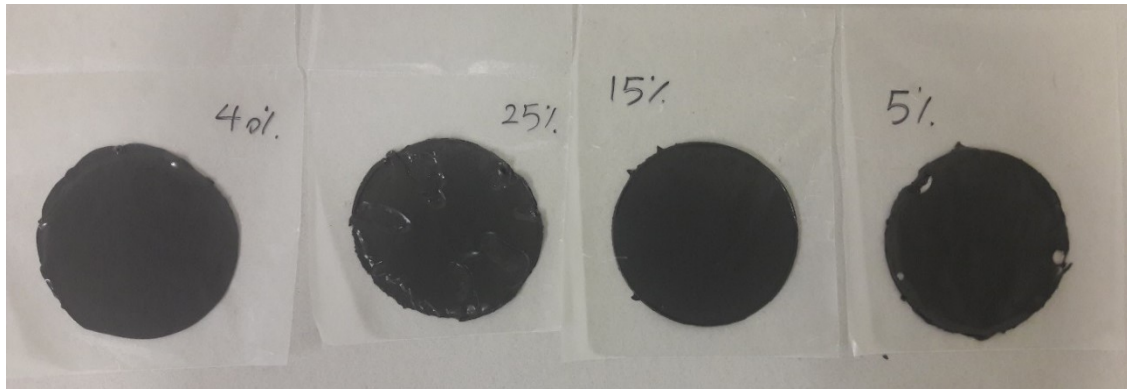
28 in-Hg for about 5 min. Next, the mixture poured into a cylindrical plexiglass mold and left at room temperature for about 24 h to be cured. For the anisotropic sample, the mold is placed under about 1 T magnetic field applied by a powerful electromagnet for 2 h to form chains of particles inside the material. After 24 h, MRE samples are taken out of the mold and left at room temperature for at least another 24 h to make sure that the samples are completely cured before cutting and performing the experiments. Figure 2.1 shows four isotropic MREs, i.e. Samples 1 to 4 of Table 2.1, in the curing stage inside the mold and after curing as they are taken out of the mold.

Table 2.1 Fabricated MRE samples and their constituents

MRE sample ID	Particles distribution	Materials		Volume fraction of constituents (%)	
		CIP	Silicone rubber	CIP	Silicone rubber
Sample 1	Isotropic	BASF SQ*	Ecoflex™ 00-20	5	95
Sample 2	Isotropic	BASF SQ*	Ecoflex™ 00-20	15	85
Sample 3	Isotropic	BASF SQ*	Ecoflex™ 00-20	25	75
Sample 4	Isotropic	BASF SQ*	Ecoflex™ 00-20	40	60
Sample 5	Isotropic	BASF SQ*	Ecoflex™ 00-50	15	85
Sample 6	Anisotropic	BASF SQ*	Ecoflex™ 00-50	15	85



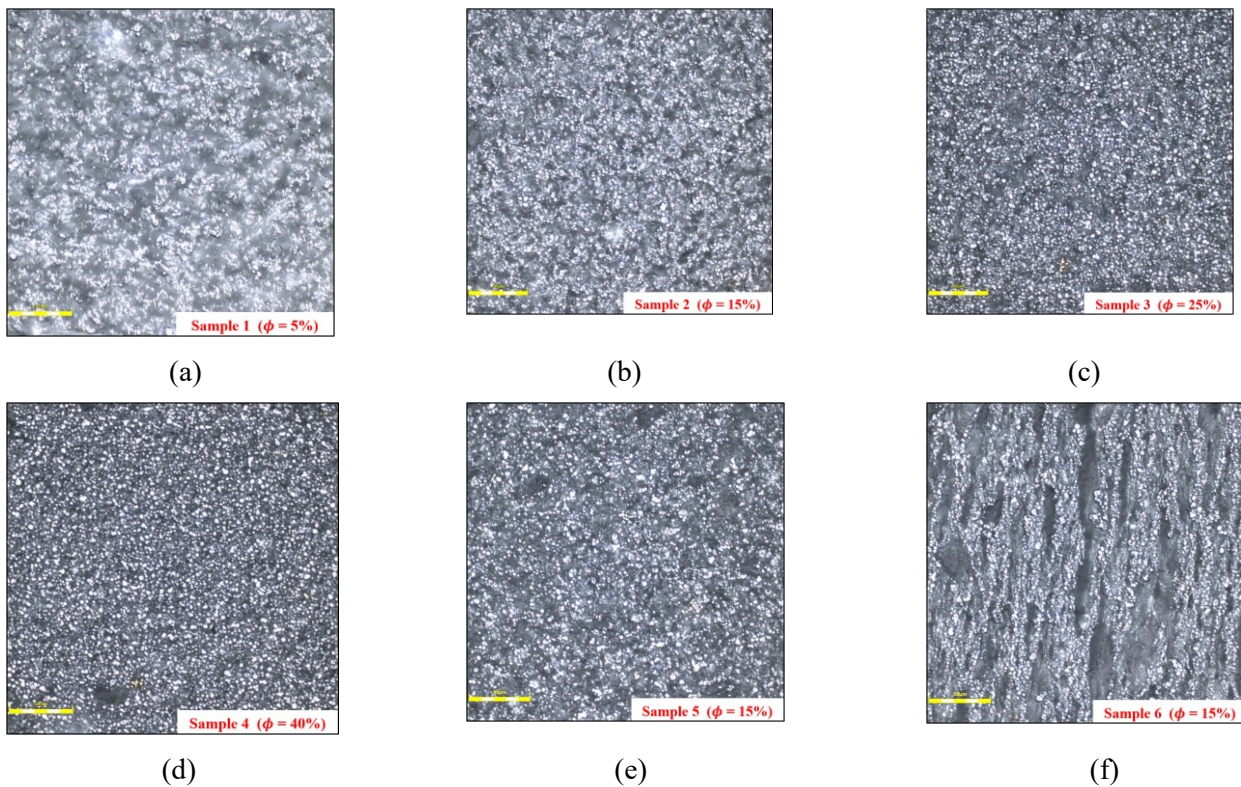
(a)



(b)

Figure 2.1 Samples 1 to 4 (a) in a cylindrical plexiglass mold in curing stage and (b) after curing.

The dispersion of particles in the MREs is investigated using an industrial laser measuring confocal microscope (OLYMPUS LEXT OLS4000). Images of microstructure are illustrated in Figure 2.2. The white points in the images show the embedded CIPs and the black background is the silicone rubber matrix. For the isotropic MREs, Samples 1 to 5, homogeneous dispersion of particles in the matrix is observed in the images while for the anisotropic MRE, Sample 6, particles are structured in chains.



(d)

(e)

(f)

Figure 2.2 Microstructure images of fabricated MRE samples taken by Confocal microscopy ( $\phi$  is the volume fraction of iron particles); (a) Sample 1, (b) Sample 2, (c) Sample 3, (d) Sample 4, (e) Sample 5, and (f) Sample 6.

### 2.2.2 Experimental characterization

The fabricated MRE samples were characterized using a rotary rheometer equipped with a magneto-rheology accessory (Discovery HR-3, TA Instrument) shown in Figure 2.3. The tests have been conducted using a 20 mm diameter parallel geometry under different levels of applied magnetic flux densities. For this purpose, the test specimens with 1 mm thickness and 20 mm diameter are carefully punched from the prepared samples and placed beneath the parallel geometry. The instrument is capable of providing a uniform magnetic field perpendicular to the direction of shear motion applied to the MRE sample. The applied magnetic field is measured using the Hall probe placed beneath the bottom geometry and a close-loop controller adjusts the required current input to the magneto-rheology accessory. Temperature has been kept constant at 20 °C using computer-controlled fluid circulator unit connected to the magneto-rheology accessory. Oscillatory tests have been performed sweeping the shear strain amplitude in the range of 0.001 % to 30 % and the applied torque was automatically measured and used for data acquisition to obtain the shear stress and moduli. All tests have been performed with the constant driving frequency of 0.1 Hz to resemble the quasi-static loading conditions. Moreover, an axial load of 5 N is applied on the samples in all tests to avoid the slippage between the sample and the geometries. It is noted that the empirical tests using the rheometer instrument in this research have been checked randomly for multiple testing cycles and for similar MRE samples fabricated at different times to make sure about the consistency and accuracy of the experimental data.

Figure 2.4 (a) to (d) present the shear stress with respect to the shear strain for Samples 1 to 4 under various levels of applied flux densities. As it can be seen in Figure 2.4 (a), the shear stress of Sample 1 increases as the magnetic flux density enhances. For instance, at 30 % shear strain amplitude, the shear stress rises from about 5.2 kPa to 8.4 kPa as the magnetic field increases from zero to 1T which shows 61 % increase in the shear stress. Accordingly, it can be concluded that the MREs become stiffer under application of an external magnetic field which is due to the resistance of the magnetized particles against the movement of polymeric chains of the silicone rubber matrix. Moreover, comparing the results obtained for MREs with different volume fractions of CIPs shows that the influence of applied magnetic field on the stiffness of the MREs is more pronounced as the volume fraction of particles increases. For example, increasing the magnetic field from zero to 1 T at 30 % shear strain amplitude, causes the shear stress to vary from 7.5 kPa to almost 23 kPa for Sample 2 which is 200 % increase. This increment is about 242 % and 590 % for Samples 3 and 4, respectively. Therefore, it can be concluded that the MR effect of the MREs in quasi-static state increases substantially with the iron particles' content.

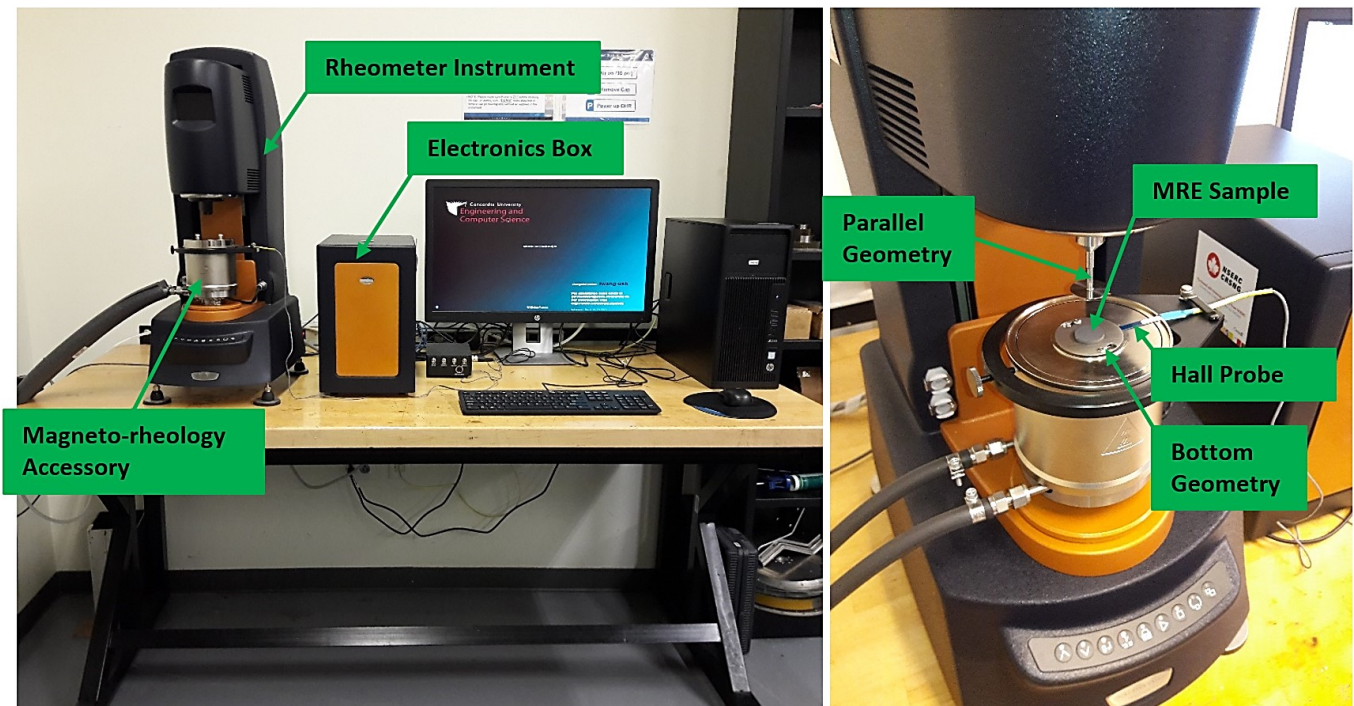


Figure 2.3 Left: Rheometer device system used for experimental testing; Right: Closer view of the position of MRE specimen on top of the magneto-rheology accessory.

In addition, the elastic behavior of the MREs changes with respect to the applied magnetic field. Figure 2.4 (a) shows that Sample 1 presents linear elastic behavior irrespective of the magnitude of the applied magnetic field. However, increasing the volume fraction of CIPs enhances the nonlinear properties of the MREs with respect to the applied magnetic flux density. It is clear in Figure 2.4 (b) that the MRE with 15 % volume fraction of solid particles acts almost as a linear elastic material within the whole strain amplitude range in the absence of applied magnetic field and its behavior gradually approaches to nonlinear properties as the magnetic field intensifies, particularly for magnetic fields above 0.4 T. Further increase of the volume participation level of CIPs enhances the nonlinear properties of the MRE samples as such the nonlinear response is obvious for the Samples 3 and 4 irrespective of the applied magnetic field level. It should be noted that the nonlinear elastic response of the MRE samples at high magnetic fields is due to the reinforcement of the polymeric matrix that changes the linear elastic response of the pure silicone rubber to nonlinear elastic behavior.

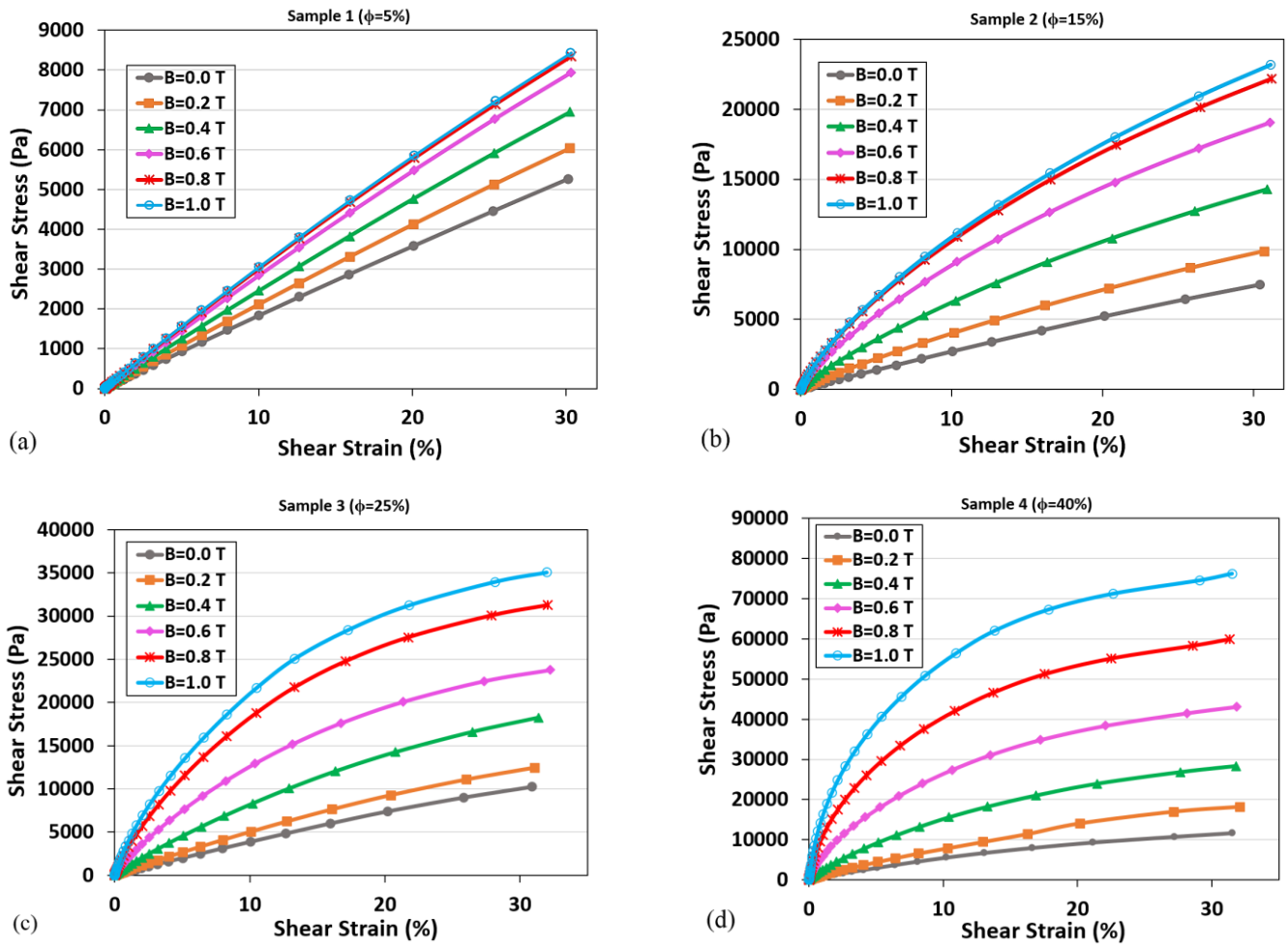


Figure 2.4 Shear stress versus strain for Samples 1 to 4 at different levels of magnetic flux density; (a) Sample 1 ( $\phi = 5\%$ ), (b) Sample 2 ( $\phi = 15\%$ ), (c) Sample 3 ( $\phi = 25\%$ ), and (d) Sample 4 ( $\phi = 40\%$ ).

Figure 2.4 also shows the magnetic saturation of the MRE samples with the increase of the applied magnetic field. In this subject, Figure 2.4 (a) illustrates that for the MRE sample with 5% volume fraction of iron particles, the rate of change of the shear stress decreases as the applied magnetic flux density reaches about 0.6 T and the MRE saturates magnetically as the applied magnetic flux density increases to 0.8 T. Moreover, Figure 2.4 (b) to (d) show that increasing the volume fraction of CIPs to 15%, 25% and 40%, increases the magnetic capacity of the MREs such a way that Sample 2 saturates at higher magnetic flux density compared to Sample 1 and Samples 3 and 4 do not show saturation in presence of applied magnetic flux densities below 1 T.



## 2.3 Elastic Response of the Filled Elastomer

Prior to model the magneto-mechanical properties of the MREs, it is required to determine the stress-strain behavior of the filled elastomer in the absence of magnetic field. There are many hyperelastic theories presented in the literature to predict the elastic response of rubbers. Here, three modeling methods including a Neo-Hookean law, a one-term Ogden theory [84] and a two-term  $I_1$ -based model [85] are selected for predicting the elastic response of passive MREs under simple shear loading. The elastic strain energy function for each of the models may be described as:

- Neo-Hookean law :  $E_{el} = \frac{\mu_1}{2} (I_1 - 3) = \frac{\mu_1}{2} (\lambda_1^2 + \lambda_2^2 + \lambda_3^2 - 3)$  (2.1)

- One-term Ogden theory:  $E_{el} = \frac{\mu_2}{\alpha_2} (\lambda_1^{\alpha_2} + \lambda_2^{\alpha_2} + \lambda_3^{\alpha_2} - 3)$  (2.2)

- Two-term  $I_1$ -based model:  $E_{el} = \frac{3^{1-\alpha_3}}{2\alpha_3} \mu_3 (I_1^{\alpha_3} - 3^{\alpha_3}) + \frac{3^{1-\alpha_4}}{2\alpha_4} \mu_4 (I_1^{\alpha_4} - 3^{\alpha_4})$  (2.3)

where  $I_1 = \lambda_1^2 + \lambda_2^2 + \lambda_3^2$  is the first principal invariant of the right Cauchy-Green deformation tensor and  $\lambda_i$  ( $i = 1,2,3$ ) is the principal extension ratio or stretch, i.e. the ratio of the current length to the original length in the  $i$ -th principal direction.  $\mu_i$  and  $\alpha_i$  are the constants of the models to be determined from experimental data.

For the situation of simple shear loading, the relationship between the extension ratio in the first principal direction and the shear strain ( $\gamma$ ) can be expressed as [84]:

$$\gamma = \lambda_1 - \frac{1}{\lambda_1} \quad (2.4)$$

The material is assumed to be incompressible ( $\lambda_1 \lambda_2 \lambda_3 = 1$ ) with a plane strain state ( $\lambda_3 = 1$ ). Then, the principal stretches are obtained in terms of the shear strain as:

$$\lambda_1 = \frac{\gamma + \sqrt{\gamma^2 + 4}}{2}, \quad \lambda_2 = \lambda_1^{-1} = \frac{\sqrt{\gamma^2 + 4} - \gamma}{2}, \quad \lambda_3 = 1 \quad (2.5)$$

Substituting the principal stretches from Eq. (2.5) into the strain energy functions in Eqs. (2.1) to (2.3) yields the following constitutive equations:

- Neo-Hookean:  $\tau = \mu_1 \frac{\lambda_1}{1 + \lambda_1^2} (\lambda_1^2 - \lambda_1^{-2}) = \mu_1 \gamma$  (2.6)

- One-term Ogden model:  $\tau = \mu_2 \frac{\lambda_1}{1 + \lambda_1^2} (\lambda_1^{\alpha_2} - \lambda_1^{-\alpha_2}) =$  (2.7)

$$\mu_2 \frac{2(\gamma + \sqrt{\gamma^2 + 4})}{8 + 2\gamma\sqrt{\gamma^2 + 4} + 2\gamma^2} \left( \left( \frac{\gamma + \sqrt{\gamma^2 + 4}}{2} \right)^{\alpha_2} - \left( \frac{\sqrt{\gamma^2 + 4} - \gamma}{2} \right)^{\alpha_2} \right)$$

- Two-term  $I_1$ -based model:  $\tau = \frac{\gamma}{\gamma^2+3} \sum_{r=3}^4 3^{1-\alpha_r} \mu_r (\gamma^2 + 3)^{\alpha_r}$  (2.8)

where  $\tau$  is the shear stress. Constant parameters in these models are found by least square optimization to minimize the error between theoretical and experimental results. Table 2.2 summarizes the values of the constant parameters found for each model and MRE samples. It should be noted that the values of the constant parameters involve the effect of different factors including but not limited to matrix type, volume fraction and type of iron particles, and more advanced phenomena such as interfaces between particles and elastomer matrix. Using parameters in Table 2.2 and Eqs. (2.6) to (2.8), the theoretical results of the shear stress versus shear strain for the four isotropic MRE samples, i.e. Samples 1 to 4, based on different models are obtained and compared with those of experimental shear stress data in the absence of the applied magnetic field as shown in Figure 2.5.

Table 2.2 Values of parameters of Neo-Hookean, one-term Ogden and two-term  $I_1$ -based models.

		MRE Sample	$\mu_1$ (Pa)			
Neo-Hookean Model	Sample 1		17716			
	Sample 2		25389			
	Sample 3		35007			
	Sample 4		41276			
			$\mu_2$ (Pa)		$\alpha_2$	
One-term Ogden Model	Sample 1		71890	0.25		
	Sample 2		74210	0.35		
	Sample 3		80770	0.45		
	Sample 4		48480	0.90		
			$\mu_3$ (Pa)	$\alpha_3$	$\mu_4$ (Pa)	$\alpha_4$
Two-term $I_1$ -based Model	Sample 1		8200	-12	10300	6
	Sample 2		16900	4.8	10800	-20
	Sample 3		33200	-2	6300	-23
	Sample 4		37800	-1	22100	-75

Examination of the results presented in Figure 2.5 shows that increasing the volume fraction of iron particles from 5% to 40% not only reinforces the material and makes it stiffer but also increases the

nonlinearity of the stress-strain curve. The stress-strain curve of the Sample 1 shows almost a full linear response in the whole strain region while in the case of Sample 4, the linear behavior only lasts up to around 0.05% strain. While all models exhibit satisfactory performance in predicting linear response of Sample 1, only two-term  $I_1$ -based model was capable of capturing the nonlinear behavior of MRE samples with higher volume fraction of CIPs at large strains.

It is noted that the Neo-Hookean and One-term Ogden models are commonly used as nonlinear hyper elastic theories for stretching and extension [84], however, for the case of simple shear loading, these models demonstrate linear stress-strain response which is valid only at small strain ranges ( $\gamma < 0.1$ ) as shown in Figure 2.5. In the following sections, the two-term  $I_1$ -based model will be used to account for the elastic response of the MRE samples at zero magnetic field.

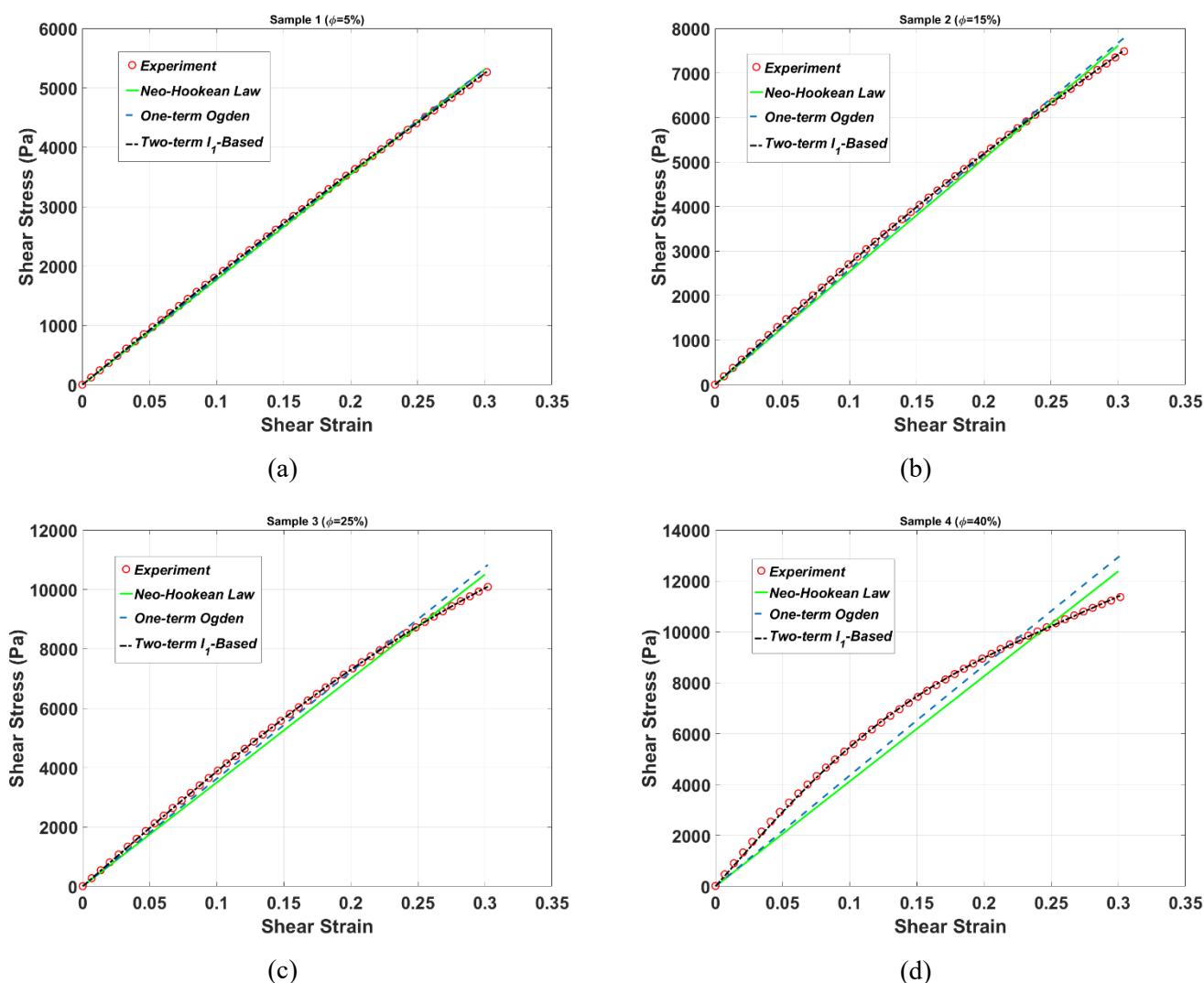


Figure 2.5 Experimental and theoretical results of the shear stress versus shear strain for the isotropic MRE samples at zero magnetic field; (a) Sample 1, (b) Sample 2, (c) Sample 3, and (d) Sample 4.

## 2.4 Quasi-Static Microscale Modeling of Magneto-Mechanical Properties of MREs

This section presents a physical microscale modeling to describe the field-dependent magneto-mechanical behavior of both isotropic and anisotropic MREs operating in quasi-static shear mode. For this purpose, different lattice models are proposed as idealized representation of the spatial distribution of magnetic particles in the material and the mechanical properties are then evaluated based on particles' distribution.

### 2.4.1 Total potential energy

The total potential energy of a deformed MRE in the presence of a magnetic field is basically comprised of two distinct parts. One is the elastic energy ( $E_{el}$ ) of the deformed MRE due to the elasticity of polymer chains and the other is the magnetic potential energy ( $E_m$ ) of the embedded magnetic particles in the matrix under an external magnetic field. Thus, the total potential energy of the deformed MRE ( $E_T$ ) under external magnetic field can be written as:

$$E_T = E_{el} + E_m \quad (2.9)$$

For the elastic part of the potential energy, the strain energy function of the two-term  $I_1$ -based model given in Eq. (2.3) is employed. As discussed in Section 2.3, the two-term  $I_1$ -based model is capable of predicting the nonlinear behavior of MREs under shear loading in the absence of magnetic field. Therefore, this energy function is used to predict the zero-field elastic response of the filled elastomer and so includes contribution of different possible phenomena such as reinforcement of elastic matrix by particles and possible adhesion at the interface of polymer matrix and hard filler particles.

For the second part of the total potential energy, the interaction of the particles under external magnetic field should be formulated. The ferromagnetic iron particles are magnetized after being subjected to an external magnetic field. Accordingly, a magnetic moment is induced in each magnetized particle which can be alternatively called as dipole. Due to the induced magnetic moment, there will be magnetic forces between the particles which is the microstructural phenomenon behind the field-dependent properties of MREs. The interaction energy of two adjacent dipoles with magnetic moments  $\mathbf{m}_1$  and  $\mathbf{m}_2$  is [86]:

$$e_{12} = -\frac{1}{4\pi\mu_1\mu_0} \left[ \frac{3(\mathbf{m}_1 \cdot \mathbf{R}_{12})(\mathbf{m}_2 \cdot \mathbf{R}_{12})}{|\mathbf{R}_{12}|^5} - \frac{\mathbf{m}_1 \cdot \mathbf{m}_2}{|\mathbf{R}_{12}|^3} \right] \quad (2.10)$$

where  $\mu_0$  and  $\mu_1$  stand for the vacuum permeability and the relative permeability of the medium, respectively. Since the elastomer matrix is assumed non-magnetic, its relative permeability is unity, i.e.  $\mu_1 = 1$ .  $\mathbf{R}_{12}$  is the spatial vector that connects the two dipoles' centers. To consider the magnetic interaction of all particles in the network, the magnetic energy density of the MRE sample could be expressed as:

$$E_m = -\frac{1}{V} \frac{1}{4\pi\mu_1\mu_0} \sum_i \sum_j \left[ \frac{3(\mathbf{m}_i \cdot \mathbf{R}_{ij})(\mathbf{m}_j \cdot \mathbf{R}_{ij})}{|\mathbf{R}_{ij}|^5} - \frac{\mathbf{m}_i \cdot \mathbf{m}_j}{|\mathbf{R}_{ij}|^3} \right] \quad (2.11)$$

where  $V$  is the volume of the sample. The double summation in the Eq. (2.11) operates over all pairs of dipoles ( $i$ -th and  $j$ -th) in the network. The spatial vector  $\mathbf{R}_{ij}$  between two dipoles depends on the macroscopic deformation of the sample. Figure 2.6 shows schematically an infinitesimal element of a MRE sample in undeformed and deformed situations by simple shear loading (within x-y plane) under an external magnetic field perpendicular to the direction of the shear deformation. Considering Figure 2.6, the components of the space vector  $\mathbf{R}_{ij} = (R_{ij_x}, R_{ij_y}, R_{ij_z})$  between two dipoles under simple shear deformation could be related to the shear strain  $\gamma$  as follows:

$$\begin{aligned} R_{ij_x} &= R_{ij_x}^0 + \gamma (R_{ij_y}^0) = R_{ij_x}^0 + \gamma (R_{ij_y}^0) \\ R_{ij_y} &= R_{ij_y}^0 \\ R_{ij_z} &= R_{ij_z}^0 \end{aligned} \quad (2.12)$$

where  $\mathbf{R}_{ij}^0 = (R_{ij_x}^0, R_{ij_y}^0, R_{ij_z}^0)$  is the space vector between two particles in undeformed situation.

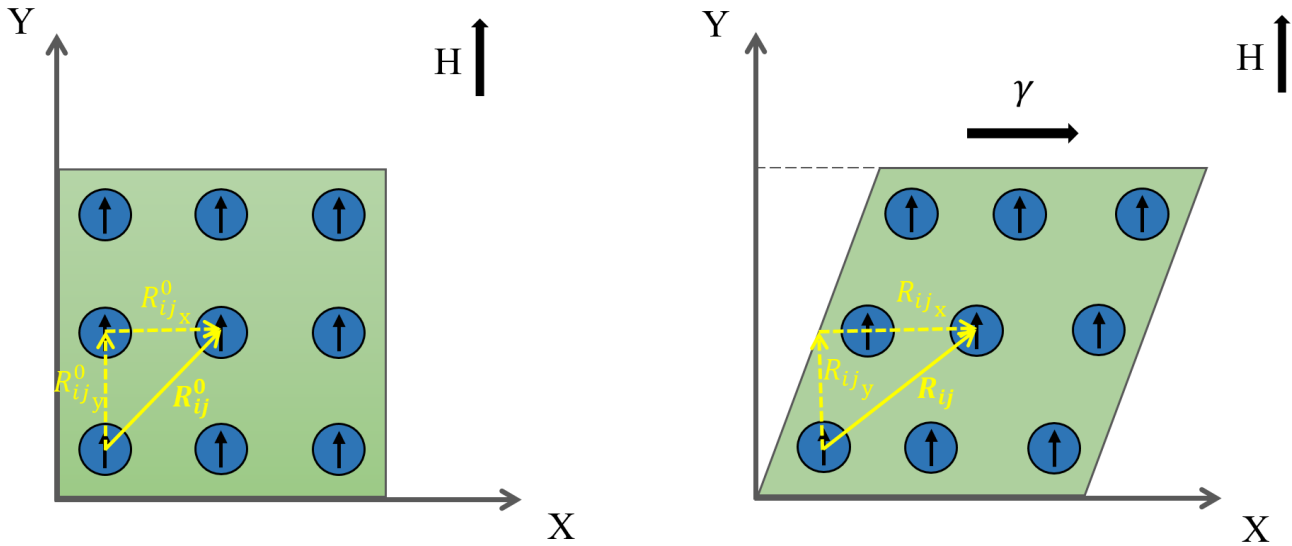


Figure 2.6 Infinitesimal element of an MRE sample in undeformed (left) and deformed (right) situations under simple shear loading (within x-y plane) and an external magnetic field (along y axis).

To perform the summation in Eq. (2.11) over all pairs of particles, we need to idealize the arrangement of particles in the material by some structured and idealized networks of particles in which the position of individual particles could be quantified. Figure 2.7 illustrates this idea graphically. For the isotropic MREs, seven lattices are proposed to represent distribution of particles in the material. For the anisotropic MRE, the

dispersion of particles is idealized with simple chain-like structure of particles in the medium. The two following sections explain these two cases.

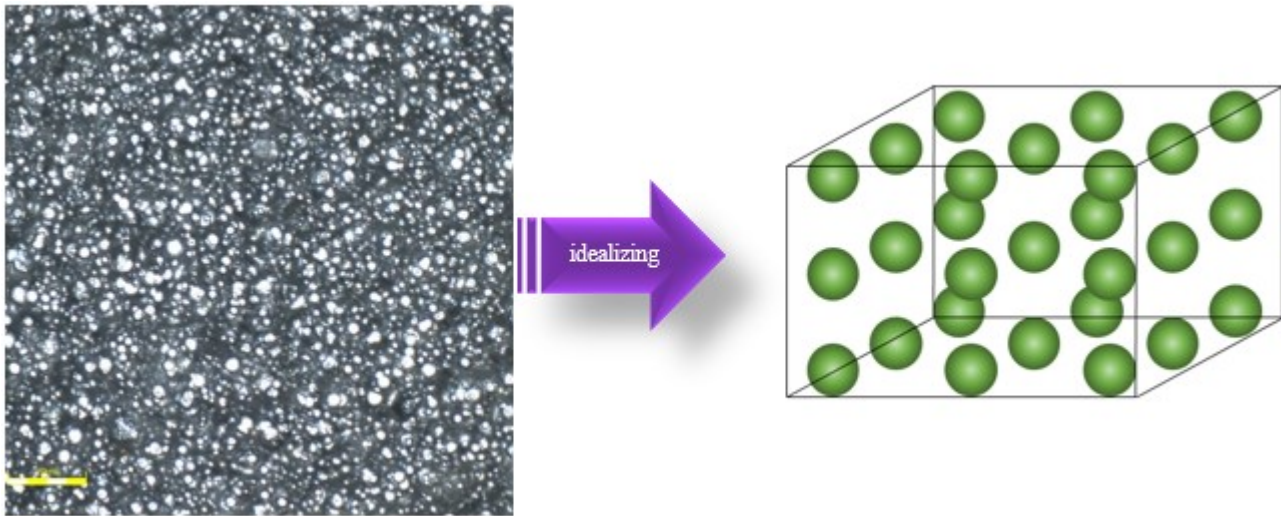
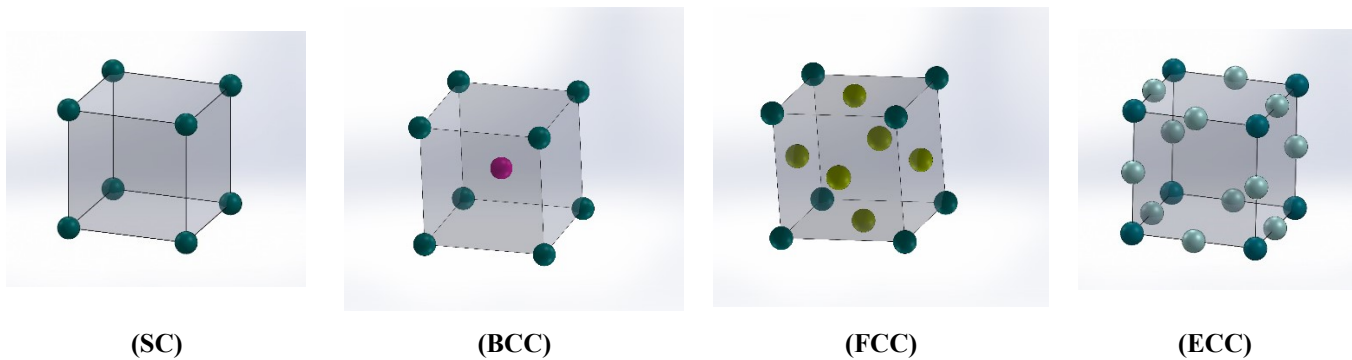


Figure 2.7 Graphical illustration for idealization of particles distribution with structured predetermined particle networks. Left: real isotropic dispersion of particles in an MRE sample, Right: schematic idealized network of particles with exaggerated particle size.

### 2.4.2 Isotropic particle distribution

For the isotropic MREs, the iron particles are assumed to be arranged based on some lattice models. Herein, seven lattices are proposed to represent isotropic distribution of particles in the material. The considered lattice types are simple cubic (SC), body centered cubic (BCC), face centered cubic (FCC), edge centered cubic (ECC), body and edge centered cubic (BECC), face and edge centered cubic (FECC), and body, face and edge centered cubic (BFECC). The first four types are basic lattices and the last three are combinations of the basic ones. Figure 2.8 illustrates the unit cell for each of the considered lattice models.



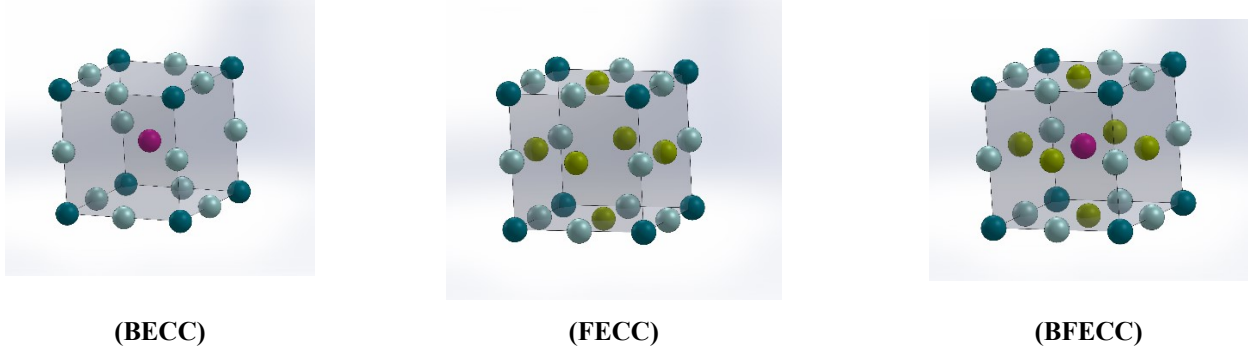


Figure 2.8 Unit cell of lattice models considered for isotropic distribution of particles.

A parameter  $\hat{\zeta}$  is defined which shows the number of particles participated in a unit cell. For instance, eight particles are located at the corners of the SC unit cell, from which 1/8 of each particle presents inside the cell. Thus, one whole particle participates inside each unit cell of the SC lattice ( $\hat{\zeta}_{SC}=1$ ). The value of  $\hat{\zeta}$  for all the lattice models presented in Figure 2.8 are as follows:

$$\hat{\zeta}_{SC}=1, \quad \hat{\zeta}_{BCC}=2, \quad \hat{\zeta}_{FCC}=4, \quad \hat{\zeta}_{ECC}=4, \quad \hat{\zeta}_{BECC}=5, \quad \hat{\zeta}_{FECC}=7, \quad \hat{\zeta}_{BF ECC}=8 \quad (2.13)$$

As a simplifying assumption, all iron particles are assumed to have the same spherical shape with average radius of  $r$ . Then, the volume fraction of iron particles distributed in the MRE sample is given by [62]:

$$\phi = \hat{\zeta} \frac{v_0}{a^3} \quad (2.14)$$

where  $v_0 = \frac{4}{3}\pi r^3$  corresponds to the volume of a particle, and  $a$  is the edge length of the unit cell of the lattice. The proposed unit cells are building blocks for the enormous lattice with millions of particles in the material. In the modeling, an infinite lattice of particles is considered. An infinite lattice has both translational and rotational symmetries around the axis of the homogeneous applied magnetic field  $\mathbf{H}$  which is the y-axis as shown in Figure 2.6. Accordingly, the induced magnetic moments of the dipoles are in the direction of the applied magnetic field with equal absolute values  $|\mathbf{m}_i| = |\mathbf{m}_j| = |\mathbf{m}|$ . Conducting summation in Eq. (2.11) in the whole medium would be computationally impractical. To simplify, here we consider an infinite lattice structure for the MRE samples and due to symmetry, the position of the origin of the lattice would not affect the overall summation [59]. Considering this, the network of dipoles (magnetized particles) have been established based on different lattice models shown in Figure 2.8 in which the  $j$ -th particle is chosen as the origin of the lattice network. The double summation in Eq. (2.11) is then reduced to single summation over index  $i$  multiplied by the number of particles  $N$ . Finally, Eq. (2.11) could be rewritten as follows:

$$E_m = -\frac{c|\mathbf{m}|^2}{4\pi\mu_0} \sum_i \left[ \frac{3(\mathbf{R}_i)_y^2 - |\mathbf{R}_i|^2}{|\mathbf{R}_i|^5} \right] \quad (2.15)$$

where  $\mathbf{R}_i$  is the spatial vector defining each particle's position in the space from the origin of the lattice.  $c = N/V$  is the total number of ferromagnetic particles in the volume  $V$  of the MRE sample which can be described also as  $c = N/V = \hat{\zeta}/a^3$  based on the unit cell of the lattice models. The magnetic dipole moment per unit particle volume is defined as the intrinsic particle polarization so it can be written as  $|\mathbf{m}| = v_0 J_p$ , where  $J_p$  is the induced particle polarization in SI units of Tesla [51], [87]. The components of the space vector  $\mathbf{R}_i$  was related with the shear strain ( $\gamma$ ) and the initial space vector  $\mathbf{R}_i^0$  in Eq. (2.12). The initial space vector can be expressed as:

$$\mathbf{R}_i^0 = a \mathbf{r}_i \quad (2.16)$$

where  $\mathbf{r}_i = (r_{ix}, r_{iy}, r_{iz})$  is a dimensionless vector addressing the coordinates of particles on the sites of infinite lattices with unit edge length, except  $\mathbf{r}_i = 0$  which has to be excluded from the calculations. Now, considering simple shear in x-y plane as shown in Figure 2.6, we may write Eq. (2.12) as:

$$\begin{aligned} R_{ix} &= R_{ix}^0 + \gamma (R_{iy}^0) = a r_{ix} + \gamma (R_{iy}^0) = a (r_{ix} + \gamma r_{iy}) \\ R_{iy} &= R_{iy}^0 = a r_{iy} \\ R_{iz} &= R_{iz}^0 = a r_{iz} \end{aligned} \quad (2.17)$$

$$|\mathbf{R}_i| = \sqrt{R_{ix}^2 + R_{iy}^2 + R_{iz}^2} = a \sqrt{(r_{ix} + \gamma r_{iy})^2 + r_{iy}^2 + r_{iz}^2}$$

By substituting Eqs. (2.17), and (2.14) into Eq. (2.15), and considering that  $|\mathbf{m}| = v_0 J_p = J_p \phi a^3 / \hat{\zeta}$  and also  $c = \hat{\zeta}/a^3$ , the potential magnetic interaction energy of the MRE sample with volume particle fraction of  $\phi$  could be obtained as a function of particle polarization, volume fraction of iron particles, and shear strain in the following form:

$$E_m = -\frac{\phi^2 J_p^2}{4\pi\mu_0 \hat{\zeta}} \sum_i \left[ \frac{(2 - \gamma^2)r_{iy}^2 - r_{ix}^2 - r_{iz}^2 - 2\gamma r_{ix} r_{iy}}{\left( (1 + \gamma^2)r_{iy}^2 + r_{ix}^2 + r_{iz}^2 + 2\gamma r_{ix} r_{iy} \right)^{\frac{5}{2}}} \right] \quad (2.18)$$

It is noted that the particle polarization,  $J_p$ , could not be directly measured. Jolly et al. [51] have presented a particle saturation model which establishes a relation between the particle polarization and average flux density in MREs which can be measured experimentally using magnetometers. The particle saturation model is founded on the basis that particle saturation begins near the contact point of two adjacent particles at very low magnetic field and increases toward total particle saturation as the applied field increases. Based on this model, particle polarization,  $J_p$ , for an MRE with volume fraction of  $\phi$  can be expressed as a function of the averaged flux density,  $B$ , as:



$$J_p = \frac{\frac{3}{2}(\alpha - \alpha^3)B + (1 - \alpha^3)(sJ_s)}{1 + \frac{3}{2}\phi(\alpha - \alpha^3)} \quad (2.19)$$

where  $J_s$  is the saturation polarization, and  $\alpha$  is a parameter constrained within the range of 0 and 1 and defined as:

$$\alpha = \frac{1}{6k} \left[ \left( 3 - \frac{2}{\phi} \right) \pm \sqrt{\left( 3 - \frac{2}{\phi} \right)^2 + 12k \left( \frac{2}{\phi} \left( 1 - k \frac{B}{(sJ_s + B - \phi J_p)} \right) + 3(k - 1) \right)} \right] \quad (2.20)$$

where  $k \geq 1$  is a constant parameter added to the model to account for the complex multipolar interactions resulting from complex structure of particles in the material. The value of saturation polarization,  $J_s$ , for pure iron is 2.1 T [51]. However, MRE samples with various volume fraction of particles will saturate at different level of magnetic induction as observed in Section 2.2.2. Therefore, another constant parameter,  $s$ , is used in the model as the coefficient of the saturation polarization to tune the results of lattice models according to the saturation of different MRE samples.

Values of these two fitting parameters ( $k, s$ ) will be selected consciously in the following subsections to evaluate the performance of different lattice types. However, to compare the results of model with the experimental data, optimal values of the constant parameters ( $k, s$ ) will be identified by a least square optimization technique in Section 2.5.

It should be noted that Eq. (2.19) has been presented as follows:

$$J_p = \frac{\frac{3}{2}\alpha^3 B + (1 - \alpha^3)J_s}{1 + \frac{3}{2}\phi\alpha^3} \quad (2.21)$$

in the Ref. [51], which does not match the assumptions and preceding relations presented in the article. Therefore, the particle polarization,  $J_p$ , has been corrected as Eq. (2.19) in the present study. The detail derivation is demonstrated in Appendix A of this dissertation.

#### 2.4.2.1 Calculation of summation in Eq. (2.18)

The role of summation in Eq. (2.18) is to accumulate the contribution of all particles' magnetic interaction in the network. The components  $r_{i_x}$ ,  $r_{i_y}$ , and  $r_{i_z}$  characterize the coordinates of particles on the sites of each lattice model with unit edge length in the x, y, and z directions with respect to the origin of arbitrary coordinate system. To explain the calculation of summation in the Eq. (2.18), a simple example is given here.

By considering one unit cell at each corner of the origin of the coordinate system, a network of particles involving 8 unit cells will be constructed. Figure 2.9 shows the 2D (in-plane) illustration of such particle network for the SC and BCC lattices.

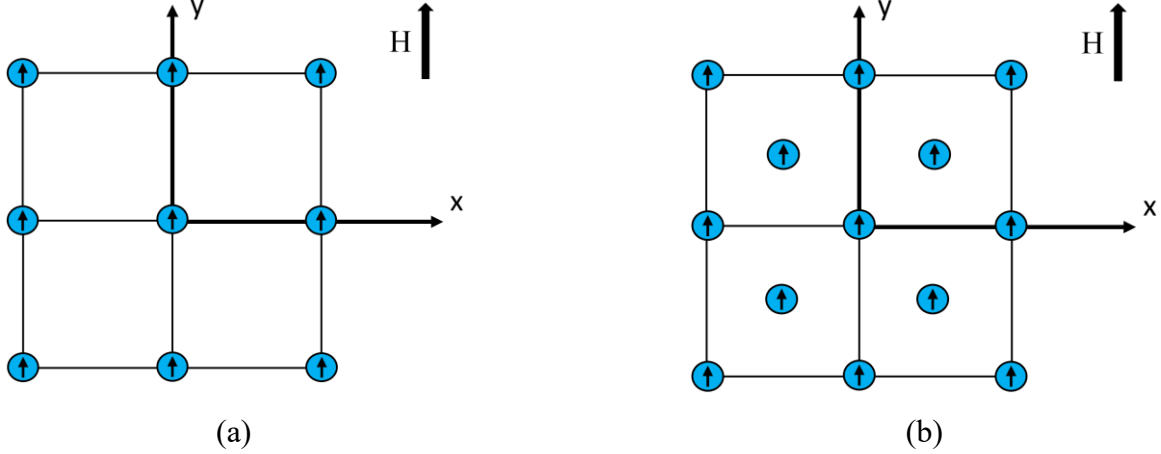


Figure 2.9 2D (in-plane) view of a network of particles made by placing one unit cell at each corner of the origin (a) SC, and (b) BCC lattices.

According to Figure 2.9, the components of vector  $\mathbf{r}_i = (r_{ix}, r_{iy}, r_{iz})$  vary in the range  $(-1, 1)$ . There are 26 particles, except the one at origin, on the sites of the SC lattice which their coordinates are:

$$\begin{aligned} \mathbf{r}_i = \{ & (1,1,-1), (0,1,-1), (-1,1,-1), (1,0,-1), (0,0,-1), (-1,0,-1), (1,-1,-1), (0,-1,-1), (-1,-1,-1), \\ & (1,1,0), (0,1,0), (-1,1,0), (1,0,0), (-1,0,0), (1,-1,0), (0,-1,0), (-1,-1,0), (1,1,1), (0,1,1), (-1,1,1), \\ & (1,0,1), (0,0,1), (-1,0,1), (1,-1,1), (0,-1,1), (-1,-1,1) \} \end{aligned} \quad (2.22)$$

And for the BCC lattice, there are 34 particles, except the one at origin, which their coordinates are:

$$\begin{aligned} \mathbf{r}_i = \{ & (1,1,-1), (0,1,-1), (-1,1,-1), (1,0,-1), (0,0,-1), (-1,0,-1), (1,-1,-1), (0,-1,-1), (-1,-1,-1), \\ & (0.5,0.5,-0.5), (-0.5,0.5,-0.5), (0.5,-0.5,-0.5), (-0.5,-0.5,-0.5), (1,1,0), (0,1,0), (-1,1,0), (1,0,0), \\ & (-1,0,0), (1,-1,0), (0,-1,0), (-1,-1,0), (0.5,0.5,0.5), (-0.5,0.5,0.5), (0.5,-0.5,0.5), (-0.5,-0.5,0.5), \\ & (1,1,1), (0,1,1), (-1,1,1), (1,0,1), (0,0,1), (-1,0,1), (1,-1,1), (0,-1,1), (-1,-1,1) \} \end{aligned} \quad (2.23)$$

For calculation of the summation in the case of particle networks shown in Figure 2.9, all the configurations of  $(r_{ix}, r_{iy}, r_{iz})$  from the above vectors are used in the calculation process. Thus, the summation runs over 26 particles for the SC lattice and over 34 particles for the BCC lattice.

Considering that the distance between particles and the origin is in the denominator with a power of 3 (look at Eq. (2.15) with simplification), the summation in Eq. (2.18) converges by reaching the unit cells far from the origin. Therefore, by using a network of particles involving finite number of cells placed at the origin of the coordinate system, the calculation of the summation could be terminated. In the present study,

in order to ensure the accuracy of results, the summation is calculated for a collection of at least 64 cells for each lattice model.

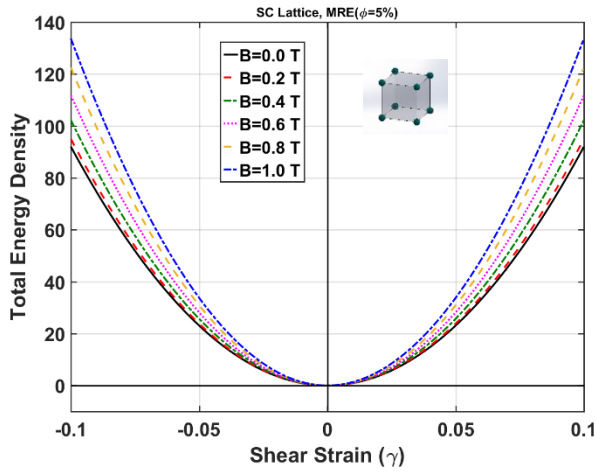
#### 2.4.2.2 Comparison of total potential energy of MREs using different lattice models

By combining the elastic energy based on two-term  $I_1$ -based model from Eq. (2.3) with the magnetic energy given in Eq. (2.18), the total potential energy of a MRE sample can be obtained as:

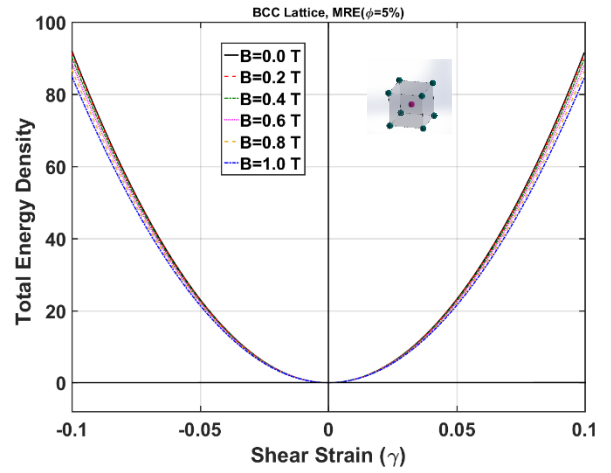
$$E_T = \frac{3^{1-\alpha_3}}{2\alpha_3} \mu_3 (I_1^{\alpha_3} - 3^{\alpha_3}) + \frac{3^{1-\alpha_4}}{2\alpha_4} \mu_4 (I_1^{\alpha_4} - 3^{\alpha_4}) - \frac{\phi^2 J_p^2}{4\pi\mu_0 \zeta^2} \sum_i \left[ \frac{(2 - \gamma^2)r_{iy}^2 - r_{ix}^2 - r_{iz}^2 - 2\gamma r_{ix}r_{iy}}{\left( (1 + \gamma^2)r_{iy}^2 + r_{ix}^2 + r_{iz}^2 + 2\gamma r_{ix}r_{iy} \right)^{\frac{5}{2}}} \right] \quad (2.24)$$

In which, particle polarization,  $J_p$ , is found using Eqs. (2.19) and (2.20). Here, for each lattice type, the total energy is calculated for an isotropic MRE with  $\phi = 5\%$  volume fraction of iron particles at different levels of magnetic field. Constant parameters for the elastic energy term are selected from Table 2.2. Figure 2.10 shows the total energy density versus shear strain ( $\gamma$ ) at several magnetic flux densities for different proposed lattice models.

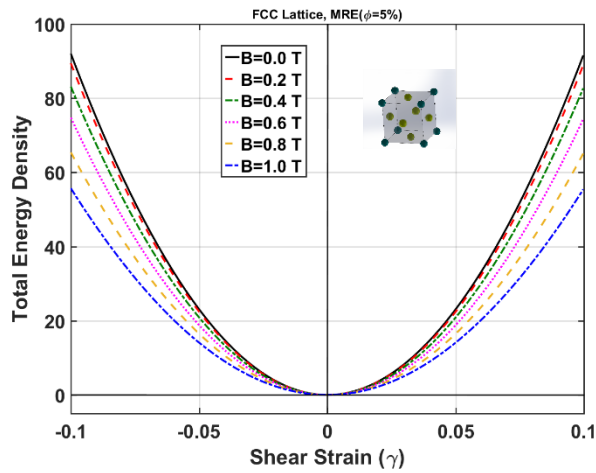
Figure 2.10 shows that the energy of the MRE changes with the magnetic flux density and, as expected, the level of change is different for each lattice type. Examination of results reveals that at a constant magnetic field intensity, potential energy shows similar increasing behavior with the strain amplitude for all lattices. On the other hand, at a constant strain, the potential energy increases directly with the applied magnetic field for all lattice types except for the FCC and BCC lattices where the energy decreases with the increase of the flux density.



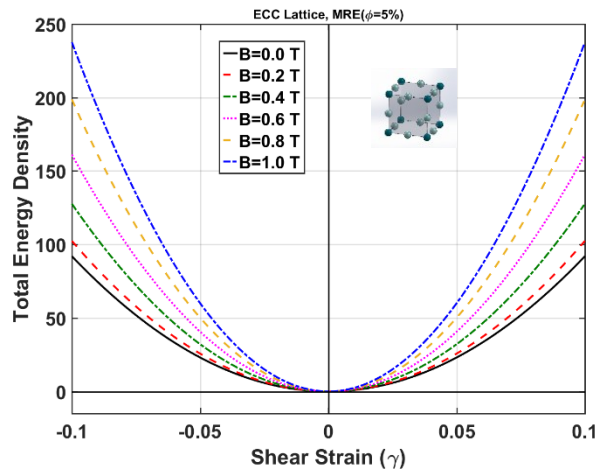
(a)



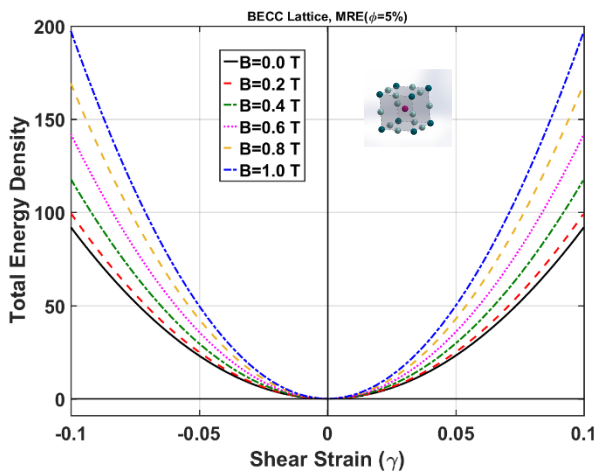
(b)



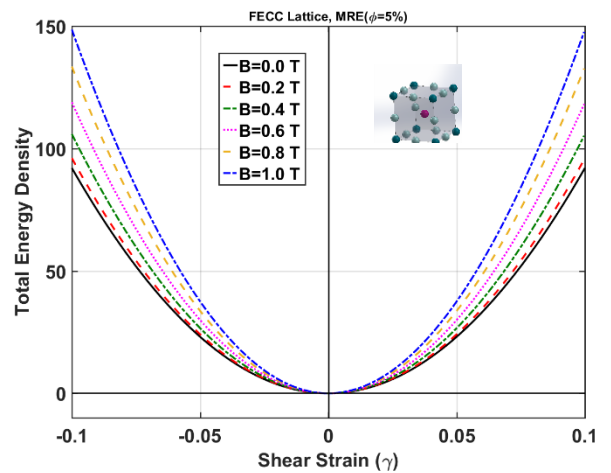
(c)



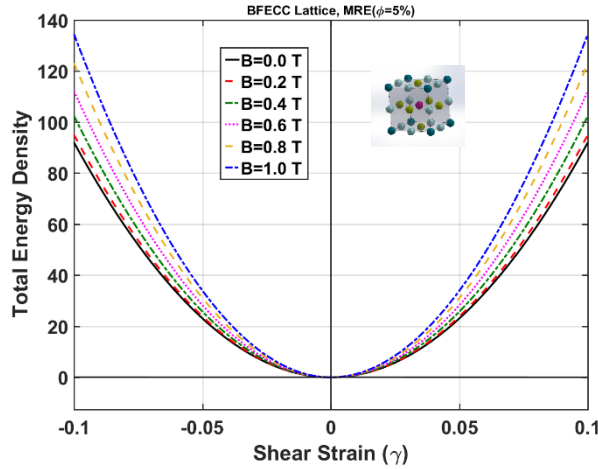
(d)



(e)



(f)



(g)

Figure 2.10 Total potential energy density for MRE material with  $\phi = 5\%$  under various flux densities assuming particle distribution according to different lattice models; (a) SC, (b) BCC, (c) FCC, (d) ECC, (e) BECC, (f) FECC, and (g) BFECC ( $k = 1, s = 1$ ).

To compare the absolute energy of all lattice networks at constant magnetic flux density, the total potential energy density is calculated at  $B = 0.6$  T for all the lattices. Figure 2.11 shows the results with respect to the shear strain amplitude. As it can be realized, the ECC and FCC lattices has the maximum and minimum level of energy, respectively. On the other hand, the SC and BFECC lattices have the same level of energy. These results show the difference in the properties of the proposed lattice types which originate from the particle arrangement in each lattice.

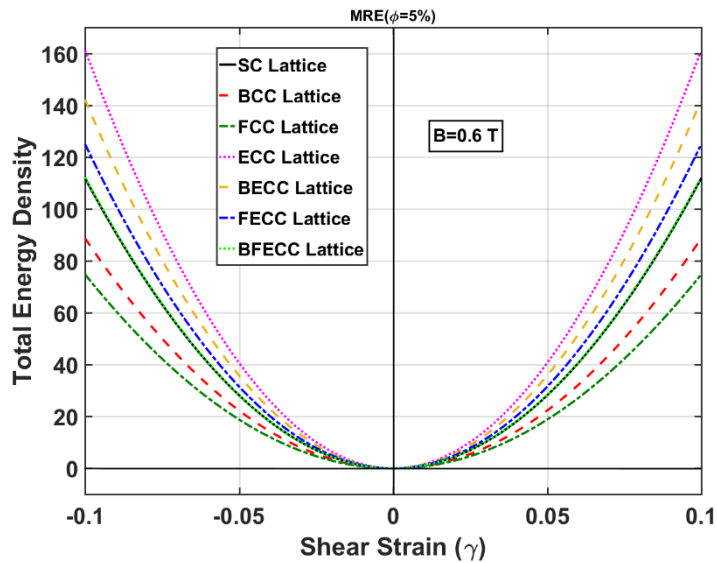


Figure 2.11 Comparison of total energy density of the proposed lattices for  $\phi = 5\%$  under applied flux density of  $B = 0.6$  T ( $k = 1, s = 1$ ).

### 2.4.2.3 Comparison of shear modulus of MREs using different lattice models

By taking the second derivative of the total energy density with respect to the shear strain evaluated at  $\gamma = 0$ , shear modulus of the MRE sample could be computed as:

$$G = \frac{\partial^2 E_T}{\partial \gamma^2} \Big|_{\gamma=0} \quad (2.25)$$

Figure 2.12 shows the results of the shear modulus as a function of magnetic flux density varying from 0 T to 1 T for MRE with 5 % volume fraction of particles arranged based on different lattice models. As it can be seen from Figure 2.12, for the SC, ECC, BECC, FECC, and BFECC lattice models, the shear modulus increases as the flux density increases and reaches to near saturation at high magnetic flux density. While for the BCC and FCC lattices, the shear modulus decreases with the applied magnetic field due to decreasing trend of their total strain energy function with respect to the applied magnetic field. The results for the BCC lattice are also available in the literature [62] which shows the same trend. Decrease of the shear modulus with magnetic field is in contradiction with experimental observations reported in the literature [9], [27], [51], [88] as well as with those presented in the present research, thus the BCC and FCC models cannot represent the microstructure behavior of the MREs. The reason behind this behavior of the BCC and FCC lattices is discussed in the Section 2.4.4.

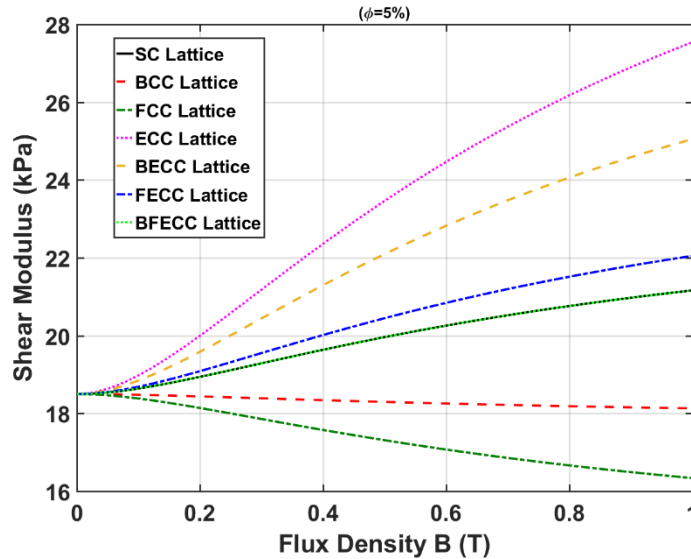


Figure 2.12 Comparison of shear modulus as a function of applied magnetic field for the proposed lattices with  $\phi = 5\%$  ( $k = 1$ ,  $s = 0.3$ ).

Figure 2.12 also shows that the ECC lattice provides the maximum increase in the shear modulus among the other lattices. Similar to the results of the energy, SC and BFECC lattices exhibit the same change in the shear modulus with enhancement of the applied magnetic field.

### 2.4.3 Anisotropic particle distribution

In this section, the proposed idealized arrangement of iron particles in the material is modified to represent the chain like structure of particles in the anisotropic MREs. Figure 2.13 shows the idealized isotropic and anisotropic arrangement of particles schematically in which  $a_x^0$ ,  $a_y^0$ , and  $a_z^0$  describe the distances between neighboring particles in the  $x$ ,  $y$ ,  $z$  directions, respectively, in Cartesian coordinates. As it can be seen, the distance of adjacent particles in  $x$ ,  $y$ ,  $z$  directions are the same for isotropic dispersion, thus  $a_x^0 = a_y^0 = a_z^0$  while for the anisotropic distribution, the vertical distance is smaller, i.e.  $a_y^0 < a_x^0 = a_z^0$ . A new parameter is defined as:

$$\beta = \frac{a_y^0}{a_x^0} \quad (2.26)$$

where  $\beta = 1$ , corresponds to the isotropic configuration and  $\beta < 1$  represents anisotropic configurations with particles forming a chain-like structure. Considering that for the anisotropic configuration with chain-like structure  $\hat{\zeta} = 1$  and noting that  $\phi = \hat{\zeta} \frac{\frac{4}{3}\pi r^3}{a_x^0 a_y^0 a_z^0} = \frac{\frac{4}{3}\pi r^3}{a_x^0 a_y^0 a_z^0}$  is the volume fraction of iron particles ( $r$  is the average particle radius), minimum and maximum values of  $\beta$  could be calculated. By substituting  $a_y^0 = 2r$  (minimum value of  $a_y^0$ ) and  $a_x^0 = a_z^0 = \frac{2r}{\beta}$  from Eq. (2.26) in the relation for  $\phi$ , the minimum value of  $\beta_{min} = \sqrt{6\phi/\pi}$  is obtained. Similarly,  $a_x^0 = a_z^0 = 2r$  (minimum value of  $a_x^0$  and  $a_z^0$ ) and  $a_y^0 = 2r\beta$ , yield the maximum value of  $\beta_{max} = \pi/6\phi$ . Needless to say,  $\beta$  could vary between its minimum and maximum values. Remembering from the Eq. (2.16), here the initial space vector  $\mathbf{R}_i^0$  can generally be expressed as:

$$\mathbf{R}_i^0 = (a_x^0 r_{ix}, a_y^0 r_{iy}, a_z^0 r_{iz}) \quad (2.27)$$

where the vector  $\mathbf{r}_i = (r_{ix}, r_{iy}, r_{iz})$  has the same definition as defined in Eq. (2.16). After the application of magnetic field and mechanical deformation on the material, the new space vector for the particles is described by  $\mathbf{R}_i = (a_x r_{ix}, a_y r_{iy}, a_z r_{iz})$ . Now, considering simple shear situation as shown in Figure 2.6, the space vector is related to the shear strain as:

$$\begin{aligned} R_{ix} &= R_{ix}^0 + \gamma (R_{iy}^0) = a_x^0 r_{ix} + \gamma (R_{iy}^0) = (a_x^0 r_{ix} + \gamma a_y^0 r_{iy}) = a_x^0 (r_{ix} + \gamma \beta r_{iy}) \\ R_{iy} &= R_{iy}^0 = a_y^0 r_{iy} = \beta a_x^0 r_{iy} \\ R_{iz} &= R_{iz}^0 = a_z^0 r_{iz} = a_x^0 r_{iz} \end{aligned} \quad (2.28)$$

$$|\mathbf{R}_i| = \sqrt{R_{ix}^2 + R_{iy}^2 + R_{iz}^2} = a_x^0 \sqrt{(r_{ix} + \gamma \beta r_{iy})^2 + \beta^2 r_{iy}^2 + r_{iz}^2}$$

Accordingly, the magnetic energy density equation for the isotropic MREs given in the Eq. (2.18) can be cast into the following form for MREs with anisotropic chain-like particle distribution under simple shear:

$$E_m = -\frac{\phi^2 J_p^2 \beta}{4\pi\mu_0} \sum_i \left[ \frac{(2 - \gamma^2)\beta^2 r_{iy}^2 - r_{ix}^2 - r_{iz}^2 - 2\beta\gamma r_{ix} r_{iy}}{\left( (1 + \gamma^2)\beta^2 r_{iy}^2 + r_{ix}^2 + r_{iz}^2 + 2\beta\gamma r_{ix} r_{iy} \right)^{\frac{5}{2}}} \right] \quad (2.29)$$

In this relation, the condition of incompressibility, i.e.  $a_x a_y a_z = a_x^0 a_y^0 a_z^0$  is also applied. The only difference between Eq. (2.29) and Eq. (2.18) is the existence of parameter  $\beta$  which enables the anisotropic arrangement of particles in the model. Now replacing the magnetic energy part in Eq. (2.24) with that given in Eq. (2.29), one can obtain the total potential energy density function for the MREs with anisotropic configuration. Figure 2.14 presents the total potential energy versus strain for different values of parameter  $\beta=1, 0.95, 0.90, 0.85,$  and  $0.8$ , under constant magnetic flux density of  $B = 0.6$  T for MRE with 5% volume fraction of iron particles. Figure 2.15 shows the same result but at a constant value of  $\beta=0.9$  being subjected to  $0.0$  T,  $0.2$  T,  $0.4$  T,  $0.6$  T,  $0.8$  T, and  $1.0$  T magnetic flux density.

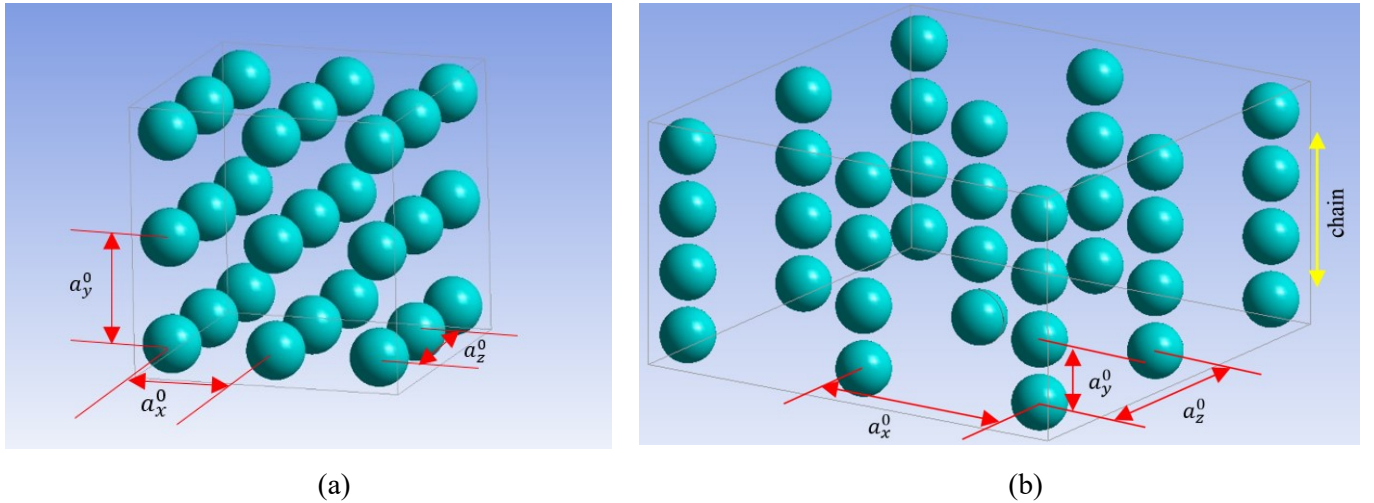


Figure 2.13 Schematic arrangement of particles in (a) isotropic configuration ( $a_x^0 = a_y^0 = a_z^0$ ) and (b) anisotropic (chain-like) configuration ( $a_y^0 < a_x^0 = a_z^0$ ).

It can be seen from Figure 2.14 and Figure 2.15 that the total potential energy density directly increases with the shear strain and its magnitude depends on both the value of parameter  $\beta$  as well as the strength of external magnetic flux density,  $B$ . According to Figure 2.14, at a constant strain level, the total potential energy tends to decrease even to negative values as  $\beta$  decreases from unity (particle distribution transforms more into chains). Similar trend of decreasing energy could be observed when the value of parameter  $\beta$  is



constant and the magnetic flux density increases in Figure 2.15. However, the rate of change of energy within a constant range of strain amplitude, is larger at higher fields which means higher MR effect.

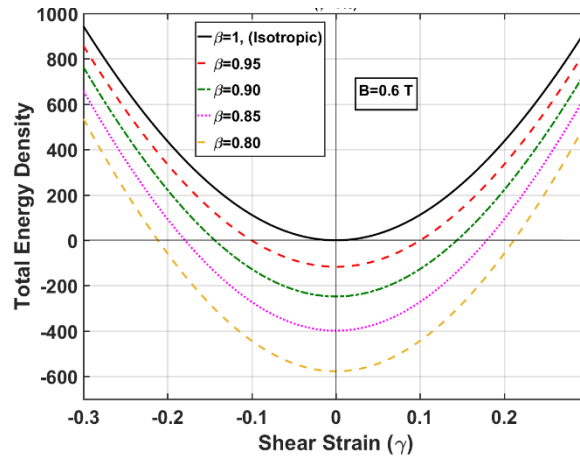


Figure 2.14 Total energy density versus strain for different values of  $\beta$  under 0.6 T magnetic flux density ( $k = 1$ ,  $s = 1$ ,  $\phi = 5\%$ ).

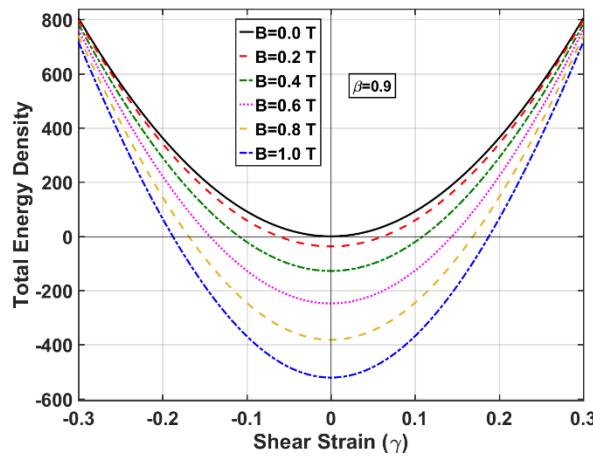


Figure 2.15 Total potential energy density versus strain under different levels of applied magnetic flux density and  $\beta = 0.9$  ( $k = 1$ ,  $s = 1$ ,  $\phi = 5\%$ ).

Using Eq. (2.25) with the modified total energy density function, the shear modulus can be calculated for the anisotropic MREs. Figure 2.16 shows the shear modulus versus external magnetic flux density changing from 0 T to 1 T for different values of parameter  $\beta$ . These results are indeed a comparison of range of change of shear modulus for the isotropic ( $\beta = 1$ ) and anisotropic ( $\beta < 1$ ) configuration of particles. Based on Figure 2.16, at lower values of  $\beta$ , greater increase in the shear modulus is observed with the magnetic flux density. Therefore, it could be concluded that the change of modulus with the applied field, i.e. the MR effect, is larger for anisotropic distribution of particles than isotropic dispersion. A similar trend has also been observed from the experiments as will be discussed later in the following sections.

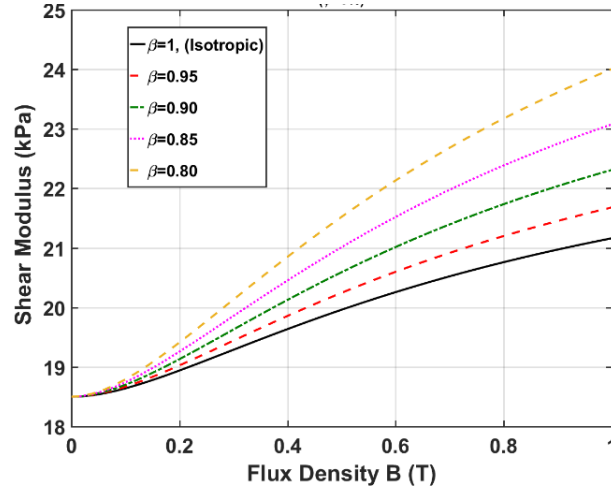


Figure 2.16 Shear modulus versus applied magnetic flux density for different values of  $\beta$  ( $k = 1$ ,  $s = 0.3$ ,  $\phi = 5\%$ ).

#### 2.4.4 Discussion on the properties of lattices

In this section, a detailed study is conducted on the properties of the proposed idealized arrangement of particles for isotropic and anisotropic distributions. First, the magnetic interaction of a pair of particles under a homogeneous applied magnetic field is investigated. Based on the energy values, attraction and repulsion of two magnetized particles caused by magnetic induction is explained. The interaction of two dipoles is then used as the basis to explain the effect of magnetic energy of the lattice on the mechanical properties of MREs.

Let us consider a pair of particles in the space as shown in Figure 2.17. External magnetic field is applied along the y-axis and the angle between the particles' centerline and the direction of the applied field is  $\theta$ . It is assumed that the two particles are magnetized and have magnetic moments of  $\mathbf{m}_1$  and  $\mathbf{m}_2$  so they are called a magnetic dipole pair. Assuming that the dipole moments are the same in value and direction,  $\mathbf{m}_1 = \mathbf{m}_2 = \mathbf{m}$ , Eq. (2.10) can be used to write the magnetic potential energy of the dipole pair as:

$$e_{12} = -\frac{|\mathbf{m}|^2}{4\pi\mu_1\mu_0} \left[ \frac{3(\mathbf{R}_{12})_y^2 - |\mathbf{R}_{12}|^2}{|\mathbf{R}_{12}|^5} \right] \quad (2.30)$$

where  $(\mathbf{R}_{12})_y = |\mathbf{R}_{12}| \cos(\theta)$ . In addition, Eq. (2.30) may also be expressed as:

$$e_{12} = \frac{|\mathbf{m}|^2}{4\pi\mu_1\mu_0} f(\theta, |\mathbf{R}_{12}|) \quad (2.31)$$

where  $f(\theta, |\mathbf{R}_{12}|) = \left[ \frac{1-3\cos^2(\theta)}{|\mathbf{R}_{12}|^3} \right]$  is an indication of the magnetic energy of dipoles and depends on the relative position of the particles in the space. In order to discuss the magnetic interaction of dipoles, function  $f(\theta, |\mathbf{R}_{12}|)$  is numerically computed for different configurations.

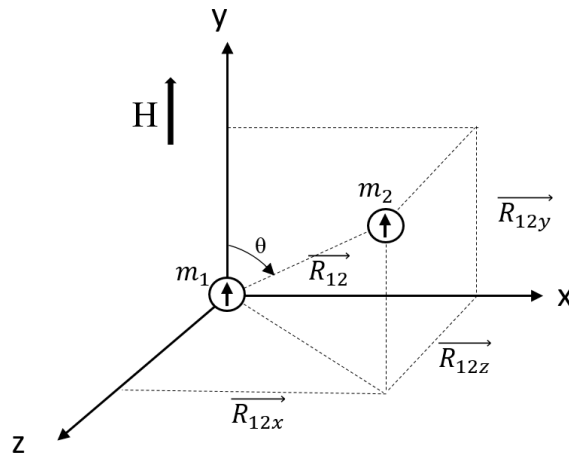


Figure 2.17 Two dipoles are located in the 3D space under an external magnetic field.

For the sake of simplicity, the magnetic dipole pair is assumed to be in a plane and value of function  $f(\theta, |\mathbf{R}_{12}|)$  is evaluated for different dipole pair configurations. Figure 2.18 shows the dipole pair in a plane in three different positions under an external magnetic field. In Figure 2.18 (a), two dipoles are aligned in the direction of external field, so the angle between their centerline and field direction is  $\theta = 0$ . Figure 2.18 (b) shows the dipole pair located normal to the field direction with  $\theta = 90^\circ$  and finally Figure 2.18 (c) shows two dipoles located in a position between the horizontal and vertical situations in which the angle  $\theta$  lies between 0 and  $90^\circ$ .

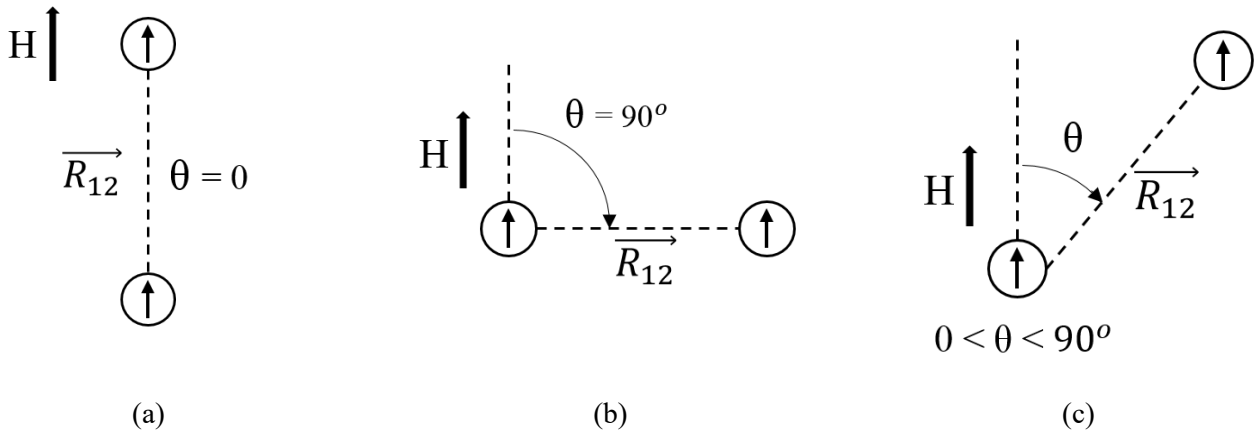


Figure 2.18 A pair of dipoles in three spatial positions; a) dipoles' centerline is parallel to the direction of field ( $\theta=0$ ), b) dipole's centerline is normal to the direction of field ( $\theta=90^\circ$ ), and c) dipole's centerline is oblique to the direction of field ( $0 < \theta < 90^\circ$ ).

Figure 2.19 shows the formulation and value of function  $f(\theta, |\mathbf{R}_{12}|)$  for the two situations of  $\theta = 0$  (Figure 2.18 (a)) and  $\theta = 90^\circ$  (Figure 2.18 (b)). For both cases, the value of function  $f$  which represents the magnetic potential energy between two dipoles, is inversely proportional to the cube of distance between two

particles. Thus, the magnetic interaction energy quickly dies out as the distance between dipoles increases. As it can be realized from Figure 2.19, the magnetic interaction energy is negative when  $\theta = 0$  which indicates that the two dipoles tend to attract each other (shown by the arrow on the blue curve) to decrease their level of energy. Therefore, there is an attractive force between two dipoles in this case. However, for the case with  $\theta = 90^\circ$ , the interaction energy is positive, and dipoles tend to move away from each other (arrow on the red curve) to decrease the energy to zero value where two dipoles are quite far from each other. Hence, a repulsive force exists between two dipoles in this position.

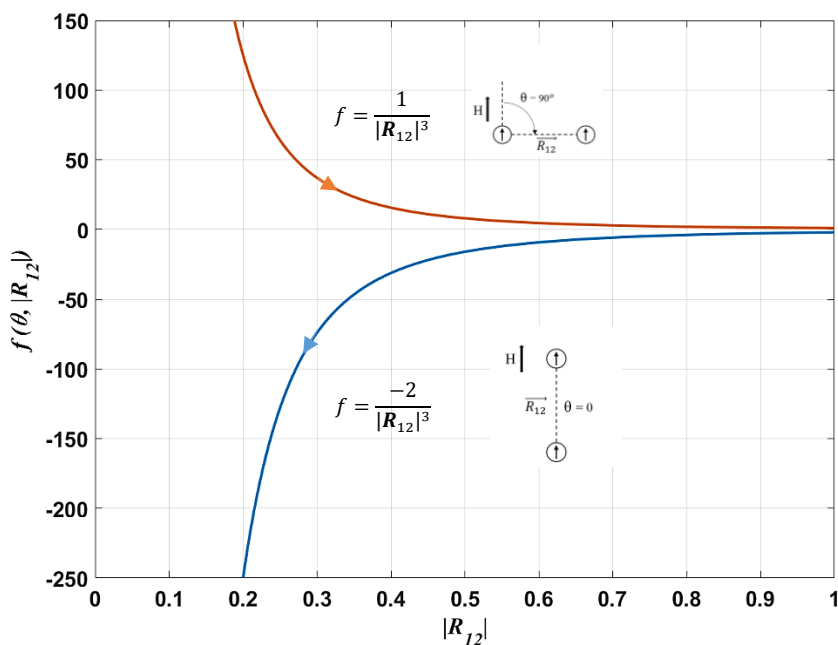


Figure 2.19 Value of function  $f(\theta, |R_{12}|)$  versus distance between two dipoles for the two situations illustrated in Figure 2.18 (a) and (b).

For the case in which  $0 < \theta < 90^\circ$ , we assume the distance of dipoles is constant and equals to unity and the value of  $f$  is evaluated as a function of the angle  $\theta$ . Figure 2.20 shows the variation of function  $f$  with respect to angle  $\theta$ . It is interesting to note that in the considered range of  $0 < \theta < 90^\circ$ , the magnetic energy between two dipoles becomes zero at  $\theta \cong 54.7^\circ$  where its sign changes from negative values at  $\theta < 54.7^\circ$ , to positive values at  $\theta > 54.7^\circ$ . Thus, as shown in Figure 2.20 (a), there is an attractive force between two dipoles for  $0 < \theta < 54.7^\circ$ ; while, for  $54.7^\circ < \theta < 90^\circ$ , there is a repulsive force between dipoles. At  $\theta \cong 54.7^\circ$  no magnetic interaction exists between two dipoles, so they neither attract nor repel each other.

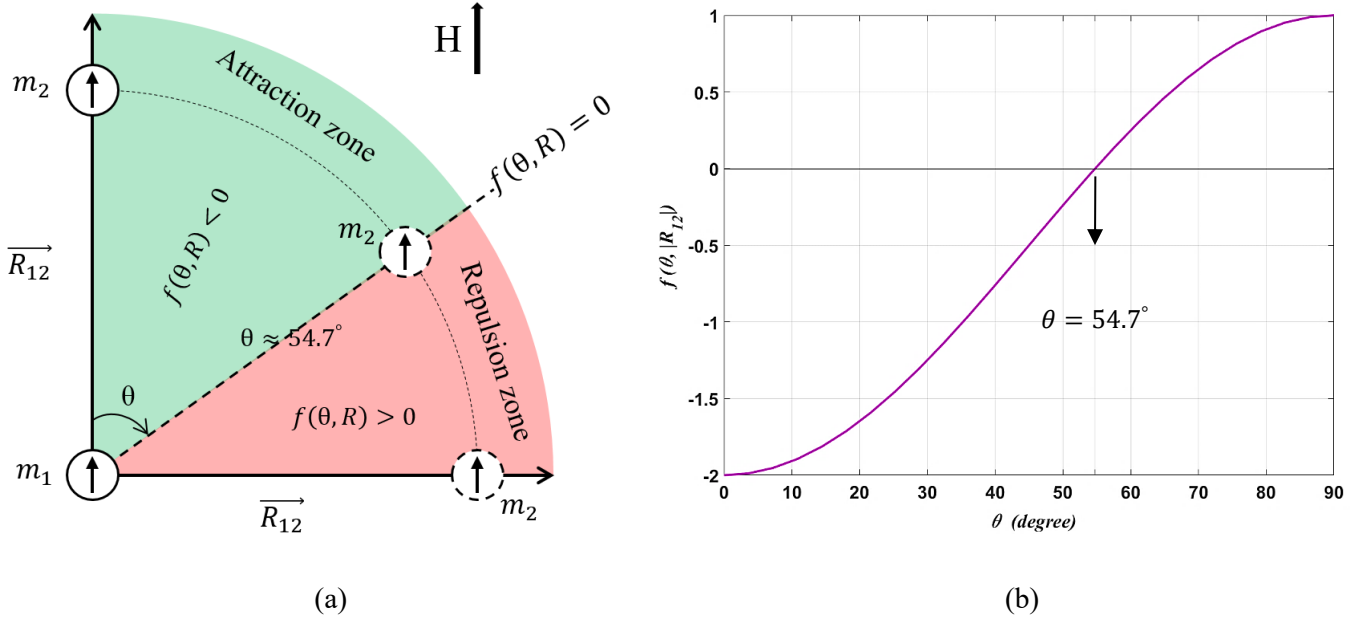


Figure 2.20 (a) Change in the sign of function  $f$  with the angle  $\theta$  between dipoles' centerline and field direction.  $f < 0$  means two dipoles tend to attract each other (attraction zone) and  $f > 0$  means two dipoles tend to repel each other (repulsion zone). (b) Change in the value of function  $f$  with respect to angle  $\theta$ .

Having the physical understanding about the dipoles' magnetic interaction, change in the stiffness of a material incorporating the magnetic particles as well as the reason behind the properties of the proposed lattices could be explained. Assume a network of particles are magnetized under an applied magnetic field. Then, less mechanical energy is required than normal situation, without magnetic field being applied, if the mechanical deformation put the particle network into a new situation with reduced level of magnetic energy. This situation is similar to the cases that we want to make the vertical dipoles in Figure 2.18 (a) closer to each other or to move away the horizontal dipoles in Figure 2.18 (b) from one another. On the other hand, more mechanical effort is required to change the arrangement of particles into a situation with higher level of magnetic energy. Higher required mechanical effort means the material is stiffer and vice versa.

Figure 2.21 shows the magnetic part of the energy evaluated using Eq. (2.18) versus applied shear strain for each of the proposed lattices in Figure 2.8 for  $\phi = 5\%$  volume fraction of particles at constant magnetic flux density of  $B=0.1$  T and unit values of parameters  $k$  and  $s$ . It is observed from Figure 2.21 that upon application of a shear deformation, particle network of the BCC and FCC lattices transform to new configurations with lower magnetic energy. It means that the shear deformation agrees with the natural tendency of particles to decrease their magnetic energy under the applied field and so lower mechanical effort is required to deform the material. This clearly shows why the shear moduli of these two lattices decrease with the magnetic field intensity as shown in Figure 2.12. However, for the other lattices, shear deformation

brings particles into a new arrangement with higher level of magnetic energy which is against the particles' natural tendency. Therefore, higher mechanical effort is required to deform the particle network. The relative changes in the magnetic energy of different lattices in the deformed situation is the reason for various level of MR effect resulted from each lattice type. For instance, the ECC lattice shows the higher level of magnetic energy at a specific strain level and so it has a larger MR effect as shown in Figure 2.12. Similar explanation could be used to justify the increase of shear modulus in case of anisotropic distribution of particles in comparison with isotropic dispersion.

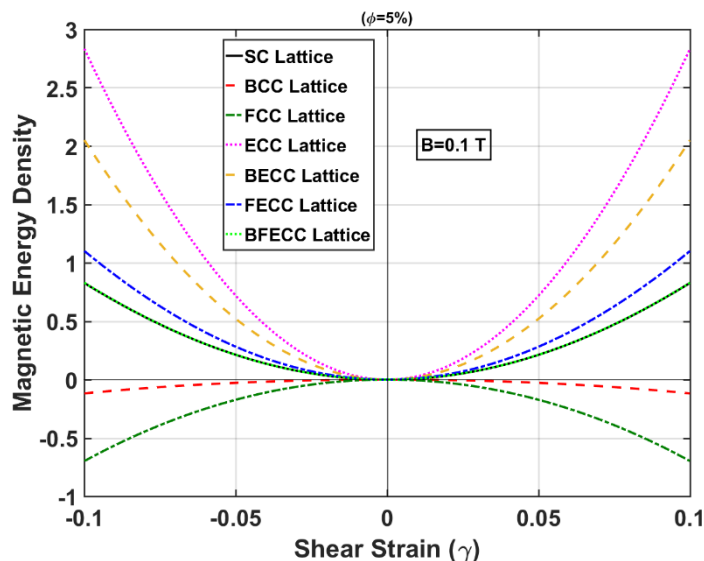


Figure 2.21 Magnetic interaction energy of particle network for MRE with  $\phi = 5\%$  arranged according to different lattice types ( $B = 0.1 \text{ T}$ ,  $k = 1$ ,  $s = 1$ ).

The above discussion could be also explained physically by comparing the unit cell of lattices when they are subjected to a shear deformation. Figure 2.22 shows two unit cells of the BCC lattice in undeformed and deformed situations. In the undeformed position, two particles at the center of unit cells locate on the diagonal lines that makes angle of  $\theta_1 = \theta_2 = 54.7^\circ$  with the direction of field. So, there is no magnetic interaction between these particles and the origin. However, when a shear deformation is applied, the particle in the left unit cell comes to the attraction zone ( $\theta'_1 < 54.7^\circ$ ) and the one in the right side comes to the repulsion zone ( $\theta'_2 > 54.7^\circ$ ). Therefore, small values of shear deformation help the natural tendency of particles for getting closer to each other in the attraction zone or to move them away from one another in the repulsion zone. This clearly shows why lower mechanical effort is required to make a shear deformation for a BCC lattice than a SC lattice.

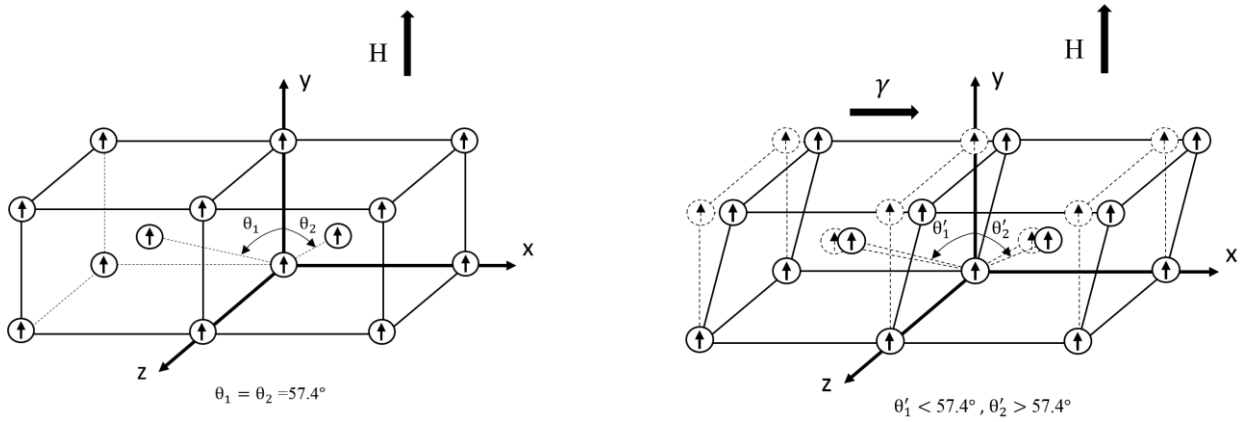


Figure 2.22 Two unit-cells of BCC lattice in undeformed (left) and deformed (right) situations.

## 2.5 Comparison of Model Results with Experiments

In order to evaluate the performance of the proposed microscale models, the shear modulus obtained from the models are compared with those experimentally measured. As it was mentioned in Section 2.2.2, experimental tests have been performed by sweeping the shear strain amplitude in the range of 0.001 % to 30 % while maintaining the driving frequency at 0.1 Hz. Here, the shear storage modulus of the MRE samples at the strain amplitude of 0.01% are utilized as the reference data to evaluate the performance of the developed model. It should be noted that the MREs operate in linear viscoelastic region at this shear strain amplitude (0.01%) and the storage modulus is independent of the strain amplitude in this region. Optimal values of fitting parameters of the models are found using the least square optimization method. For the isotropic MREs, performance of the model is evaluated by measuring the root mean square error (RSME) for each of the lattices. For the anisotropic sample, the range of change of modulus predicted using the proposed model is compared with that obtained experimentally and also for similar isotropic MRE sample with the same level of particle volume fraction.

### 2.5.1 Isotropic MREs

Among the lattice models proposed in the Section 2.4.2 for isotropic distribution of particles in MRE materials, those that exhibited increase of the shear modulus with magnetic flux density, i.e. SC, ECC, BECC, FECC, and BFECC, are selected for predicting the shear modulus of fabricated isotropic MRE samples (Table 2.1) in terms of applied magnetic field. Optimal values of fitting parameters of the model,  $k$  and  $s$ , are found for each sample of MRE using least square optimization method to minimize the error between simulation and experiential results and thus to make the best fit between the model results and those measured experimentally. Figure 2.23 and Figure 2.24 show the experimental and theoretical results of the shear

modulus versus magnetic flux density for the SC and ECC lattice models, respectively. Values of parameters  $k$  and  $s$  for different volume fraction of iron particles are reported in Table 2.3.

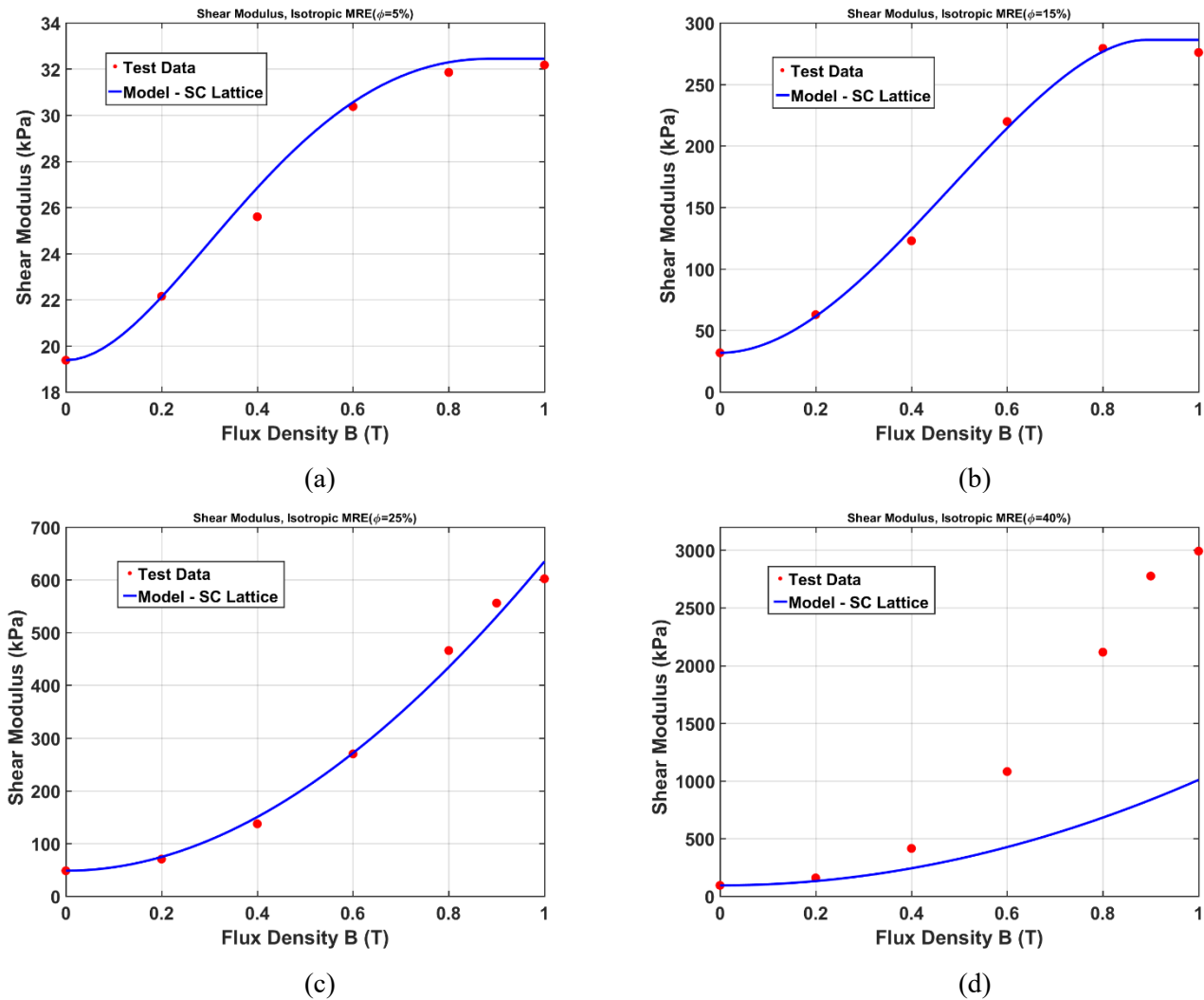


Figure 2.23 Comparison between the experimental data and model results using SC lattice for four isotropic MRE samples with different volume fraction of particles (a) Sample 1 ( $\phi = 5\%$ ), (b) Sample 2 ( $\phi = 15\%$ ), (c) Sample 3 ( $\phi = 25\%$ ), and (d) Sample 4 ( $\phi = 40\%$ ).

Results in Figure 2.23 show that for MRE samples with 5%, 15%, and 25% volume fraction of iron particles, the simple cubic lattice can suitably predict the variation of shear modulus with respect to the applied magnetic flux density up to high flux density values and saturation point. However, for the Sample 4 with  $\phi = 40\%$ , simulation based on SC lattice model does not agree with the experimental data for magnetic flux density beyond 0.2 T as shown in Figure 2.23 (d). Examination of results in Figure 2.24 reveals that the ECC lattice model is capable of predicting the variation of shear modulus of MRE samples versus external magnetic flux density irrespective of their volume fraction of iron particles. The superiority of ECC lattice in predicting the field dependent shear modulus of MREs with high content of particles in comparison



with the SC lattice can also be better realized from Figure 2.12 where the ECC lattice showed the maximum MR effect among the proposed lattices. Indeed, the SC lattice cannot represent the dense configuration of particles at high volume fractions such as  $\phi = 40\%$ . However, the ECC lattice is a better idealized representation of particles distribution at high volume fractions and could better predict the shear modulus test data.

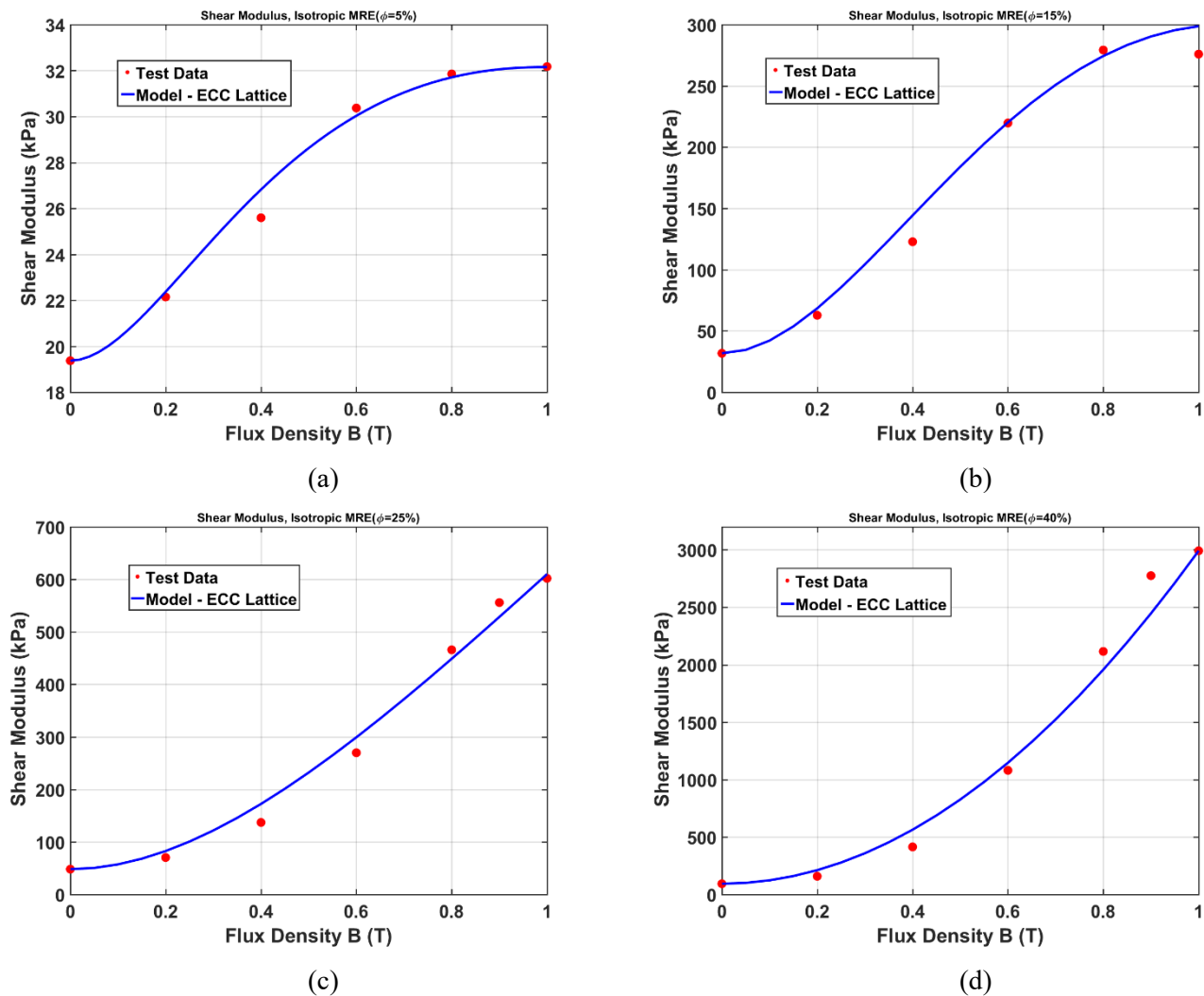


Figure 2.24 Comparison between experimental data and model results using ECC lattice for four isotropic MRE samples with different volume fraction of particles (a) Sample 1 ( $\phi = 5\%$ ), (b) Sample 2 ( $\phi = 15\%$ ), (c) Sample 3 ( $\phi = 25\%$ ), and (d) Sample 4 ( $\phi = 40\%$ ).

The performance of each lattice model and its agreement with the experimental data can be evaluated by using root mean square error (RMSE) index calculated as follows:

$$\text{RMSE} = \sqrt{\frac{\sum_i^n \left( \frac{G_m - G_{exp}}{G_{exp}} \right)^2}{n}} \quad (2.32)$$

where  $G_m$  is the value of shear modulus predicted by the model and  $G_{exp}$  is that of experimental test.  $n$  is the number of experimental data points available for each MRE sample. Table 2.4 compares the results of shear modulus at different magnetic flux density levels predicted by the model using each of the lattice types with the experimental data for four isotropic MRE samples. The corresponding RMSE value for each lattice type is also given in the last column. In addition, the absolute value of error between the model prediction,  $G_m$ , and experimental data,  $G_{exp}$ , at each magnetic flux density level is presented in the bar charts in Figure 2.25 for the four isotropic samples to have more clear comparison of the performance of different lattices.

According to the results in Table 2.4 and bar charts of Figure 2.25, the performance of SC lattice at lower participation of iron particles ( $\phi = 5\%$  and  $15\%$ ) is better compared to the ECC lattice. However, at higher particle content, particularly for Sample 4 with  $\phi = 40\%$ , the SC lattice could not predict the change in modulus at high magnetic field and ECC lattice shows better agreement with experimental data. This observation suggests that different lattice models might be proper to be used for representing the distribution of particles for different MRE samples with various amounts of particle content. In another word, not a single lattice type could be used as the best representation of particles' dispersion for all particle participation levels.

For other lattices, i.e. BECC, FECC, and BFECC, which are combinations of basic lattice types, the error of model for the samples with moderate particle content is roughly of the same order. For the Sample 4, the BECC lattice shows the lowest error among these three lattices and also compared to the SC lattice; however, its performance at higher field levels beyond 0.6 T is not as satisfactory as the performance of the ECC lattice. As discussed before in Figure 2.12 and Figure 2.21, the BFECC lattice has similar magnetic energy density behavior as the SC lattice, thus they show the same level of RMSE error as expected.

Table 2.3 Values of constant parameters used in the model.

	MRE Sample Type	$k$	$s$
SC lattice	Sample 1 ( $\phi = 5\%$ )	2.90	1.0
	Sample 2 ( $\phi = 15\%$ )	30.0	1.60
	Sample 3 ( $\phi = 25\%$ )	4.30	4.90
	Sample 4 ( $\phi = 40\%$ )	30.0	20.0
		$k$	$s$
ECC lattice	Sample 1 ( $\phi = 5\%$ )	1.50	0.45
	Sample 2 ( $\phi = 15\%$ )	2.60	0.80
	Sample 3 ( $\phi = 25\%$ )	1.0	1.0
	Sample 4 ( $\phi = 40\%$ )	8.20	17.65

Table 2.4 Values of the shear modulus at different magnetic flux densities obtained using different lattice models and comparison with the experimental data.

Lattice type	MRE Sample	Shear Modulus at $B=0.2$ T (kPa)		Shear Modulus at $B=0.4$ T (kPa)		Shear Modulus at $B=0.6$ T (kPa)		Shear Modulus at $B=0.8$ T (kPa)		Shear Modulus at $B=1.0$ T (kPa)		RMSE (%)
		Model	Test	Model	Test	Model	Test	Model	Test	Model	Test	
SC lattice	Sample 1	22.11	22.14	26.84	25.59	30.55	30.37	32.29	31.85	32.29	32.17	2.30
	Sample 2	61.42	62.76	131.91	122.81	214.39	219.71	276.60	279.29	276.60	275.91	3.64
	Sample 3	74.34	70.34	150.10	137.14	271.43	269.86	434.33	465.86	634.80	601.98	6.29
	Sample 4	130.74	158.33	241.90	413.97	426.07	1080.25	682.37	2115.84	1009.9	2991.62	54.18
ECC lattice	Sample 1	22.38	22.14	26.85	25.59	30.07	30.37	31.75	31.85	32.20	32.17	2.29
	Sample 2	68.58	62.76	144.65	122.81	220.93	219.71	275.24	279.29	299.63	275.91	9.78
	Sample 3	82.80	70.34	172.82	137.14	300.13	269.86	450.22	465.86	612.0	601.98	15.04
	Sample 4	211.96	158.33	565.24	413.97	1150.10	1080.25	1963.40	2115.84	3001.8	2991.62	22.99
BECC lattice	Sample 1	21.96	22.14	26.17	25.59	29.55	30.37	31.58	31.85	32.40	32.17	1.69
	Sample 2	67.94	62.76	144.20	122.81	220.36	219.71	269.70	279.29	280.05	275.91	8.78
	Sample 3	74.94	70.34	151.12	137.14	270.88	269.86	428.73	465.86	619.55	601.98	6.61
	Sample 4	184.50	158.33	456.06	413.97	905.99	1080.25	1532.10	2115.84	2332.30	2991.62	19.41

Table 2.4 Continue...

Lattice type	MRE Sample	Shear Modulus at $B=0.2$ T (kPa)		Shear Modulus at $B=0.4$ T (kPa)		Shear Modulus at $B=0.6$ T (kPa)		Shear Modulus at $B=0.8$ T (kPa)		Shear Modulus at $B=1.0$ T (kPa)		RMSE (%)
		Model	Test	Model	Test	Model	Test	Model	Test	Model	Test	
FECC lattice	Sample 1	22.11	22.14	26.79	25.59	30.51	30.37	32.41	31.85	32.62	32.17	2.33
	Sample 2	64.71	62.76	139.57	122.81	220.70	219.71	272.82	279.29	272.82	275.91	6.37
	Sample 3	74.62	70.34	150.58	137.14	271.11	269.86	431.38	465.86	626.67	601.98	6.40
	Sample 4	142.81	158.33	289.98	413.97	533.82	1080.25	873.15	2115.84	1306.80	2991.62	45.11
BFECC lattice	Sample 1	22.11	22.14	26.85	25.59	30.56	30.37	32.29	31.85	32.29	32.17	2.30
	Sample 2	61.42	62.76	131.91	122.81	214.39	219.71	276.60	279.29	276.60	275.91	3.64
	Sample 3	74.34	70.34	150.10	137.14	271.43	269.86	434.33	465.86	634.80	601.98	6.29
	Sample 4	130.74	158.33	241.90	413.97	426.07	1080.25	682.37	2115.84	1009.90	2991.62	54.18

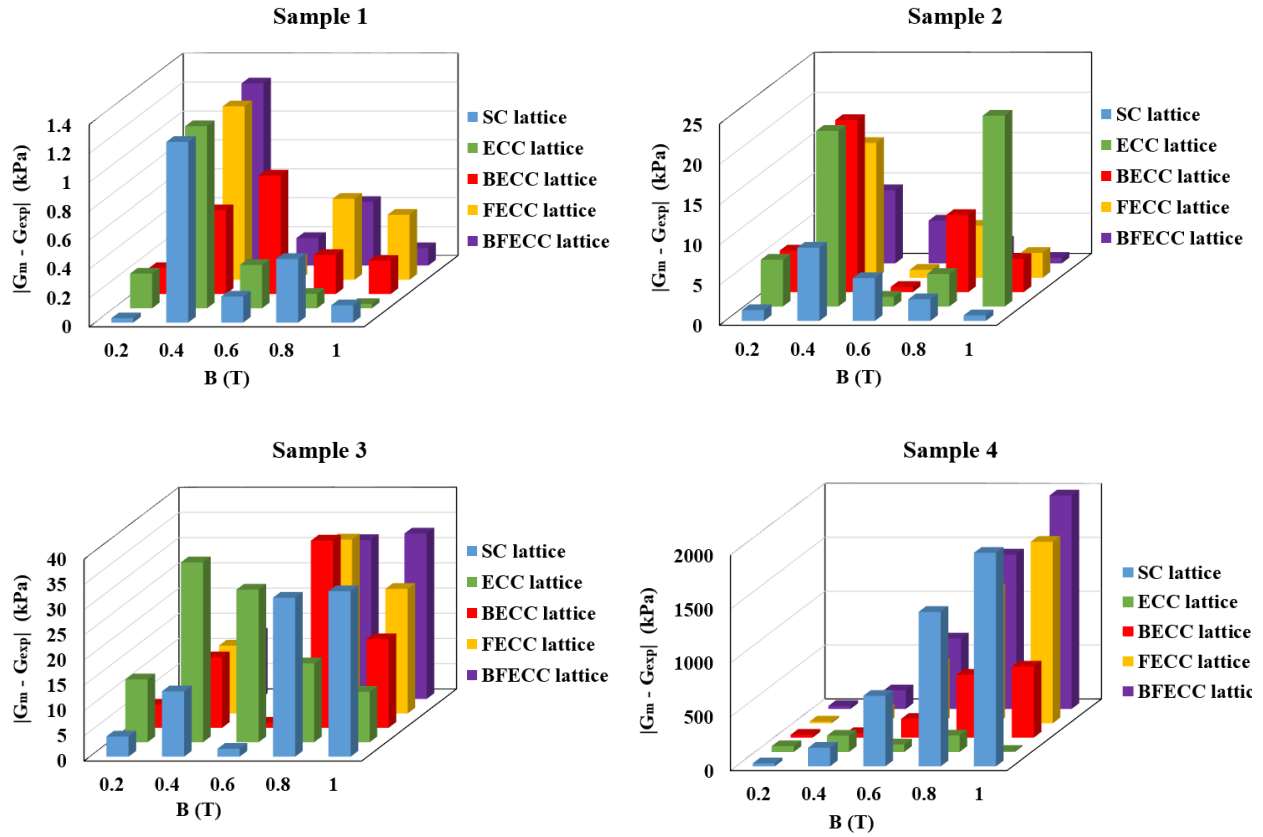


Figure 2.25 Error between lattice models prediction,  $G_m$ , and experiment data,  $G_{exp}$ , for four isotropic MRE Samples 1, 2, 3, and 4.

## 2.5.2 Anisotropic MREs

As discussed before in the section 2.4.3, the magnetic energy density for anisotropic MREs with chain-like particle distribution can be obtained using Eq. (2.29). Combining Eq. (2.29) with the elastic energy given in Eq. (2.3) and then using Eq. (2.25), we can obtain shear modulus of MRE samples with chain-like distribution of particles versus applied magnetic field. Figure 2.26 shows the results of shear modulus versus magnetic flux density for anisotropic MRE (Sample 6) and its comparison with isotropic MRE (Sample 5) with the same level of iron volume fraction ( $\phi = 15\%$ ). For the isotropic sample, the value of  $\beta=1$  corresponding to simple cubic lattice is used in Eq. (2.29). For the anisotropic sample,  $\beta=0.54$  corresponding to chain-like structure of particles is obtained from least square optimization technique. Other fitting parameters are reported in Table 2.5.

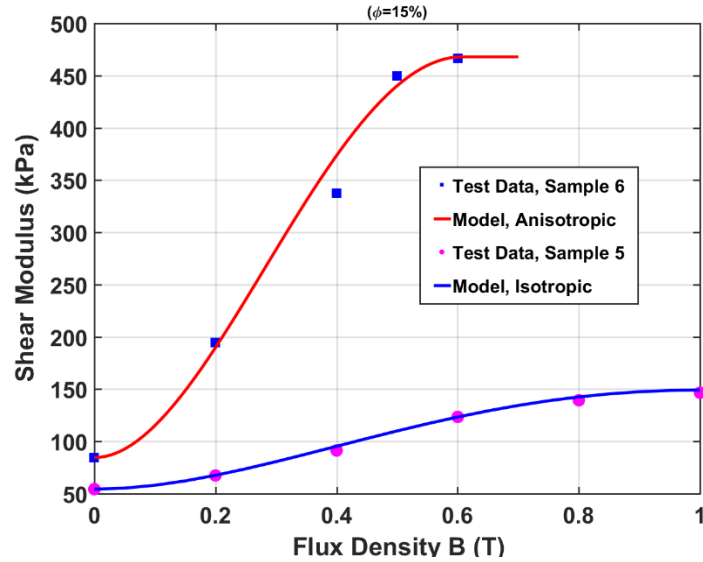


Figure 2.26 Comparison of the model and experimental results of the shear modulus versus magnetic flux density for isotropic (Sample 5) and anisotropic (Sample 6) MREs.

Table 2.6 also presents the initial shear modulus of the isotropic and anisotropic MRE samples at zero field and maximum change in the modulus obtained by applying the magnetic flux density in the considered range. According to Figure 2.26 and Table 2.6, a considerable improvement is observed in the stiffness of the anisotropic MRE in comparison with the similar isotropic one by the application of the magnetic field. In other words, putting particles arrangement into chains, not only increases the initial modulus of the material at zero field, but also greatly improves the MR effect. The anisotropic sample saturates at lower fields compared with its isotropic counterpart. The model shows an acceptable performance in predicting the variation of shear modulus for both isotropic and anisotropic MREs.

Table 2.5 Optimal values of the parameters used in the model.

MRE Sample Type		$k$	$s$	
Isotropic (SC lattice)	Sample 5 ( $\phi = 15\%$ )	3.30	0.90	
		$k$	$s$	$\beta$
Anisotropic (Chain-like)	Sample 6 ( $\phi = 15\%$ )	7	0.8	0.54

Table 2.6 Shear modulus at zero field and the experimental and predicted range of change of modulus.

MRE Sample Name	Shear Modulus at Zero Field (kPa)	Maximum Change in Modulus From Experiment (kPa) (%Change)	Maximum Change in Modulus Calculated by Model (kPa) (%Change)
Isotropic, Sample 5 ( $\phi = 15\%$ )	54.43	92.16 (169%)	94.81 (174%)
Anisotropic, Sample 6 ( $\phi = 15\%$ )	84.59	381.52 (451%)	383.23 (453%)

## 2.6 Conclusions

In this chapter, the quasi-static magneto-mechanical properties of isotropic and anisotropic MREs in terms of particles' spatial distribution, particles' volume fraction, and magnetic induction intensity have been investigated. Experimental characterization in shear mode was carried out by using an advanced rheometer equipped with an MR device. Theoretical modeling was performed based on microscale modeling approach incorporating different lattice types as idealized distribution of magnetic particles in the material. Depending on the spatial distribution of particles according to different lattices, various levels of magneto-induced change in shear modulus was observed. Some of the proposed lattices exhibited decrease in the shear modulus with the applied magnetic field which is in contradiction with experimental test results.

Moreover, a thorough investigation has been conducted on the magnetic interaction of particles which is the basis for variation in the properties of MREs under applied magnetic field. For the anisotropic MREs, idealized chain-like structure of particles is incorporated into the model which results in higher MR effect in comparison with isotropic distribution. Results obtained using microscale modeling approach based on proposed lattice types are compared with experimental data for several MRE samples. For the isotropic MREs, the performance of the lattices was evaluated quantitatively by considering the RMSE for each case. For the anisotropic MRE, the idealized chain-like structure of particles in the model exhibited good agreement with experimental results.



## CHAPTER 3

# ADAPTIVE DYNAMIC MODULI OF MAGNETORHEOLOGICAL ELASTOMERS: FROM EXPERIMENTAL IDENTIFICATION TO MICROSTRUCTURE-BASED MODELING

### 3.1 Introduction

In this chapter, the developed knowledge on microstructure modelling of MREs in Chapter 2 is extended to formulate a novel physic-based microstructure modeling approach to investigate the dynamic magneto-mechanical properties of MREs. This is important as MREs are generally under oscillatory mechanical loading in most practical applications such as in MRE-ATVAs [68], [80] and MR isolators [7], [81].

The influence of magnetic particles content, magnetic field strength, frequency, and strain amplitude on the viscoelastic properties of MREs, such as dynamic moduli and loss factor, have been experimentally investigated in different research studies [9], [27]. It has been shown that both the storage and loss moduli of an MRE increase steadily with increasing excitation frequency in the linear viscoelastic region [9], [27]. Moreover, the dynamic performance of the MRE was observed to be improved by the increment of iron particles quantity up to a certain extent [89]. Regarding the magnetic field intensity, it is reported that the material response is dominated by the polymeric matrix at low magnetic fields (up to 75 mT) while above a certain magnetic flux density (200 mT for a sample composed of 40% volume fraction of CIPs) the magneto-reinforced microstructure dominates the MR elastomer's behavior [25]. The viscoelastic response of isotropic and anisotropic MREs in squeeze mode were observed to be nonlinear under high static pre-strain according to the shape of stress-strain hysteresis loops [26]. This nonlinearity intensifies with increasing the strain amplitude.

Experimental characterization of MREs requires operation of sophisticated commercial testing machines sometimes with self-developed fixtures and magnets which could be very time consuming and financially expensive. On the other hand, efficient utilization of MREs in practical applications while having control on the material properties is not possible without having in-depth knowledge on the material response under various operating conditions. Therefore, several

attempts have been made on development of models capable of predicting dynamic behavior of MREs within a given range of operating conditions.

Several phenomenological models have been presented in the literature which usually employ viscoelastic parametric elements such as Maxwell, Bouc-Wen, and Voigt elements or parametric mathematical formulations to represent the viscoelastic characteristics of the material [48], [49], [90]–[92]. These models use several parameters which usually have to be evaluated repeatedly for new operating conditions, e.g. change in the magnetic field, material, etc. Moreover, the parameters do not have certainly a physical meaning and they are not able to interpret material's dynamic behavior. Some recent research studies have tried to overcome the limitations of the phenomenological models by combining a fractional viscoelastic model with a microstructural dipole model [93]; however, these models still could not well explain the variation in dynamic properties of the MREs from the internal structure point of view. Physical microscale-based modeling approaches consider the interaction of embedded magnetized fillers (dipoles) at the microstructure level and could address the isotropic or anisotropic distribution of particles in the host carrier matrix. A coarse grained network model has been proposed by Ivaneyko et al. [65], [66] as discussed in CHAPTER 1, however, due to its limitations, the model cannot be used in practical applications for a wide range of frequency and magnetic field.

In the present chapter, a novel magneto-dynamic microstructure-based model is developed based on the relaxation behavior of the embedded particles inside the matrix presented by Ivaneyko et al. [65], [66]. The model is used to predict the storage and loss moduli of MRE materials with various particle participation rate and is validated with experimental storage and loss moduli data of MREs in a broad frequency and magnetic field range up to the saturation point. First, cubic and chain-like lattice of magnetic particles embedded in an elastomeric medium, as investigated in Chapter 2, are utilized to model the isotropic and anisotropic configuration of magnetic particles in the network, respectively. Similar to the coarse grained network models proposed by Ivaneyko et al. [65], [66], particles are considered to be connected with springs representing the elasticity of the host matrix and each particle has a viscous constant providing the damping effects associated with particles' motion and that of the material. The governing equations of motion of the particles (Langevin equations) in the network are subsequently derived using Lagrange's equations to study the relaxation times of the particles network under magnetic induction. A dipole magnetic saturation formula is then introduced into the model to relate the eigenvalues and relaxation times

to the magnetic flux density,  $B$ , which is directly measurable in practice. The information of relaxation times is used in the relaxation modulus formulation to find the storage and loss moduli of the MRE as a function of frequency, magnetic flux density, volume fraction of particles, and the elastic properties of the host matrix. The material model parameters are finally estimated using the experimental data. For this purpose, isotropic and anisotropic MRE samples with different volume fraction of iron particles have been fabricated and then experimentally characterized under wide range of excitation frequencies and external flux densities using an advanced rheometer device integrated with electromagnet cell. Finally, the theoretical results based on the proposed model are compared with empirical data.

### **3.2 Magneto-Dynamic Microstructure-based Modeling**

In this section, after defining an ideal distribution of particles in a cubic network, the governing equations of motion of the particles will be first developed in Cartesian coordinates and then transferred to normal coordinates. Governing equations will be solved to evaluate the relaxation time spectrum of particles motion which will be subsequently utilized to calculate the dynamic moduli of the MRE materials.

#### **3.2.1 Defining Ideal Distribution of Particles in Cubic Network**

An ideal distribution of particles arranged as a cubic network is considered in the microstructure-based modeling of the MRE materials. Figure 3.1 shows schematically a sample of ideally arranged cubic network of particles in equally spaced isotropic structure and in chain-like anisotropic configuration. Particles are located at sites of the cubic network and connected with springs with elasticity constants of  $K_x$ ,  $K_y$ ,  $K_z$  which represent the elasticity of the three dimensional network. In addition, a friction constant  $\zeta$  is assigned to each particle which provides the effects of interfacial and intersegmental viscous friction in the composite polymer material. Magnetic field is applied on the particle network in vertical direction along  $y$  axis.

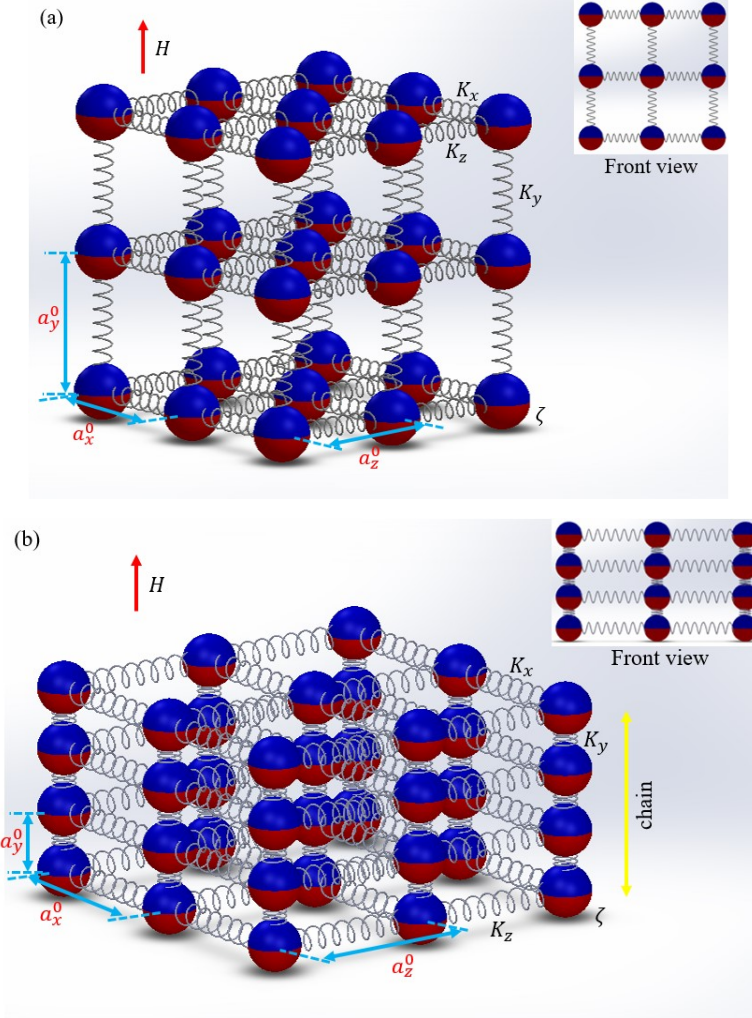


Figure 3.1 Ideal arrangement of magnetic particles in (a) equally spaced isotropic configuration (b) chain-like anisotropic configuration.

As it can be seen in Figure 3.1, the distance of adjacent particles in  $x$ ,  $y$ ,  $z$  directions are the same for isotropic dispersion, thus  $a_x^0 = a_y^0 = a_z^0 = a_0$ . For the chain-like anisotropic distribution, the vertical distance is smaller, i.e.  $a_y^0 < a_x^0 = a_z^0$  and the horizontal distance is smaller for the plane-like dispersion of particles. i.e.  $a_y^0 > a_x^0 = a_z^0$ . Similar to Eq. (2.26), the parameter  $\beta$  is employed to show the anisotropy level of the particle network, defined as:

$$\beta = \frac{a_y^0}{a_x^0} \quad (3.1)$$

where  $\beta = 1$ , corresponds to the isotropic configuration and  $\beta < 1$  presents the chain-like distribution of particles.  $\beta > 1$  stands for particles forming a plane-like anisotropic structure which

is not the concern of the present research study. Considering one unit cell, the volume fraction of particles in the medium as also defined in the Section 2.4.3 can be expressed as:

$$\phi = \frac{v_0}{a_x^0 a_y^0 a_z^0} \quad (3.2)$$

where  $v_0 = \frac{4}{3}\pi r^3$  is the volume of one particle. For the isotropic dispersion, volume fraction simplifies to  $\phi = \frac{4}{3}\pi \left(\frac{r}{a_0}\right)^3$ . The elasticity constants of the springs in the general anisotropic network are as  $K_y \neq K_x = K_z$  because the distance between adjacent particles in the vertical and horizontal directions are different. For the isotropic network, however, the elasticity coefficients take equal values as  $K_y = K_x = K_z = K_0$ . Therefore, for the base isotropic cubic particle network,  $a_0$  is the edge of unit cell and  $K_0$  is the isotropic spring coefficient. Using the equivalent spring constant formula of  $K_i = E_i A_i / L_i$ , the spring constants for the case of anisotropic network can be related to the edge size of the cells as [66]:

$$\begin{aligned} K_y &= \frac{K_0 a_x^{02}}{a_0 a_y^0} \\ K_x = K_z &= \frac{K_0}{a_0} a_y^0 \end{aligned} \quad (3.3)$$

It should be noted that the corresponding isotropic MRE has the same volume fraction of particles as the considered anisotropic MRE, i.e.  $\phi_{iso} = \phi_{aniso}$ , thus the edge sizes of the unit cells are related as  $a_x^0 a_y^0 a_z^0 = (a_0)^3$ . Now, considering  $a_x^0 = a_z^0$  and Eq. (3.1), it can be shown that  $a_y^0/a_0 = \beta^{2/3}$  and  $a_z^0/a_0 = a_x^0/a_0 = \beta^{-1/3}$ . Thus, the spring constants can be related to the anisotropic parameter  $\beta$  as:

$$\frac{K_y}{K_0} = \beta^{-4/3}; \frac{K_x \text{ (or } K_z)}{K_0} = \beta^{2/3}; \frac{K_y}{K_x} = \beta^{-2} \quad (3.4)$$

For the base isotropic arrangement of particles, shear modulus of elasticity  $G_0$  of the material at zero magnetic field can be related to the parameters of the network. Considering a unit cell of the cubic network under shear deformation,  $G_0$  can be expressed in terms of isotropic spring coefficient  $K_0$  and edge of isotropic unit cell  $a_0$  as:

$$G_0 = \frac{K_0}{a_0} \quad (3.5)$$

### 3.2.2 Dynamic Equations of Motion

Brownian dynamics is used in the microstructure-based model to describe the motion of particles. We use the terms of energy to formulate the equation of motion of a particle by the Lagrange's equations. The kinetic energy  $T(\mathbf{r}_n)$  of the  $n$ -th particle (network junction) can be expressed as:

$$T(\mathbf{r}_n) = \frac{1}{2} m_p \dot{\mathbf{r}}_n^2 \quad (3.6)$$

where  $m_p$  and  $\mathbf{r}_n$  are the mass and position vector of a particle, respectively.  $\dot{\mathbf{r}}_n = d\mathbf{r}_n/dt$  is the time derivative of the position vector. The index  $\mathbf{n} = (n_x, n_y, n_z)$  runs over the junctions of the network and numerates all the particles. Elastic energy  $U_{\text{elast}}(\mathbf{r}_n)$  and magnetic energy  $U_{\text{magn}}(\mathbf{r}_n)$  of the  $n$ -th particle with a position vector of  $\mathbf{r}_n = (r_{n_x}, r_{n_y}, r_{n_z})$  can be also expressed in the general form as below [18], [74]:

$$U_{\text{elast}}(\mathbf{r}_n) = \frac{1}{2} K_x \sum_{n'_x} C_{nn'} (r_{n_x} - r_{n'_x})^2 + \frac{1}{2} K_y \sum_{n'_y} C_{nn'} (r_{n_y} - r_{n'_y})^2 + \frac{1}{2} K_z \sum_{n'_z} C_{nn'} (r_{n_z} - r_{n'_z})^2 \quad (3.7)$$

$$U_{\text{magn}}(\mathbf{r}_n) = -\frac{1}{4\pi\mu_0} v^2 J_p^2 \sum_{n'} \frac{3(r_{n_y} - r_{n'_y})^2 - |\mathbf{r}_n - \mathbf{r}_{n'}|^2}{|\mathbf{r}_n - \mathbf{r}_{n'}|^5} \quad (3.8)$$

The connectivity parameter  $C_{nn'}$  in Eq. (3.7) is equal to unity if  $n$ - and  $n'$ -th particles are connected by a spring and is 0 otherwise.  $J_p$  in Eq. (3.8) is the particle polarization which will be formulated in terms of the flux density ( $B$ ) in the following and  $\mu_0$  stands for the vacuum permeability. Eq. (3.8) is similar to Eq. (2.15) in CHAPTER 2. Total potential energy of the particle is thus the summation of elastic and magnetic energy as:

$$U(\mathbf{r}_n) = U_{\text{elast}}(\mathbf{r}_n) + U_{\text{magn}}(\mathbf{r}_n) \quad (3.9)$$

The dissipative term of the energy associated with interfacial and intersegmental friction in the motion of a particle can be stated as [74]:

$$E_{\text{diss}} = \frac{1}{2} \zeta \dot{\mathbf{r}}_n^2 \quad (3.10)$$

where  $\zeta$  is the friction constant. To derive the equation of motion for a particle in the network, the extended Euler-Lagrange's equation is used which is written here as:

$$\frac{d}{dt} \left( \frac{\partial L}{\partial \dot{\mathbf{r}}_n} \right) - \frac{\partial L}{\partial \mathbf{r}_n} + \frac{\partial E_{diss}}{\partial \dot{\mathbf{r}}_n} = \tilde{Q}_n \quad (3.11)$$

where  $L$  is the Lagrangian defined as  $L = T(\mathbf{r}_n) - U(\mathbf{r}_n)$ , and  $\tilde{Q}_n$  is the generalized force associated with the motion of the  $n$ -th particle. By substituting the Lagrangian and dissipative energy into Eq. (3.11), the equation of motion for a particle can be derived as follow:

$$m_p \ddot{\mathbf{r}}_n + \zeta \dot{\mathbf{r}}_n + \frac{\partial U(\mathbf{r}_n)}{\partial \mathbf{r}_n} = \tilde{Q}_n \quad (3.12)$$

Eq. (3.12) is known as the Langevin equation and is used in dynamic modeling of molecular systems. In polymeric systems, usually an overdamped form of the Langevin equation known as Brownian equation of motion is used which corresponds to the approximation where no average acceleration takes place [74]. Therefore, the inertia term is not considered and the equation of motion for a particle is simplified as:

$$\zeta \dot{\mathbf{r}}_n + \frac{\partial U(\mathbf{r}_n)}{\partial \mathbf{r}_n} = F_n^{(Br)} + F_n^{(Ext)} \quad (3.13)$$

where  $F_n^{(Br)}$  is the Brownian force and  $F_n^{(Ext)}$  is the external load applied on the particle due to dynamic mechanical loading. The derivative of the elastic energy function can be easily obtained as:

$$\begin{aligned} \frac{\partial U_{elast}(\mathbf{r}_n)}{\partial \mathbf{r}_n} = & K_x \sum_{n'_x} C_{nn'} (r_{n_x} - r_{n'_x}) + K_y \sum_{n'_y} C_{nn'} (r_{n_y} - r_{n'_y}) \\ & + K_z \sum_{n'_z} C_{nn'} (r_{n_z} - r_{n'_z}) \end{aligned} \quad (3.14)$$

Due to high nonlinear nature of the magnetic energy function, Taylor series has been used to expand the function in the polynomial form up to the second order. To this end, the position vectors of the  $n$ -th particle and its adjacent  $n'$ -th particle can be defined around their average values as:

$$\begin{aligned} \mathbf{r}_n &= \mathbf{r}_n^{(0)} + \delta \mathbf{r}_n \\ \mathbf{r}_{n'} &= \mathbf{r}_{n'}^{(0)} + \delta \mathbf{r}_{n'} \end{aligned} \quad (3.15)$$

where  $\mathbf{r}_n^{(0)}$  is the average value and  $\delta \mathbf{r}_n$  is the variation around the average value. Indeed,  $\delta \mathbf{r}_n$  states the fluctuation of a particle around its average position. The magnetic energy which is a function of the term  $(\mathbf{r}_n - \mathbf{r}_{n'})$ , can now be expanded using a Taylor series as:

$$U_{magn}(\mathbf{r}_n - \mathbf{r}_{n'}) = U_{magn}(\mathbf{r}_n^{(0)} - \mathbf{r}_{n'}^{(0)} + \delta \mathbf{r}_n - \delta \mathbf{r}_{n'}) \quad (3.16)$$

$$\cong U_{\text{magn}}(\mathbf{r}_n^{(0)} - \mathbf{r}_{n'}^{(0)}) + \nabla U_{\text{magn}}(\mathbf{r}_n^{(0)} - \mathbf{r}_{n'}^{(0)})^T (\delta \mathbf{r}_n - \delta \mathbf{r}_{n'}) \\ + \frac{1}{2} (\delta \mathbf{r}_n - \delta \mathbf{r}_{n'})^T H_{\text{magn}}(\mathbf{r}_n^{(0)} - \mathbf{r}_{n'}^{(0)}) (\delta \mathbf{r}_n - \delta \mathbf{r}_{n'})$$

where  $\nabla U_{\text{magn}}(\mathbf{r}_n^{(0)} - \mathbf{r}_{n'}^{(0)})$  and  $H_{\text{magn}}(\mathbf{r}_n^{(0)} - \mathbf{r}_{n'}^{(0)})$  are the gradient vector and Hessian matrix of the magnetic energy function at average positions of the particles. The superscript “ $T$ ” shows the transpose for a matrix. Regarding the above Taylor’s expansion, the first-order derivation of the magnetic energy function may be obtained as:

$$\frac{\partial U_{\text{magn}}(\mathbf{r}_n - \mathbf{r}_{n'})}{\partial \mathbf{r}_n} = \nabla U_{\text{magn}}(\mathbf{r}_n^{(0)} - \mathbf{r}_{n'}^{(0)}) + H_{\text{magn}}(\mathbf{r}_n^{(0)} - \mathbf{r}_{n'}^{(0)}) (\delta \mathbf{r}_n - \delta \mathbf{r}_{n'}) \quad (3.17)$$

The gradient of the magnetic potential energy at equilibrium state, i.e. at average positions of the particles is zero, ( $\nabla U_{\text{magn}}(\mathbf{r}_n^{(0)} - \mathbf{r}_{n'}^{(0)}) = 0$ ) and the Hessian matrix at equilibrium state in Eq. (3.17) is calculated as follow:

$$H_{\text{magn}}(\mathbf{r}_n^{(0)} - \mathbf{r}_{n'}^{(0)}) = \begin{bmatrix} \frac{\partial^2 U_{\text{magn}}}{\partial r_{n_x}^2} & \frac{\partial^2 U_{\text{magn}}}{\partial r_{n_x} \partial r_{n_y}} & \frac{\partial^2 U_{\text{magn}}}{\partial r_{n_x} \partial r_{n_z}} \\ \frac{\partial^2 U_{\text{magn}}}{\partial r_{n_y} \partial r_{n_x}} & \frac{\partial^2 U_{\text{magn}}}{\partial r_{n_y}^2} & \frac{\partial^2 U_{\text{magn}}}{\partial r_{n_y} \partial r_{n_z}} \\ \frac{\partial^2 U_{\text{magn}}}{\partial r_{n_z} \partial r_{n_x}} & \frac{\partial^2 U_{\text{magn}}}{\partial r_{n_z} \partial r_{n_y}} & \frac{\partial^2 U_{\text{magn}}}{\partial r_{n_z}^2} \end{bmatrix}_{\substack{r_n = r_n^{(0)} \\ r_{n'} = r_{n'}^{(0)}}} = -12K_0 \beta^{\frac{5}{3}} \left(\frac{J}{J^*}\right)^2 \sum_{\mathbf{k}} \hat{a}(\mathbf{k}, \beta) \quad (3.18)$$

where the index  $\mathbf{k} = \mathbf{n}' - \mathbf{n}$  is introduced and the relation  $\mathbf{r}_{n'}^{(0)} - \mathbf{r}_n^{(0)} = a_x^0 k_x \mathbf{e}_x + a_y^0 k_y \mathbf{e}_y + a_z^0 k_z \mathbf{e}_z$  was employed in derivation.  $J^*$  is a parameter defined by:

$$J^* = \sqrt{\frac{\pi \mu_0 G_0}{\phi^2}} \quad (3.19)$$

The components of the matrix  $\hat{a}(\mathbf{k}, \beta)$  in Eq. (3.18) are obtained as:

$$a_{xx}(\mathbf{k}, \beta) = -\frac{4\beta^4 k_y^4 + 4k_x^4 - k_z^4 + 3(k_x^2 + \beta^2 k_y^2)k_z^2 - 27\beta^2 k_x^2 k_y^2}{16(k_x^2 + \beta^2 k_y^2 + k_z^2)^{9/2}} \\ a_{xy}(\mathbf{k}, \beta) = a_{yx}(\mathbf{k}, \beta) = \frac{5\beta^2 k_x k_y (4\beta^2 k_y^2 - 3k_x^2 - 3k_z^2)}{16(k_x^2 + \beta^2 k_y^2 + k_z^2)^{9/2}} \quad (3.20) \\ a_{yy}(\mathbf{k}, \beta) = \frac{8\beta^4 k_y^4 - 24\beta^2 k_y^2 (k_x^2 + k_z^2) + 3(k_x^2 + k_z^2)^2}{16(k_x^2 + \beta^2 k_y^2 + k_z^2)^{9/2}}$$



$$\begin{aligned}
a_{zy}(\mathbf{k}, \beta) &= a_{yz}(\mathbf{k}, \beta) = \frac{5\beta^2 k_y k_z (4\beta^2 k_y^2 - 3k_x^2 - 3k_z^2)}{16(k_x^2 + \beta^2 k_y^2 + k_z^2)^{9/2}} \\
a_{zx}(\mathbf{k}, \beta) &= a_{xz}(\mathbf{k}, \beta) = \frac{5k_x k_z (6\beta^2 k_y^2 - k_x^2 - 3k_z^2)}{16(k_x^2 + \beta^2 k_y^2 + k_z^2)^{9/2}} \\
a_{zz}(\mathbf{k}, \beta) &= -\frac{4\beta^4 k_y^4 + 4k_z^4 - k_x^4 + 3(\beta^2 k_y^2 + k_z^2)k_x^2 - 27\beta^2 k_y^2 k_z^2}{16(k_x^2 + \beta^2 k_y^2 + k_z^2)^{9/2}}
\end{aligned}$$

Finally, by substituting Eqs. (3.14), (3.17), and (3.18) into Eq. (3.13), the equation of motion can be written in terms of  $\delta \mathbf{r}_n$  in the following form:

$$\begin{aligned}
\zeta \delta \dot{\mathbf{r}}_n + K_x \sum_{n'_x} C_{nn'} (\delta r_{n_x} - \delta r_{n'_x}) + K_y \sum_{n'_y} C_{nn'} (\delta r_{n_y} - \delta r_{n'_y}) \\
+ K_z \sum_{n'_z} C_{nn'} (\delta r_{n_z} - \delta r_{n'_z}) \\
- 12K_0 \beta^{\frac{5}{3}} \left( \frac{J}{J^*} \right)^2 \sum_{\mathbf{k}} \hat{a}(\mathbf{k}, \beta) (\delta \mathbf{r}_n - \delta \mathbf{r}_{n+\mathbf{k}}) = F_n^{(\text{Br})} + F_n^{(\text{Ext})}
\end{aligned} \tag{3.21}$$

To solve the equation of motion and find the relaxation times of the particle motions, first the Cartesian coordinates  $\delta \mathbf{r}_n$  are transformed into the normal coordinates  $\mathbf{Q}(\boldsymbol{\theta})$  using the following Fourier transform [74]:

$$\delta \mathbf{r}_n = \sum_{\boldsymbol{\theta}} e^{in\boldsymbol{\theta}} \mathbf{Q}(\boldsymbol{\theta}) \tag{3.22}$$

The phase shift vector  $\boldsymbol{\theta} = (\theta_x, \theta_y, \theta_z)$ , with the components vary within the limiting values of 0 and  $\pi$ , i.e.  $\theta_{x,y,z} \in [0, \pi]$ , determines the phase shift between the displacements of neighboring network junctions for motions along the x, y, z-axes under excitation of a given normal mode. The limiting values of  $\boldsymbol{\theta} \rightarrow (0, 0, 0)$  describe the in-phase motion of neighboring particles whereas  $\boldsymbol{\theta} \rightarrow (\pi, \pi, \pi)$  determine modes with out-of-phase motion of particles. In Eq. (3.22),  $n\boldsymbol{\theta}$  is the scalar product of the vectors.

By substituting Eq. (3.22) into Eq. (3.21), the first term in the left side of the equation ( $\zeta \delta \dot{\mathbf{r}}_n$ ), takes the following form in the normal coordinates:

$$\zeta \delta \dot{\mathbf{r}}_n = \zeta \sum_{\boldsymbol{\theta}} e^{in\boldsymbol{\theta}} \dot{\mathbf{Q}}(\boldsymbol{\theta}) \tag{3.23}$$

where  $\dot{\mathbf{Q}}(\boldsymbol{\theta})$  is the time derivative of the normal coordinate  $\mathbf{Q}(\boldsymbol{\theta})$ . Also considering that there are six particles in the cubic network surrounding the  $n$ -th particle, the terms having spring forces in Eq. (3.21) can be simplified as:

$$\begin{aligned}
& K_x \sum_{n'_x} C_{nn'} (\delta r_{n_x} - \delta r_{n'_x}) + K_y \sum_{n'_y} C_{nn'} (\delta r_{n_y} - \delta r_{n'_y}) \\
& \quad + K_z \sum_{n'_z} C_{nn'} (\delta r_{n_z} - \delta r_{n'_z}) \\
& = K_x \left( 2\delta r_{(n_x, n_y, n_z)} - \delta r_{(n_x+1, n_y, n_z)} - \delta r_{(n_x-1, n_y, n_z)} \right) \\
& \quad + K_y \left( 2\delta r_{(n_x, n_y, n_z)} - \delta r_{(n_x, n_y+1, n_z)} - \delta r_{(n_x, n_y-1, n_z)} \right) \\
& \quad + K_z \left( 2\delta r_{(n_x, n_y, n_z)} - \delta r_{(n_x, n_y, n_z+1)} - \delta r_{(n_x, n_y, n_z-1)} \right)
\end{aligned} \tag{3.24}$$

which after substitution of normal modes from Eq. (3.22), right hand side of Eq. (3.24) yields:

$$\begin{aligned}
& = K_x \left( 2 \sum_{\boldsymbol{\theta}} e^{in\boldsymbol{\theta}} \mathbf{Q}(\boldsymbol{\theta}) - \sum_{\boldsymbol{\theta}} e^{in\boldsymbol{\theta}+i\theta_x} \mathbf{Q}(\boldsymbol{\theta}) - \sum_{\boldsymbol{\theta}} e^{in\boldsymbol{\theta}-i\theta_x} \mathbf{Q}(\boldsymbol{\theta}) \right) \\
& \quad + K_y \left( 2 \sum_{\boldsymbol{\theta}} e^{in\boldsymbol{\theta}} \mathbf{Q}(\boldsymbol{\theta}) - \sum_{\boldsymbol{\theta}} e^{in\boldsymbol{\theta}+i\theta_y} \mathbf{Q}(\boldsymbol{\theta}) - \sum_{\boldsymbol{\theta}} e^{in\boldsymbol{\theta}-i\theta_y} \mathbf{Q}(\boldsymbol{\theta}) \right) \\
& \quad + K_z \left( 2 \sum_{\boldsymbol{\theta}} e^{in\boldsymbol{\theta}} \mathbf{Q}(\boldsymbol{\theta}) - \sum_{\boldsymbol{\theta}} e^{in\boldsymbol{\theta}+i\theta_z} \mathbf{Q}(\boldsymbol{\theta}) - \sum_{\boldsymbol{\theta}} e^{in\boldsymbol{\theta}-i\theta_z} \mathbf{Q}(\boldsymbol{\theta}) \right)
\end{aligned} \tag{3.25}$$

Also as for the general anisotropic network, the horizontal distance between particles in the  $x$ - $z$  plane and so the spring constants are equal,  $K_x = K_z$ . We may write Eq. (3.25) as:

$$\begin{aligned}
& = K_x \left( 4 \sum_{\boldsymbol{\theta}} e^{in\boldsymbol{\theta}} - \sum_{\boldsymbol{\theta}} e^{in\boldsymbol{\theta}} (e^{i\theta_x} + e^{-i\theta_x} + e^{i\theta_z} + e^{-i\theta_z}) \right) \mathbf{Q}(\boldsymbol{\theta}) \\
& \quad + K_y \left( 2 \sum_{\boldsymbol{\theta}} e^{in\boldsymbol{\theta}} - \sum_{\boldsymbol{\theta}} e^{in\boldsymbol{\theta}} (e^{i\theta_y} + e^{-i\theta_y}) \right) \mathbf{Q}(\boldsymbol{\theta})
\end{aligned} \tag{3.26}$$

Finally, using the Euler's formula,  $e^{i\theta_x} = \cos(\theta_x) + i\sin(\theta_x)$ , Eq. (3.26) can be written as:

$$\begin{aligned}
&= \left[ K_x \left( 4 \sum_{\theta} e^{in\theta} - \sum_{\theta} e^{in\theta} (2 \cos(\theta_x) + 2 \cos(\theta_z)) \right) \right. \\
&\quad \left. + K_y \left( 2 \sum_{\theta} e^{in\theta} - \sum_{\theta} e^{in\theta} (2 \cos(\theta_y)) \right) \right] \mathbf{Q}(\theta) \\
&= \left[ 2K_x \sum_{\theta} e^{in\theta} (2 - \cos(\theta_x) - \cos(\theta_z)) + 2K_y \sum_{\theta} e^{in\theta} (1 - \cos(\theta_y)) \right] \mathbf{Q}(\theta)
\end{aligned} \tag{3.27}$$

The term associated with magnetic forces in Eq. (3.21) also transform to the following form after substitution of normal modes:

$$\begin{aligned}
&-12K_0\beta^{\frac{5}{3}} \left( \frac{J}{J^*} \right)^2 \sum_{\mathbf{k}} \hat{\mathbf{a}}(\mathbf{k}, \beta) (\delta \mathbf{r}_n - \delta \mathbf{r}_{n+\mathbf{k}}) \\
&= -12K_0\beta^{\frac{5}{3}} \left( \frac{J}{J^*} \right)^2 \sum_{\mathbf{k}} \hat{\mathbf{a}}(\mathbf{k}, \beta) \left( \sum_{\theta} e^{in\theta} \mathbf{Q}(\theta) - \sum_{\theta} e^{i(n+\mathbf{k})\theta} \mathbf{Q}(\theta) \right) \\
&= -12K_0\beta^{\frac{5}{3}} \left( \frac{J}{J^*} \right)^2 \sum_{\mathbf{k}} \hat{\mathbf{a}}(\mathbf{k}) \left( \sum_{\theta} e^{in\theta} \mathbf{Q}(\theta) - \sum_{\theta} e^{in\theta} e^{i\mathbf{k}\theta} \mathbf{Q}(\theta) \right) = \\
&= -12K_0\beta^{\frac{5}{3}} \left( \frac{J}{J^*} \right)^2 \sum_{\mathbf{k}} \hat{\mathbf{a}}(\mathbf{k}) \left( \sum_{\theta} e^{in\theta} \mathbf{Q}(\theta) - \sum_{\theta} e^{in\theta} (\cos(\mathbf{k}\theta) + i \sin(\mathbf{k}\theta)) \mathbf{Q}(\theta) \right) \\
&= -12K_0\beta^{\frac{5}{3}} \left( \frac{J}{J^*} \right)^2 \sum_{\mathbf{k}} \hat{\mathbf{a}}(\mathbf{k}) \left( \sum_{\theta} e^{in\theta} (1 - \cos(\mathbf{k}\theta) - i \sin(\mathbf{k}\theta)) \right) \mathbf{Q}(\theta) \\
&= -12K_0\beta^{\frac{5}{3}} \left( \frac{J}{J^*} \right)^2 \sum_{\theta} e^{in\theta} \sum_{\mathbf{k}} \hat{\mathbf{a}}(\mathbf{k}, \beta) (1 - \cos(\mathbf{k}\theta) - i \sin(\mathbf{k}\theta)) \mathbf{Q}(\theta)
\end{aligned} \tag{3.28}$$

By substituting the resulting relations from Eqs. (3.23), (3.27), and (3.28) into the Eq. (3.21), the homogeneous equation of motion can be expressed as:

$$\begin{aligned}
\zeta \sum_{\theta} e^{in\theta} \dot{\mathbf{Q}}(\theta) + \left[ 2K_x \sum_{\theta} e^{in\theta} (2 - \cos(\theta_x) - \cos(\theta_z)) + 2K_y \sum_{\theta} e^{in\theta} (1 - \cos(\theta_y)) \right] \mathbf{Q}(\theta) \\
- 12K_0\beta^{\frac{5}{3}} \left( \frac{J}{J^*} \right)^2 \sum_{\theta} e^{in\theta} \sum_{\mathbf{k}} \hat{\mathbf{a}}(\mathbf{k}, \beta) (1 - \cos(\mathbf{k}\theta) - i \sin(\mathbf{k}\theta)) \mathbf{Q}(\theta) = 0
\end{aligned} \tag{3.29}$$

Eq. (3.29) can be also written in the following form:

$$= \sum_{\theta} e^{i\mathbf{n}\theta} \left( \zeta \dot{\mathbf{Q}}(\theta) + \left( \begin{array}{c} 2K_x(2 - \cos(\theta_x) - \cos(\theta_z)) + 2K_y(1 - \cos(\theta_y)) \\ -12K_0\beta^{\frac{5}{3}} \left(\frac{J}{J^*}\right)^2 \sum_{\mathbf{k}} \hat{\mathbf{a}}(\mathbf{k}, \beta) (1 - \cos(\mathbf{k}\theta) - i\sin(\mathbf{k}\theta)) \end{array} \right) \mathbf{Q}(\theta) \right) = 0 \quad (3.30)$$

To be valid, the summand in Eq. (3.30) must be zero:

$$\zeta \dot{\mathbf{Q}}(\theta) + \left( \begin{array}{c} 2K_x(2 - \cos(\theta_x) - \cos(\theta_z)) + 2K_y(1 - \cos(\theta_y)) \\ -12K_0\beta^{\frac{5}{3}} \left(\frac{J}{J^*}\right)^2 \sum_{\mathbf{k}} \hat{\mathbf{a}}(\mathbf{k}, \beta) (1 - \cos(\mathbf{k}\theta) - i\sin(\mathbf{k}\theta)) \end{array} \right) \mathbf{Q}(\theta) = 0 \quad (3.31)$$

Using relations in Eq. (3.4) and by taking only the real terms into consideration, Eq. (3.31) can be subsequently simplified as:

$$\dot{\mathbf{Q}}(\theta) + \frac{12K_0}{\zeta} \left( \begin{array}{c} \frac{1}{6}\beta^{\frac{2}{3}}(2 - \cos(\theta_x) - \cos(\theta_z)) + \frac{1}{6}\beta^{-\frac{4}{3}}(1 - \cos(\theta_y)) \\ +\beta^{\frac{5}{3}} \left(\frac{J}{J^*}\right)^2 \sum_{\mathbf{k}} \hat{\mathbf{a}}(\mathbf{k}, \beta) (\cos(\mathbf{k}\theta) - 1) \end{array} \right) \mathbf{Q}(\theta) = 0 \quad (3.32)$$

which can be written in compact form as:

$$\dot{\mathbf{Q}}(\theta) + \frac{1}{\tau_0} \hat{\mathbf{B}} \mathbf{Q}(\theta) = 0 \quad (3.33)$$

where  $\tau_0 = \frac{\zeta}{12K_0}$  is the minimal relaxation time associated with the base isotropic particle network in the absence of the applied magnetic field. Matrix  $\hat{\mathbf{B}}$  has the following form:

$$\hat{\mathbf{B}}(\theta, \beta) = \lambda_0(\theta, \beta) \hat{\mathbf{I}} + \left(\frac{J}{J^*}\right)^2 \hat{\mathbf{A}}(\theta, \beta) \quad (3.34)$$

where  $\hat{\mathbf{I}}$  is a third-order unit matrix. The function  $\lambda_0(\theta, \beta)$  and the matrix  $\hat{\mathbf{A}}(\theta, \beta)$  are expressed as:

$$\lambda_0(\theta, \beta) = \frac{1}{6}\beta^{\frac{2}{3}}(2 - \cos(\theta_x) - \cos(\theta_z)) + \frac{1}{6}\beta^{-\frac{4}{3}}(1 - \cos(\theta_y)) \quad (3.35)$$

$$\hat{\mathbf{A}}(\theta, \beta) = \beta^{\frac{5}{3}} \sum_{\mathbf{k}} \hat{\mathbf{a}}(\mathbf{k}, \beta) (\cos(\mathbf{k}\theta) - 1) \quad (3.36)$$

It is seen that the cubic matrix  $\hat{\mathbf{A}}(\theta, \beta)$  is related to the symmetrical matrix  $\hat{\mathbf{a}}(\mathbf{k}, \beta)$  whose components were obtained in Eq. (3.20). Now Equation (3.33) is solved to obtain the relaxation spectrum corresponding to the normal modes. A potential solution for Eq. (3.33) is in the following form:

$$\mathbf{Q} = \mathbf{V} e^{-\frac{t}{\tau}} \quad (3.37)$$

where  $\hat{\tau}$  is the relaxation time for a given normal coordinate. To simplify the solution of the Eq. (3.33), the dimensionless parameter  $\lambda = \tau_0 / \hat{\tau}$  is defined where  $\lambda$  is the inverse relaxation time. By substituting Eq. (3.37) into Eq. (3.33), the eigenvalue equation for  $\lambda$  is obtained in the following form:

$$\hat{B}\mathbf{V} = \lambda\mathbf{V} \quad (3.38)$$

where the vector  $\mathbf{V}$  and the inverse relaxation time  $\lambda$  are the eigenvector and eigenvalues of the matrix  $\hat{B}$ , respectively. To find the relaxation time and spectrum of the particle network, the eigenvalue equation in Eq. (3.38) has to be solved to find the values of  $\lambda$  in the three directions, i.e.  $\lambda_x, \lambda_y, \lambda_z$ . An approximate solution is suggested in [65] for the eigenvalues of the matrix  $\hat{B}$  assuming that the contribution of the non-diagonal elements of the matrix  $\hat{A}$  to the dynamic characteristics of the network can be neglected with a good approximation. It means that the motion along one direction is independent from the motions along the other directions. The approximate solution for  $\lambda$  can be expressed as:

$$\begin{cases} \lambda_x(\boldsymbol{\theta}, \beta) = \lambda_0(\boldsymbol{\theta}, \beta) + \left(\frac{J}{J^*}\right)^2 A_{xx}(\boldsymbol{\theta}, \beta) \\ \lambda_y(\boldsymbol{\theta}, \beta) = \lambda_0(\boldsymbol{\theta}, \beta) + \left(\frac{J}{J^*}\right)^2 A_{yy}(\boldsymbol{\theta}, \beta) \\ \lambda_z(\boldsymbol{\theta}, \beta) = \lambda_0(\boldsymbol{\theta}, \beta) + \left(\frac{J}{J^*}\right)^2 A_{zz}(\boldsymbol{\theta}, \beta) \end{cases} \quad (3.39)$$

where  $A_{xx}, A_{yy}, A_{zz}$  are the diagonal elements of the matrix  $\hat{A}(\boldsymbol{\theta}, \beta)$  defined in Eq. (3.36). Therefore, Eq. (3.39) gives three independent relations for the eigenvalues in the three directions  $\lambda_x, \lambda_y, \lambda_z$ . It is seen that the eigenvalues  $\lambda_x, \lambda_y, \lambda_z$  are functions of  $\theta_x, \theta_y, \theta_z$  and depend on the parameter  $\left(\frac{J}{J^*}\right)$ . In addition,  $\lambda_x$  and  $\lambda_z$  are equal at  $\theta_x = \theta_y = \theta_z$ . These eigenvalues define the relaxation times associated with particle motions parallel to the magnetic field  $\hat{\tau}_y = \tau_0/\lambda_y$  and perpendicular to the field direction,  $\hat{\tau}_x = \tau_0/\lambda_x$  and  $\hat{\tau}_z = \tau_0/\lambda_z$ . It can be inferred from Eq. (3.39) that  $\lambda_0$  describes the eigenvalue  $\lambda$  for the particle network in the absence of magnetic field. It should be noted here that dependence of parameters in the above equations on  $\boldsymbol{\theta}$  and  $\beta$  is for the general anisotropic network of particles. For the isotropic configuration, equal distance between particles results in  $\beta = 1$  and so the parameters only depend on the phase shift vector  $\boldsymbol{\theta}$ .

The particle polarization  $J$ , which cannot be directly measured, is related to the magnetic flux density, which is a directly measurable parameter, using a modified particle saturation model

originated from the work of Jolly et al. [51] and discussed in the previous chapter in Eq.(2.19). Based on this model, particle polarization,  $J$ , for an MRE with volume fraction of  $\phi$  can be expressed as a function of the averaged magnetic flux density,  $B$ , as:

$$J = \frac{\frac{3}{2}(\alpha - \alpha^3)B + (1 - \alpha^3)(sJ_s)}{1 + \frac{3}{2}\phi(\alpha - \alpha^3)} \quad (3.40)$$

where  $J_s$  is the saturation polarization, and  $\alpha$  is a parameter constrained within the range of 0 and 1 as defined in Eq.(2.20). The constant parameter  $k_1$  is assumed to be unity here,  $k_1 = 1$ . As also described in the Chapter 2, the value of saturation polarization,  $J_s$ , for pure iron is 2.1 T. However, MRE samples with various volume fraction of particles will saturate at different level of magnetic induction as observed in the experimental results in Section 2.2. Therefore, another constant parameter,  $s$ , is used in the model as the coefficient of the saturation polarization to tune for MRE samples with different volume fraction of iron particles.

Using Eqs. (3.39) and (3.40), the eigenvalues,  $\lambda$ , can now be obtained as a function of  $\theta$  for different values of magnetic flux density,  $B$ , volume fraction,  $\phi$ , and anisotropy parameter,  $\beta$ . First, we consider isotropic MREs with  $\beta = 1$ . Figure 3.2 shows the spectrum of eigenvalues,  $\lambda$ , as a function of  $\theta = \theta_x = \theta_y = \theta_z$  for two MRE samples with 15% and 25% volume fraction of magnetic particles under 0.0 T and 0.2 T applied magnetic flux densities.

The dashed line in Figure 3.2, presents the eigenvalue  $\lambda_0$  in the absence of magnetic field. It is observed that by applying a magnetic field on the medium, the spectrum of eigenvalues breaks into two independent branches of eigenvalues associated with motions along ( $\lambda_y < \lambda_0$ ) and normal ( $\lambda_x = \lambda_z > \lambda_0$ ) to the direction of external magnetic field. Both the external magnetic field and volume fraction of particles intensify the breaking level of eigenvalues. For instance, for the sample with  $\phi = 15\%$ ,  $\lambda_y$  decreases while  $\lambda_x = \lambda_z$  increases with increasing the magnetic flux density as shown in Figure 3.2 (a) and (b). Similar behavior is observed in Figure 3.2 (c) and (d) for the volume fraction of  $\phi = 25\%$ . On the other hand, at constant level of applied magnetic field, the sample with higher volume fraction of particles has lower values of  $\lambda_y$  and higher values of  $\lambda_x = \lambda_z$ , which shows the fact that sensitivity to the applied magnetic field is greater when there is higher population of particles in the structure.

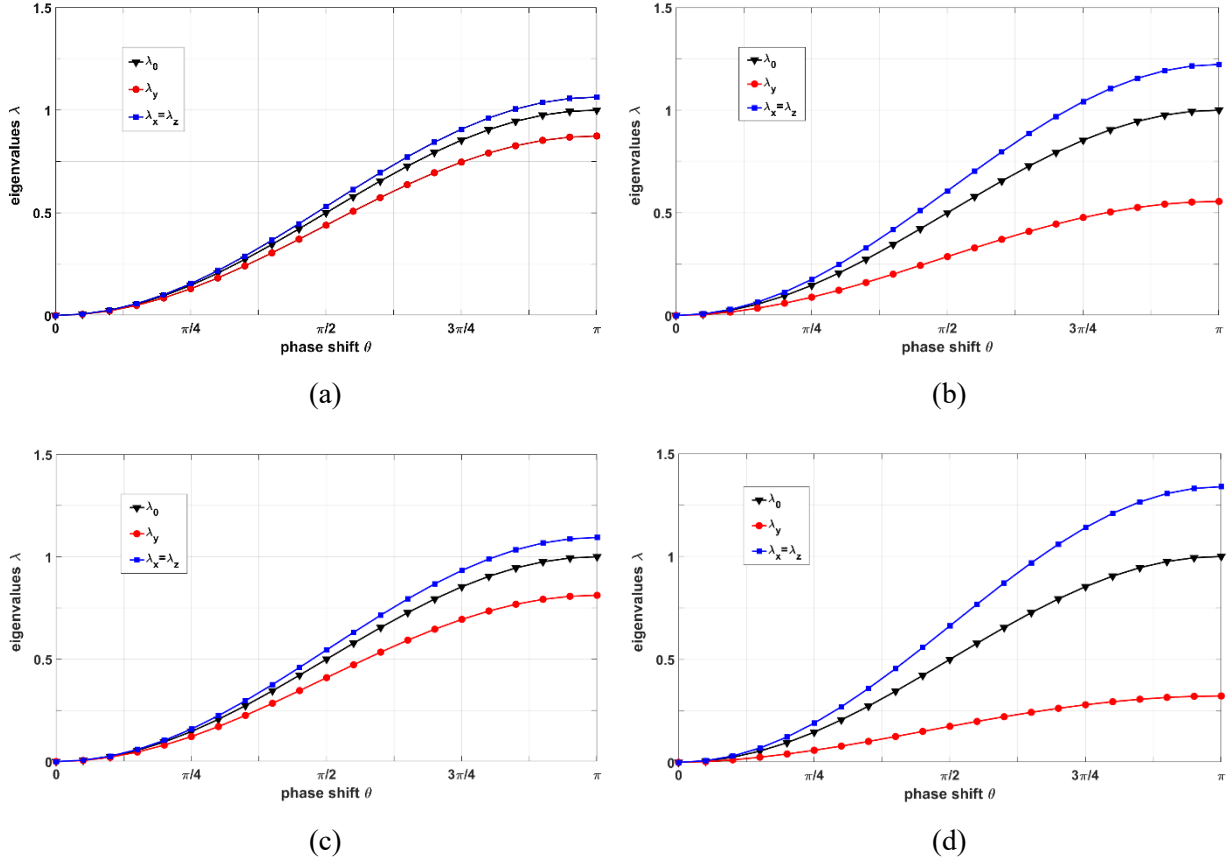


Figure 3.2 Spectrum of eigenvalues,  $\lambda$ , in terms of  $\theta$  for isotropic dispersion of particles at various magnetic field induction: (a)  $\phi = 15\%$ ,  $G_0 = 31.77$  kPa, and  $B = 0.2$  T, (b)  $\phi = 15\%$ ,  $G_0 = 31.77$  kPa, and  $B = 0.4$  T, (c)  $\phi = 25\%$ ,  $G_0 = 48.19$  kPa, and  $B = 0.2$  T, and (d)  $\phi = 25\%$ ,  $G_0 = 48.19$  kPa, and  $B = 0.4$  T.

For the chain-like anisotropic dispersion of particles, the eigenvalues,  $\lambda$ , also depend on the anisotropy parameter  $\beta < 1$ . Figure 3.3 shows the eigenvalues for an anisotropic MRE with  $\phi = 15\%$  at two different values of anisotropy parameter  $\beta = 0.8$  and  $\beta = 0.6$ . To observe the effect of  $\beta$  on the spectrum, magnetic flux density is kept constant at  $B = 0.2$  T. Results show that the zero-field eigenvalue,  $\lambda_0$ , increases with decreasing  $\beta$  suggesting that higher eigenvalue (lower relaxation time) can be achieved in the absence of magnetic field by enhancing the anisotropy nature of the MRE. In addition, under applied magnetic field, greater decrease in  $\lambda_y$  and greater increase in  $\lambda_x = \lambda_z$  are observed with decreasing  $\beta$ . This suggests that the eigenvalues (relaxation times) become more sensitive to the magnetic field as the particles arrangement moves toward chains (decrease in  $\beta$  from unity).

It should be noted that the relaxation time is inversely related to the effective stiffness along a direction which can explain the variation of eigenvalues with respect to the applied magnetic field.

As discussed in the Chapter 2 and [18], when magnetic field is applied on the particle network along the y direction, particles along the y-axis attract each other leading to negative magnetic potential energy that reduces the effective stiffness and subsequently increases the relaxation time along the y-axis (decrease of  $\lambda_y$ ). On the other hand, the positive magnetic potential energy of particles in the x and z directions, adds to the stiffness in those direction which leads to the decrease of relaxation time (increase of  $\lambda_x = \lambda_z$ ). This trend of eigenvalues in terms of applied magnetic field is naturally more pronounced at higher volume fraction of particles and also for strongly chain-like structure of particles as shown in the Figure 3.2 and Figure 3.3. Another important conclusion from results of this part is that the relaxation time of the particle motions at zero magnetic field depends on the particle distribution ( $\beta$ ) but not on the population of the particles ( $\phi$ ).

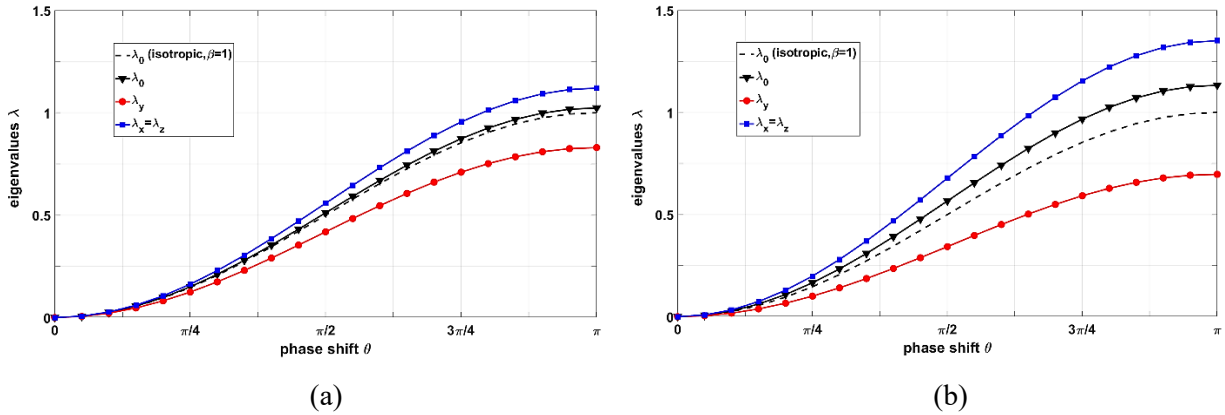


Figure 3.3 Spectrum of eigenvalues,  $\lambda$ , in terms of  $\theta$  for anisotropic chain-like distribution of particles with  $\phi = 15\%$ ,  $G_0 = 31.77$  kPa, and  $B = 0.2$  T, for (a)  $\beta = 0.8$  and (b)  $\beta = 0.6$ .

According to Eq. (3.39) and results of Figure 3.2 and Figure 3.3, the decreasing trend of  $\lambda_y$  with increase of external magnetic field might ultimately yield negative  $\lambda_y$  and subsequently negative relaxation time along the y-axis,  $\hat{\tau}_y$ , at sufficiently high magnetic flux density. Negative relaxation time means instability and tendency of a normal mode to move toward infinity which means that under applied magnetic field, particles diverge from the initial equilibrium position and they may rearrange into a new equilibrium state [66]. Regarding that the rearrangement of particles is out of the scope of the current model, we introduce a critical magnetic flux density,  $B_{cr}$ , at which  $\lambda_y$  is a negative value and thus the model is not applicable to magnetic flux densities above this critical threshold. The critical flux density depends on both the anisotropy parameter,  $\beta$ , and volume fraction of magnetic particles,  $\phi$ . Therefore, all eigenvalues are positive at  $B < B_{cr}$ , while



there are negative eigenvalues in the spectrum at  $B > B_{cr}$  which is not acceptable. The critical flux density is calculated numerically as a function of  $\beta$  varying in the range of 0.1 to 3 (it is noted that in the present research we are mainly concerned with  $\beta \leq 1$ ) and  $\phi$  changing from 5% to 40% as shown in the Figure 3.4. Results suggest that at constant  $\phi$ , the critical flux density occurs at lower field values for chain-like configuration of particles ( $\beta < 1$ ) as compared with the isotropic particle network ( $\beta = 1$ ). For instance, for MREs with 15% particle volume fraction, the critical flux density for isotropic network ( $\beta = 1$ ) is  $B_{cr} = 0.64$  T, while it is  $B_{cr} = 0.5$  T for  $\beta = 0.8$ . Besides, for a constant value of  $\beta$ , the critical flux density moves toward lower flux densities at higher volume fraction of particles. For instance, for  $\beta = 0.6$ , the critical flux density is  $B_{cr} = 0.86$  T for  $\phi = 5\%$ , , while it is  $B_{cr} = 0.29$  T for  $\phi = 20\%$ . It should be noted that the relation between  $G_0$  and  $\phi$  is obtained as  $G_0 = 15810 e^{4.462\phi}$  using the experimental results presented in Figure 2.23 of CHAPTER 2 and this relation is used for the simulations presented in Figure 3.4. In summary, the flux density values in the proposed model cannot go beyond the critical flux density,  $B_{cr}$ .

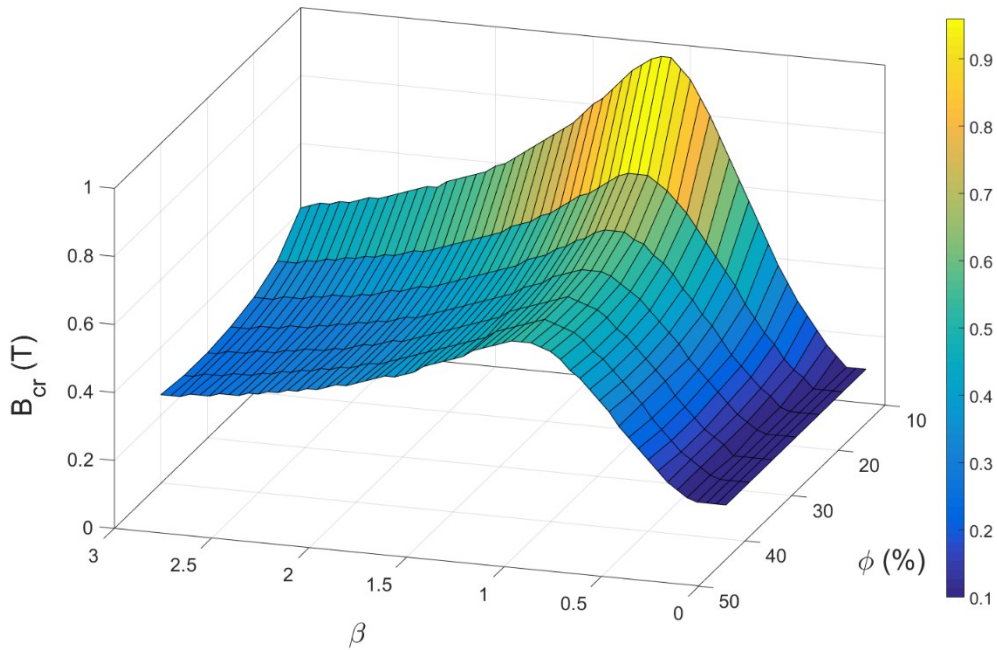


Figure 3.4 Critical flux density,  $B_{cr}$ , in tesla versus anisotropy parameter,  $\beta$ , and volume fraction of magnetic particles,  $\phi$  (%), ( $s = 1$ ).

### 3.2.3 Storage and Loss Moduli of MRE

The results of relaxation time spectrum obtained in the previous section can be effectively utilized to evaluate the dynamic moduli of the MRE material. Let us consider that the MRE material is under oscillatory shear deformation where magnetic field is applied normal to the shearing deformation as shown in Figure 3.5.

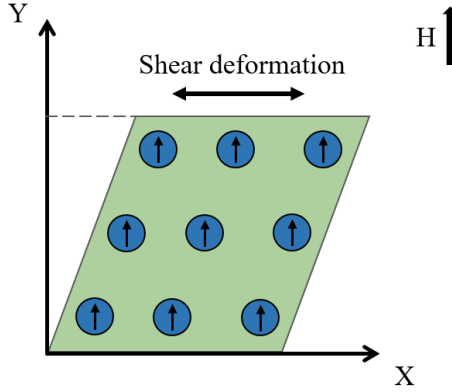


Figure 3.5 An element of MRE material under oscillating shear deformation where magnetic field is normal to the shear direction.

Using the relations developed for the dynamic properties of three-dimensional network polymer systems [94], the time-dependent relaxation modulus of the MRE material in the framework of considered normal coordinates can be written as [66]:

$$G_{xy}(t) = G_{xy}^{(eq)} + \frac{ck_B\bar{T}}{\pi^3} \iiint_{\Omega} \left[ \frac{\lambda_x(\boldsymbol{\theta}, \beta)}{\lambda_y(\boldsymbol{\theta}, \beta)} e^{-(\lambda_x(\boldsymbol{\theta}, \beta) + \lambda_y(\boldsymbol{\theta}, \beta))t/\tau_0} \right] d\theta_x d\theta_y d\theta_z \quad (3.41)$$

where  $G_{xy}^{(eq)}$  is the static shear modulus,  $c$  is the number of magnetic particles in the unit volume of the network which can be written as  $c = \phi/v$ .  $k_B = 1.380649 \times 10^{-23}$  is the Boltzmann constant,  $\bar{T}$  is the average absolute temperature which is 298.15 K for the experiments done in the current research. The triple integral is performed over the volume  $\Omega$  of the cube with the side length of  $\pi$ .

The frequency-dependent dynamic complex modulus can subsequently be derived by transforming the time-dependent relaxation modulus in Eq. (3.41) to frequency domain using Fourier transform as:

$$G_{xy}^*(\omega) = i\omega \int_0^{\infty} G_{xy}(t) e^{-i\omega t} dt \quad (3.42)$$

where  $\omega = 2\pi f$  is the angular frequency in rad/s. The storage and loss moduli can be obtained from the real and imaginary parts of the dynamic complex modulus, respectively. By substituting Eq. (3.41) into Eq. (3.42) and performing the time-dependent integral, the storage,  $G'_{xy}$ , and loss,  $G''_{xy}$ , moduli can be expressed in terms of frequency as:

$$G'_{xy}(f) = G_{xy}^{(\text{eq})} + \frac{cPk_B\bar{T}}{\pi^3} \iiint_{\Omega} \left[ \frac{\lambda_x(\boldsymbol{\theta}, \beta)}{\lambda_y(\boldsymbol{\theta}, \beta)} \times \frac{(2\pi f\tau_0)^2}{[\lambda_x(\boldsymbol{\theta}, \beta) + \lambda_y(\boldsymbol{\theta}, \beta)]^2 + (2\pi f\tau_0)^2} \right] d\theta_x d\theta_y d\theta_z \quad (3.43)$$

$$G''_{xy}(f) = G''_{f_0} + \frac{cPk_B\bar{T}}{\pi^3} \iiint_{\Omega} \left[ \frac{\lambda_x(\boldsymbol{\theta}, \beta)}{\lambda_y(\boldsymbol{\theta}, \beta)} \times \frac{(2\pi f\tau_0)(\lambda_x(\boldsymbol{\theta}, \beta) + \lambda_y(\boldsymbol{\theta}, \beta))}{[\lambda_x(\boldsymbol{\theta}, \beta) + \lambda_y(\boldsymbol{\theta}, \beta)]^2 + (2\pi f\tau_0)^2} \right] d\theta_x d\theta_y d\theta_z \quad (3.44)$$

where  $f$  is the frequency of the dynamic load in Hz.  $G_{xy}^{(\text{eq})}$  is the static shear modulus that can be obtained from quasi-static model in Chapter 2 or from the experimental data. Since practically the loss modulus at low starting frequency is not zero and has a small value,  $G''_{f_0}$  is added to the right side of Eq. (3.44) to address the initial loss modulus at starting frequency. Therefore, the value  $G''_{f_0}$  will be identified from the experimental results. As mentioned before,  $\tau_0$  is the minimal relaxation time of the isotropic particle network in the absence of the applied magnetic field. In Eqs. (3.43) and (3.44),  $P$  is a constant incorporated into the modulus formulations as a tuning parameter. This parameter could also compensate the effects of complex multipolar interactions resulting from complex structure of particles on the dynamics of the material which are not considered in the ideal cubic particle network of the microstructure-based model.

It is noted that storage and loss moduli in Eqs. (3.43) and (3.44) are not only dependent on the frequency, but also are functions of the applied magnetic flux density, anisotropy parameter  $\beta$ , volume fraction of particles, and material properties of the host matrix. Equations (3.43) and (3.44) can be practically used to predict the results of storage and loss moduli of the isotropic and anisotropic MRE materials with different volume fractions under varying applied magnetic field and dynamic shear loading. It is interesting to note that the proposed models for storage and loss moduli in Eqs. (3.43) and (3.44) have minimal number of constant parameters ( $\tau_0, P, s$  and  $\beta$ ) which should be identified using experiment. Such versatile models can be effectively utilized for modeling and analysis of MRE-based devices at early stages of design without conducting time-

consuming and expensive experiments for different conditions associated with material, magnetic field and loading excitation.

### **3.3 Materials and Experimental Methods**

#### **3.3.1 Preparation of MRE Samples**

A silicon rubber with commercial name of Ecoflex™ 00-20 is used as the elastomeric matrix material. This silicon rubber has a density of 1.04 g/cm<sup>3</sup> and dynamic viscosity of 3000 cPs. Spherical shape CIPs with commercial name of BASF SQ\* with average diameter of 3.9 to 5 μm and density of 7.87 g/cm<sup>3</sup> are used as the magnetic fillers. The spherical shape of the particles and low viscosity of the selected rubber facilitate the distribution of particles in the matrix and ensures easy mixing and degassing.

As mentioned earlier in CHAPTER 2, sample preparation has three steps. In the first step, required amounts of the silicone rubber and CIPs are mixed for about 4 minutes. The mixture in the next step is placed inside a vacuum chamber under 28 in-Hg for about 5 minutes to remove the trapped air bubbles during mixing. Finally, the mixture is transferred to a cylindrical plexiglass mold and left at room temperature for about 24 hours. Curing phase occurs without applying a magnetic field on the sample for isotropic dispersion of particles. For the anisotropic sample, a powerful electromagnet apparatus, shown in Figure 3.6, is used to apply magnetic flux of about 1 T on the mold for 2 hours in order to form chains of particles inside the material. After 24 hours, MRE samples are taken out of the mold and left in the cabinet for at least another 24 hours before cutting and preparation of cylindrical test specimens with diameter and thickness of 20 mm and 1 mm, respectively. Table 3.1 provides information regarding four types of MRE samples fabricated in the lab.

Table 3.1 Constituents of the MRE samples.

MRE sample ID	Particles distribution	Materials		Volume fraction of constituents (%)	
		CIP	Silicone rubber	CIP	Silicone rubber
Sample 1	Isotropic	BASF SQ <sup>®</sup>	Ecoflex <sup>TM</sup> 00-20	15	85
Sample 2	Isotropic	BASF SQ <sup>®</sup>	Ecoflex <sup>TM</sup> 00-20	25	75
Sample 3	Anisotropic	BASF SQ <sup>®</sup>	Ecoflex <sup>TM</sup> 00-20	15	85
Sample 4	Anisotropic	BASF SQ <sup>®</sup>	Ecoflex <sup>TM</sup> 00-20	25	75



Figure 3.6 Electromagnet device used for applying magnetic field on MRE fabrication mold.

### 3.3.2 Microstructure Imaging

Distribution of magnetic particles in the prepared MRE samples is inspected by taking images from the microstructure using a laser confocal microscope named commercially as OLYMPUS LEXT OLS4000. Microstructure images are illustrated in Figure 3.7 for the samples of Table 3.1. The white points in the images show the dispersed CIPs and the black background is the silicone rubber matrix. As it can be realized, for isotropic MRE samples (Samples 1 and 2 in Table 3.1),

homogeneous dispersion of particles in the matrix is clearly observed while for the anisotropic MREs (Samples 3 and 4 in Table 3.1), particles are structured in chainlike form.

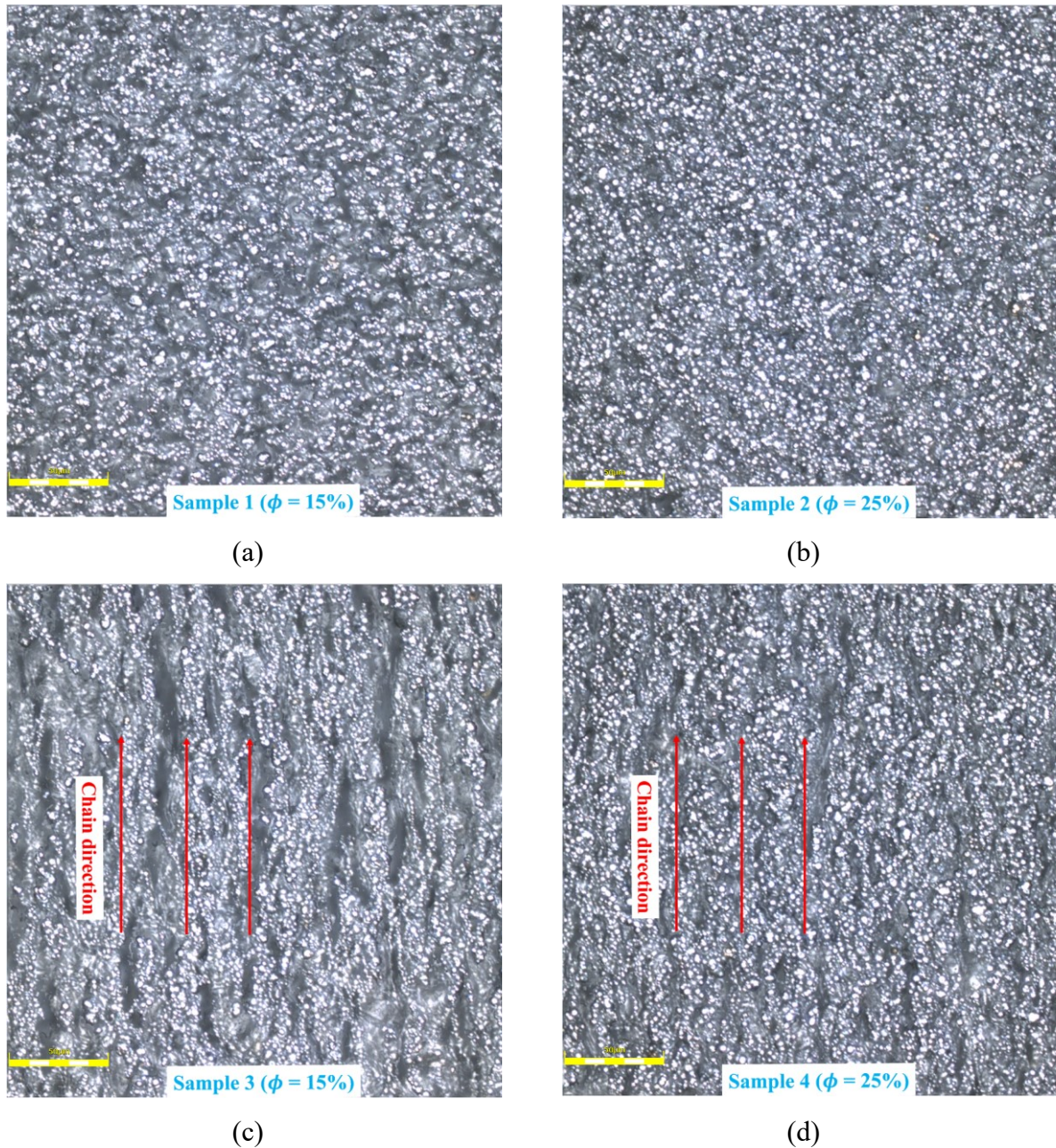


Figure 3.7. Microstructure images of fabricated MRE samples ( $\phi$  is the volume fraction of iron particles). (a) Sample 1, (b) Sample 2, (c) Sample 3, (d) Sample 4

### 3.3.3 Characterization

The four prepared MRE samples are characterized in shear mode using a rotary rheometer (Discovery HR-3, TA Instrument). The rheometer is equipped with a magneto-rheology accessory which makes the instrument capable of providing a uniform magnetic field perpendicular to the direction of shear deformation applied on the MRE sample. The MRE is placed on the bottom geometry and the applied magnetic field is measured using a Hall probe beneath the bottom geometry allowing to measure the magnetic flux density inside the sample. A close-loop controller adjusts the required current input to the magneto-rheology accessory to keep the magnetic field uniform at all times. A parallel upper geometry with 20 mm diameter applies shear deformation on the cylindrical MRE test specimens with the same diameter and a thickness of 1 mm. Figure 3.8 shows the different parts of the rheometer device along with the direction of the applied magnetic field and shear deformation.

Dynamic tests are performed in the linear viscoelastic region by sweeping the driving frequency in the range of 2 Hz to 100 Hz under various levels of applied magnetic flux densities. The resulting torque is automatically measured by the rheometer and is used for data acquisition to obtain the shear stress and dynamic moduli. To be in the linear viscoelastic region, all tests are executed at a small constant shear strain amplitude of 0.01 %. Temperature is kept constant at 25 °C using computer-controlled fluid circulator unit connected to the magneto-rheology accessory. To avoid the slippage between the sample and the geometries, MRE samples are subjected to an axial preload of 10 N in all tests. Experimental results are subsequently used to identify the material constant parameters and evaluate the performance of the developed microstructure-based model.

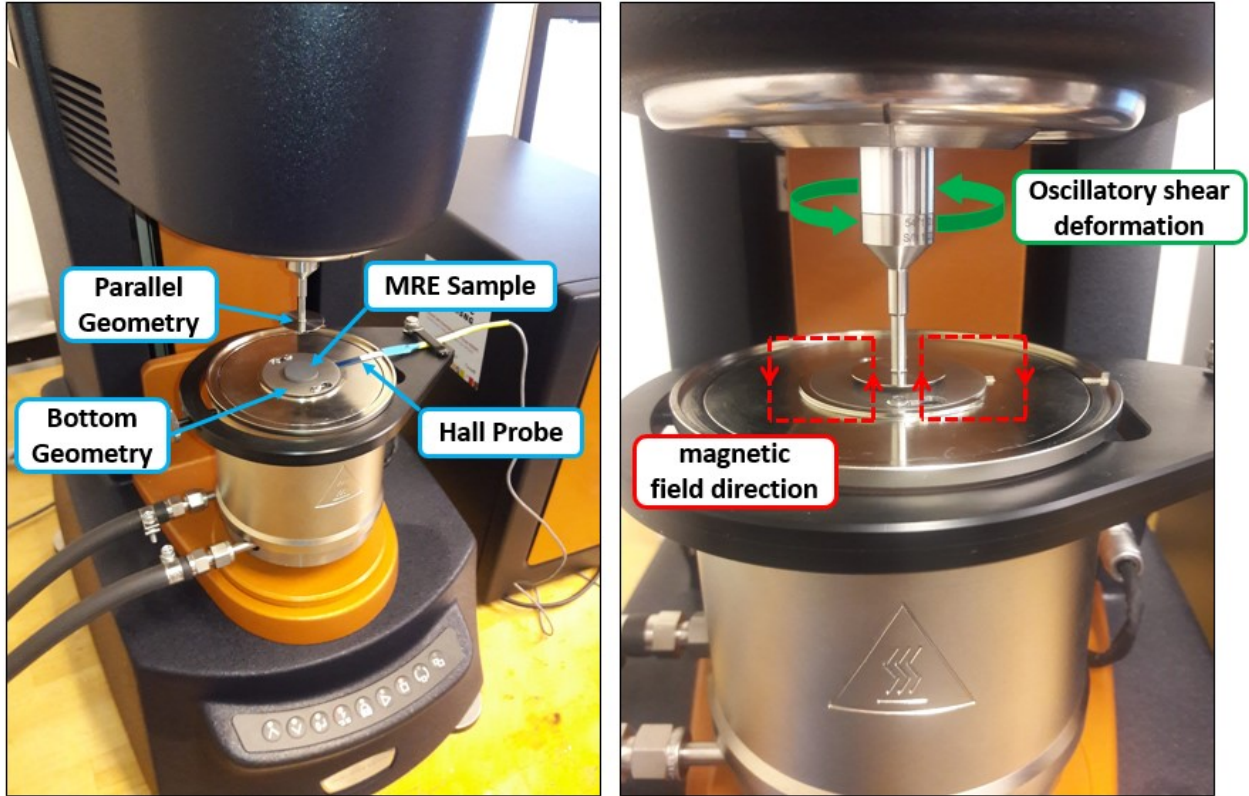


Figure 3.8 Left: Different parts of the rotary rheometer used for dynamic characterization; Right: direction of the magnetic field and shear deformation applied on MRE sample.

### 3.4 Results and Discussion

In this section, the theoretical results based on the proposed microstructure-based model for the storage and loss moduli will be compared with experimental results for both isotropic and anisotropic MREs.

#### 3.4.1 Dynamic Moduli of Isotropic MREs

Results of storage and loss moduli in terms of frequency and magnetic flux density are presented in this section for two MRE materials with isotropic distribution of particles, i.e. Samples 1 and 2 presented in Table 3.1. Using the experimental data, the value of constant parameters in the model are extracted using the least-square optimization method and presented in the Table 3.2.



Table 3.2 Values of constant parameters for isotropic MREs.

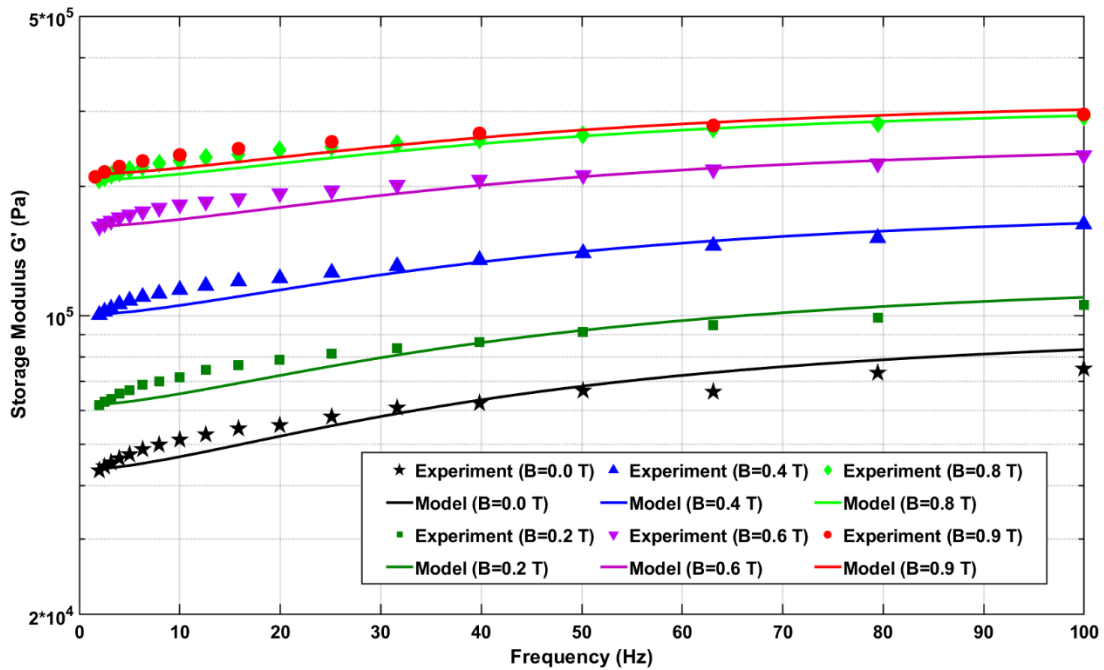
	Sample Type	$\tau_0$	$P$	$s$
Sample 1 Isotropic MRE ( $\phi = 15\%$ )	Storage Modulus ( $G'$ )	$\frac{0.017}{2\pi}$	$5.7 \times 10^9$	0.4
	Loss Modulus ( $G''$ )	$\frac{0.015}{2\pi}$	$1.9 \times 10^9$	0.4
		$\tau_0$	$P$	$s$
Sample 2 Isotropic MRE ( $\phi = 25\%$ )	Storage Modulus ( $G'$ )	$\frac{0.015}{2\pi}$	$5.3 \times 10^9$	0.3
	Loss Modulus ( $G''$ )	$\frac{0.013}{2\pi}$	$1.7 \times 10^9$	0.3

Figure 3.9 shows the variation of the storage and loss moduli with respect to the driving frequency varying from 2 Hz to 100 Hz for an MRE with 15% volume fraction of particles at different magnetic flux density values in the range of 0.0 T to 0.9 T.

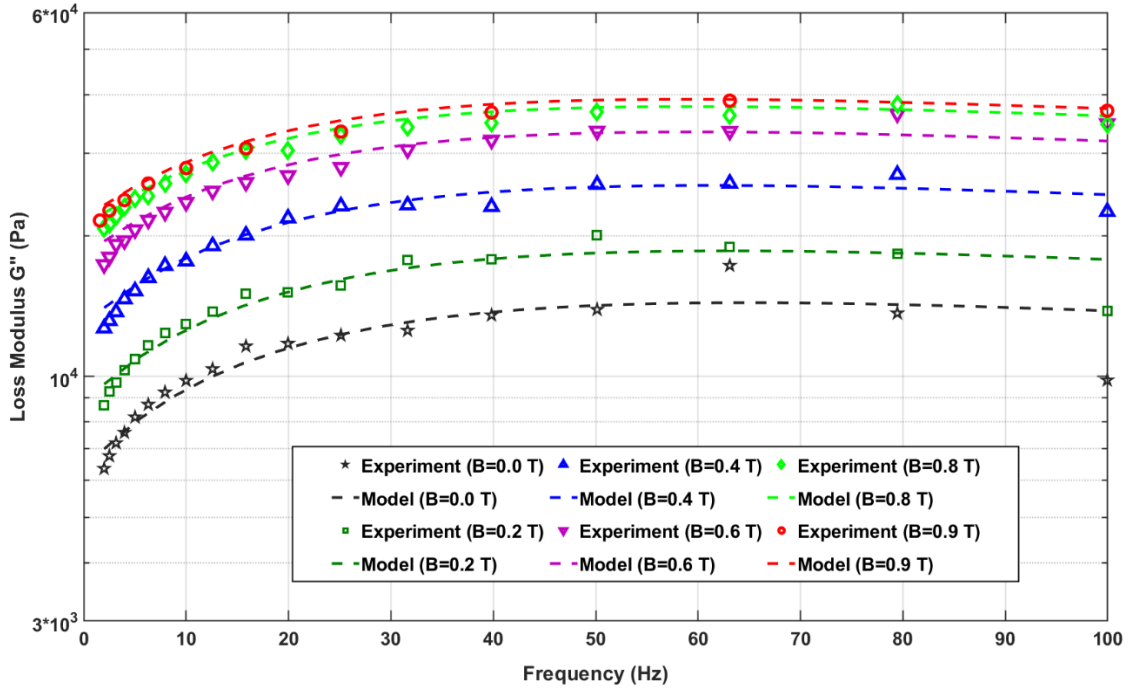
As it can be realized from Figure 3.9 (a), the storage modulus, at fixed values of magnetic flux density, gradually increases with the frequency and approaches a plateau region suggesting saturation at high frequencies. This is a typical trend of both unfilled and composite polymeric materials which show stiffening effect by increasing the excitation frequency [9], [27], [95]. This is mainly attributed to the fact that the cross-linked chains of the host elastomer do not have time to relax at higher excitation frequencies resulting in reduction of the forced relaxation time of the material and subsequently increase in the stiffness. On the other hand, at constant frequency, storage modulus increases with magnetic flux density. Magnetic interaction between particles basically produces a resistive force against chains motion which increases the effective stiffness of the material and thus the storage modulus. At high magnetic flux values, i.e.  $B = 0.8$  T and  $B = 0.9$  T, the storage modulus does not change significantly which implies magnetic saturation of the MRE at high level of magnetic excitation as expected.

Results for the loss modulus shown in the Figure 3.9 (b) also illustrates similar trend with variation of frequency and magnetic field as storage modulus, except that instead of gradual increase with the frequency and reaching to saturation, loss modulus illustrates a maximum value at certain critical frequency and then slightly decreases with further increase of frequency. The

reason of reduction in  $G''$  at high frequencies might be due to the absence of adequate molecular motions capable of dissipating energy within the shortened period of deformation in soft polymers. Similar to storage modulus, the loss modulus initially increases considerably with magnetic flux density until it reaches to saturation at high magnetic flux densities beyond 0.8 T. Thus, it can be inferred that the magnetic interaction between embedded magnetic particles not only makes the material stiffer, but also improves the energy loss processes in the MRE likely due to the increase in interfacial friction between particles and polymer chains.



(a)

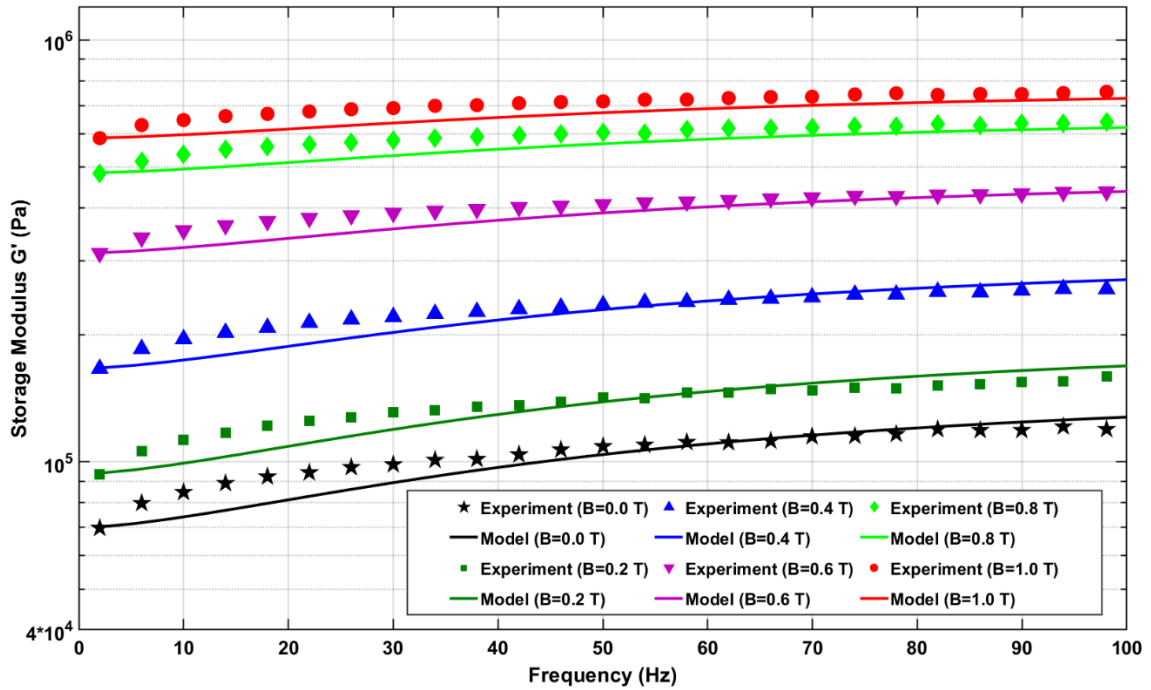


(b)

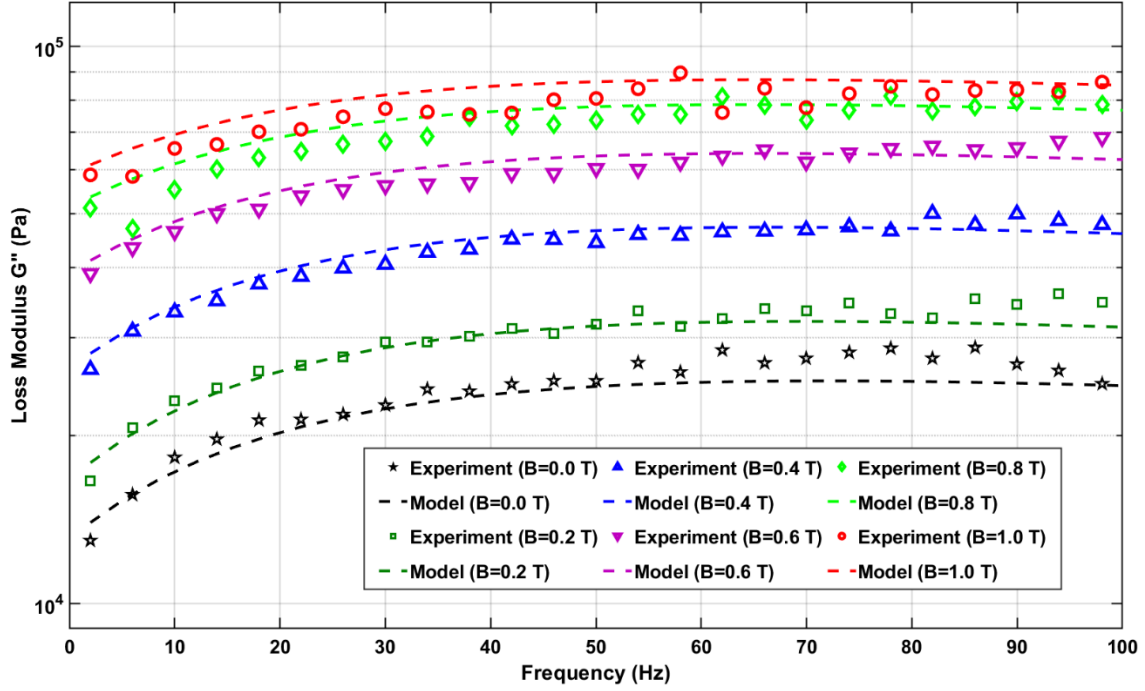
Figure 3.9 Results of dynamic moduli obtained from model and experiment for an MRE with  $\phi = 15\%$  at several magnetic flux densities; (a) Storage modulus,  $G'$ , versus frequency, and (b) Loss modulus,  $G''$ , versus frequency.

Figure 3.10 also shows the results of storage and loss moduli for an isotropic MRE with 25% volume fraction of particles with respect to frequency ranging from 2 Hz to 100 Hz under different magnetic flux density values in the range of 0.0 T to 1.0 T. Similar trend as of Figure 3.9 is also observed here regarding the behavior of dynamic moduli with the frequency and magnetic flux density. However, the order of magnitude and also variation of storage and loss moduli are higher due to the increased volume fraction of magnetic particles in the material suggesting higher MR effect. To have an idea of the increased MR effect, for instance, for a driving frequency of 2 Hz, the storage modulus of MRE with 15% volume fraction of solid particles changes from 43 kPa to 207 kPa as the magnetic field enhances from 0 to 0.8 T, suggesting an absolute increase of 164 kPa (381% relative increase) in the modulus. While, the storage modulus of MRE with 25% volume fraction of CIPs varies from 70 kPa to 483 kPa under the same conditions showing 413 kPa absolute increase (590% relative increase). Similar trend also exists for the loss modulus. In addition, results from Figure 3.10 confirm that for the MRE with higher volume fraction, the saturation of storage and loss moduli occurs at higher flux density values compared with the MRE with lower volume fraction of iron particles.

Figure 3.9 and Figure 3.10 clearly show that the developed model can accurately predict both storage and loss moduli for the isotropic MRE with different volume fractions of CIPs under wide range of frequency and applied magnetic flux density up to the saturation point. To quantify the level of the accuracy of the model, the coefficient of determination,  $R^2$  ( $0 \leq R^2 \leq 1$ ) has been employed in which  $R^2$  close to 1 means perfect fit. Table 3.3 provides the average values of the coefficient of determination over the given range of frequency and magnetic flux density for the storage and loss moduli of both types of isotropic MREs. As it can be realized,  $R^2$  is generally higher than 0.94 for the isotropic MREs. Performance of the model in predicting the dynamic viscoelastic properties of isotropic MRE samples with 15% and 25% volume fraction of iron particles shown in Figure 3.9 and Figure 3.10 proves the efficiency and accuracy of the proposed model for various particle participations in a wide ranges of frequency and applied magnetic field.



(a)



(b)

Figure 3.10 Results of dynamic moduli obtained from model and experiment for an MRE with  $\phi = 25\%$  at several magnetic flux density values (a) Storage modulus,  $G'$ , versus frequency, and (b) Loss modulus,  $G''$ , versus frequency.

Table 3.3 Average values of coefficient of determination ( $R^2$ ) for isotropic and anisotropic MREs.

MRE sample ID	Particles distribution	$R^2$ for	
		$G'$ Storage modulus	$G''$ Loss modulus
Sample 1	Isotropic ( $\phi = 15\%$ )	0.95	0.95
Sample 2	Isotropic ( $\phi = 25\%$ )	0.94	0.94
Sample 3	Anisotropic ( $\phi = 15\%$ )	0.96	0.94
Sample 4	Anisotropic ( $\phi = 25\%$ )	0.96	0.93

### 3.4.2 Dynamic Moduli of Anisotropic MREs

In the case of anisotropic MREs, the dynamic moduli in Eqs. (3.43) and (3.44) would also depend on the anisotropy parameter  $\beta$  whose value was unity for the isotropic MREs. Depending on the level of chain-like structure of particles in the material, the value of  $\beta$  might be different as

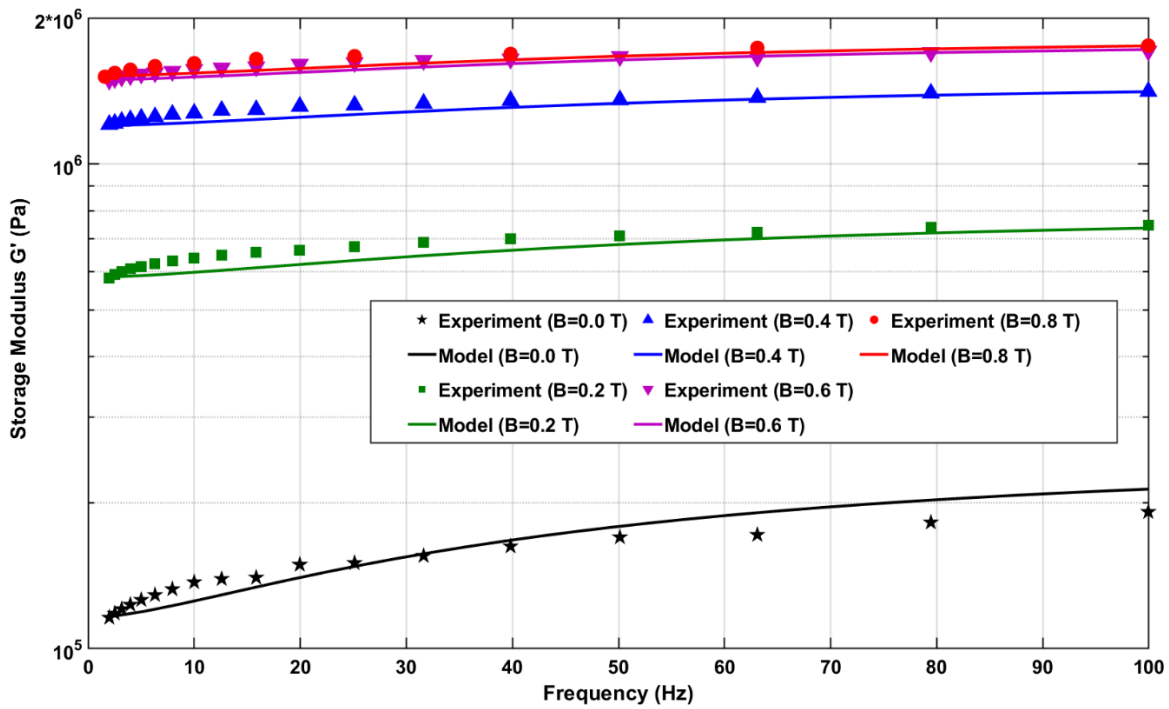
it depends on the particle percentage and magnitude of the applied magnetic field in the curing phase of the fabrication process. Similar to the previous section, values of constant parameters of the model, including  $\beta$ , are obtained employing the least-square optimization aiming at minimizing the error between the model results and experimental data. The identified model parameters are based on the anisotropic MREs with 15% and 25% volume fraction of iron particles (Samples 3 and 4 in Table 3.1) and provided in Table 3.4.

Table 3.4 Values of constant parameters for anisotropic MREs.

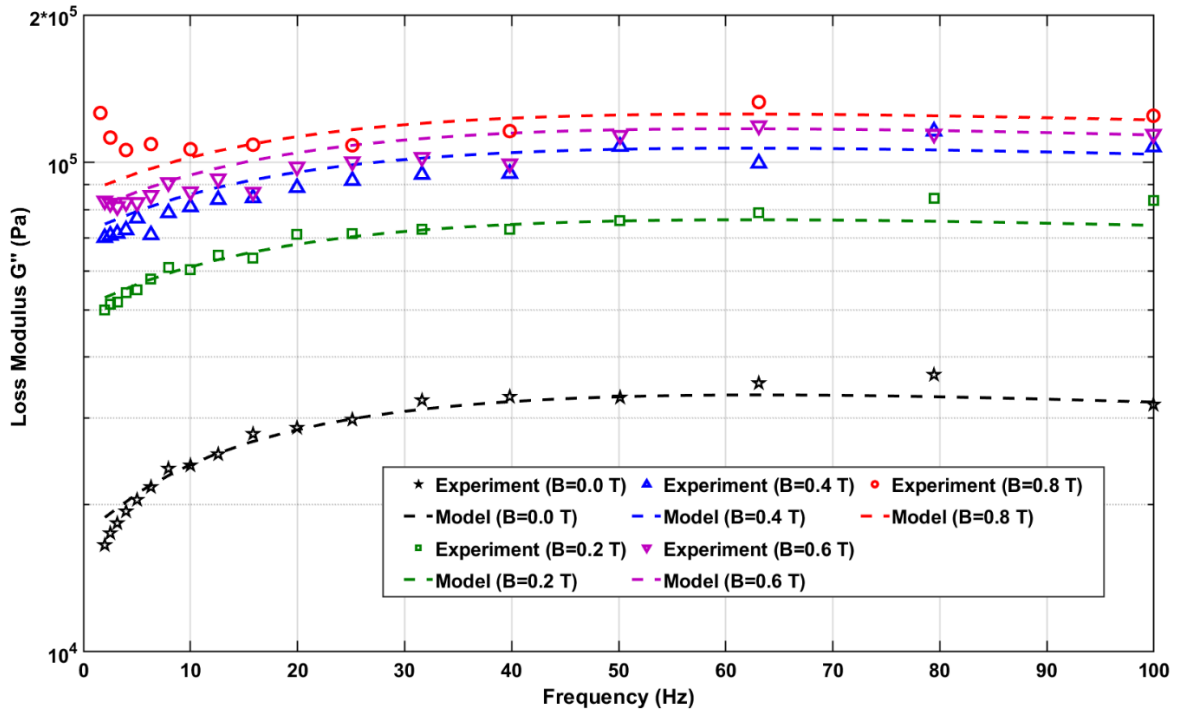
	Sample Type	$\beta$	$\tau_0$	$P$	$s$
Sample 3 Anisotropic MRE ( $\phi = 15\%$ )	Storage Modulus ( $G'$ )	0.55	$\frac{0.02}{2\pi}$	$1.41 \times 10^{10}$	0.2
	Loss Modulus ( $G''$ )	0.55	$\frac{0.018}{2\pi}$	$4.0 \times 10^9$	0.2
		$\beta$	$\tau_0$	$P$	$s$
Sample 4 Anisotropic MRE ( $\phi = 25\%$ )	Storage Modulus ( $G'$ )	0.7	$\frac{0.02}{2\pi}$	$1.33 \times 10^{10}$	0.2
	Loss Modulus ( $G''$ )	0.7	$\frac{0.018}{2\pi}$	$3.8 \times 10^9$	0.2

Figure 3.11 and Figure 3.12 show the theoretical and experimental results for the storage and loss moduli in terms of frequency and flux density for the anisotropic MREs, i.e. Samples 3 and 4 in Table 3.1. Comparison of Figure 3.11 with Figure 3.9, and Figure 3.12 with Figure 3.10, reveals that the magnitude of dynamic moduli at a given magnetic flux density for anisotropic MRE is higher than that for isotropic MRE with same level of volume fraction of iron particles. Thus, as expected, the chain-like distribution of particles yields higher magnetic effect in the material as compared to the isotropic dispersion. Moreover, the storage and loss moduli of the anisotropic MRE show a greater increase by the application of the magnetic field. It means that the anisotropic sample is more sensitive to magnetic induction as also confirmed by observing the results of relaxation spectrum in Section 3.2. It is also noted that, for instance, considering the anisotropic MRE with  $\phi = 15\%$ , the storage and loss moduli do not change significantly in presence of 0.6 T and 0.8 T magnetic flux densities which shows magnetic saturation at lower level of magnetic

induction around 0.6 T compared with the similar isotropic sample with magnetic saturation at  $B = 0.9$  T. The developed model again shows an acceptable performance in predicting the experiment data over the considered range of frequency and magnetic flux density. It is noted that agreement between model and experiments for loss modulus of both anisotropic samples at high flux density values decreases likely due to the change in the type of molecular motion in the material at high field values which is not considered in the model. Similar to the isotropic MREs, the coefficient of determination,  $R^2$  ( $0 \leq R^2 \leq 1$ ) has been calculated for the storage and loss moduli of the anisotropic sample and provided in the last row of Table 3.3. Average values of  $R^2$  for the anisotropic MRE samples are also higher than 0.93 confirming the good accuracy of the developed model.



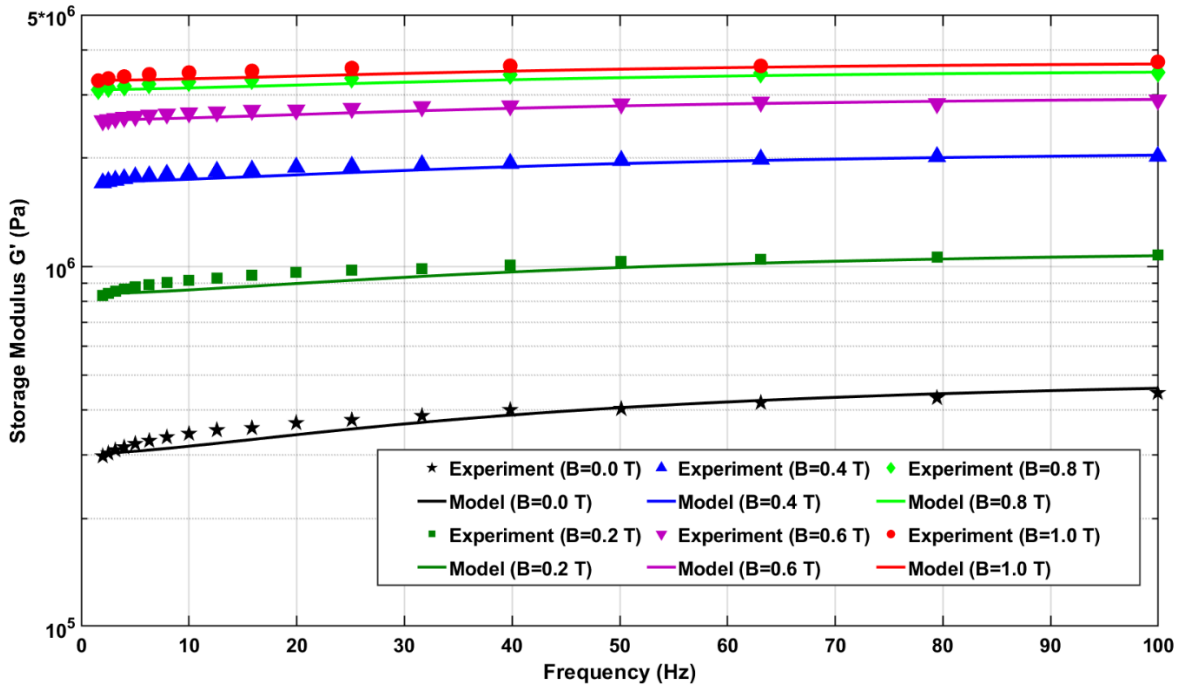
(a)



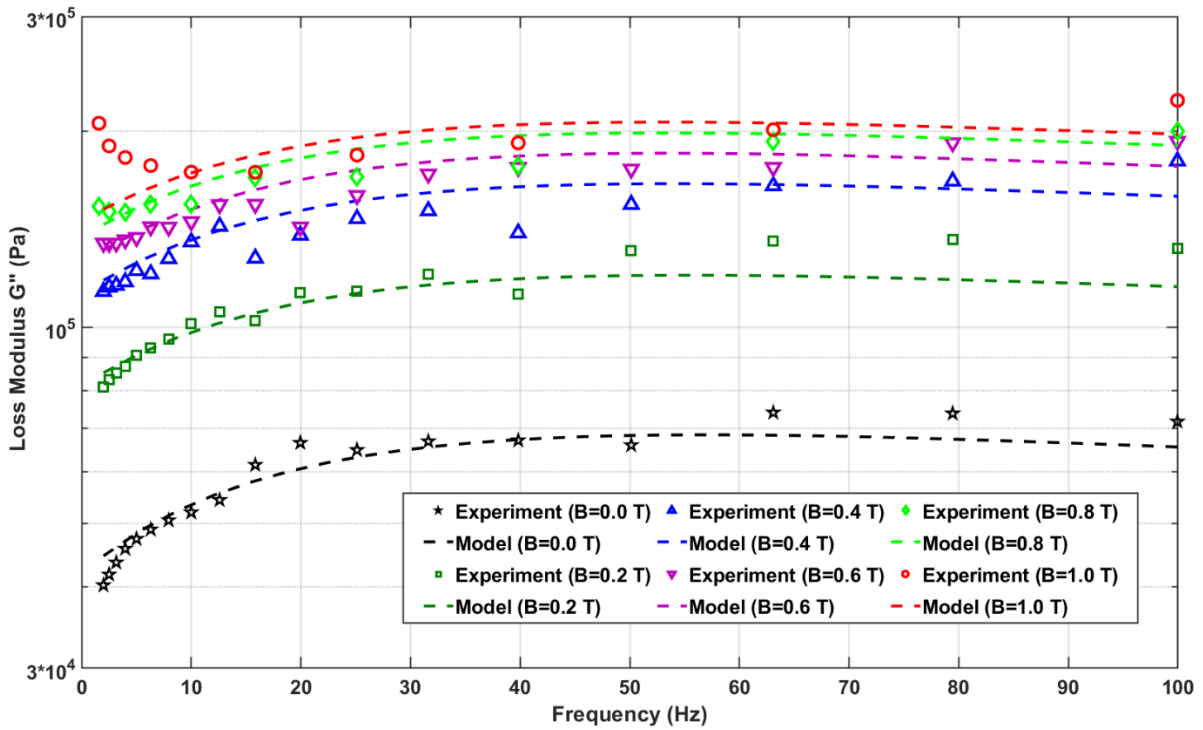
(b)

Figure 3.11 Results of dynamic moduli in terms of frequency obtained from model and experiments for an anisotropic MRE with  $\phi = 15\%$  at several magnetic flux density values; (a) Storage modulus,  $G'$ , and (b) Loss modulus,  $G''$ .





(a)



(b)

Figure 3.12 Results of dynamic moduli in terms of frequency obtained from model and experiment for an anisotropic MRE with  $\phi = 25\%$  at several magnetic flux density values (a)

Storage modulus  $G'$ , and (b) Loss modulus  $G''$

### 3.5 Conclusions

This chapter aimed at dynamic experimental characterization and microstructural modeling of linear viscoelastic response of isotropic and anisotropic MREs which complement the quasi-static modeling of MRE presented in the previous chapter. A microstructure-based model was derived based on a cubic network of particles that are connected with elastic springs and a friction coefficient is assigned to the motion of each particle. To account for the anisotropic MREs, idealized chain-like structure of particles is incorporated into the model by introducing a parameter defining the anisotropy level. The dynamic equation of motion of the particles was extracted by Lagrange's equation and was solved to obtain relaxation times associated with the motion of particles in the network around their equilibrium positions. A dipole saturation model was also employed in the formulations to relate the dynamic characteristics directly to the magnetic flux density which could be directly measured in practice.

The behavior of normal modes relaxation spectrum illustrated splitting of the spectrum under application of magnetic field into two branches associated with the motions parallel and perpendicular to the field direction. The relaxation time corresponding to the motions parallel with the direction of the applied magnetic field increased while the one corresponding to the motions normal to the field direction decreased. For anisotropic distribution of particles, higher MR effect and higher sensitivity to the magnetic induction was observed. A critical magnetic flux density value was calculated in terms of volume fraction of particles and anisotropy of the network to present the threshold beyond which the model gives negative relaxation times. Relations for storage and loss moduli were subsequently derived by using the information of relaxation time spectrum.

To validate the model performance, four MRE samples with isotropic and anisotropic dispersion of particles were fabricated using an elastomeric matrix and different concentrations of ferromagnetic particles. The dynamic moduli of the MRE samples were characterized in shear mode using an advanced rheometer with excitation frequency ranging from 2 Hz to 100 Hz and magnetic flux density varying up to 1 T. The tuning parameters of the proposed model were identified by minimizing the error between experimental data and theoretical results. The storage and loss moduli of the MRE samples showed increasing behavior with magnetic flux density and saturation at high magnetic fields. The increase in the dynamic moduli was improved for higher volume fraction of particles and for anisotropic chain-like dispersion of particles in the material.

The developed model showed a remarkable performance in predicting the experimentally measured storage and loss moduli in a wide range of frequency and magnetic field up to the saturation point for all considered MRE samples. The obtained results demonstrated the suitability of the model for MRE samples with a variety of compositions and distribution of particles. The developed microstructure-based model clarified the relationship between relaxation behavior of the microstructure and dynamic magneto-induced properties of MREs and can be effectively utilized to model and analyze MRE-based adaptive devices at the early stages of design without conducting extensive experimental tests.

## CHAPTER 4

# MULTI-DISCIPLINARY DESIGN OPTIMIZATION OF A NOVEL SANDWICH BEAM-BASED ADAPTIVE TUNED VIBRATION ABSORBER FEATURING MAGNETORHEOLOGICAL ELASTOMER

### 4.1 Introduction

One intriguing application of MREs is in the development of adaptive vibration absorbers which can be effectively utilized to attenuate vibration in a broad range of frequencies. To date, several designs have been proposed in the literature for vibration absorbers featuring MREs as presented in CHAPTER 1 [28], [69]–[72]. However, limited studies reported on the design optimization of MR-based devices have been narrowed to MRF-based dampers and absorbers [96][97][98]–[100][78].

Parlak et al. [96] used finite element-based electromagnetic and CFD tools in ANSYS platform to carry out optimization on an MR damper's geometry aiming to reach the targeted damper force and maximize the magnetic flux density applied to the MRF. Nguyen and Choi [97] proposed an optimal design for a MR damper of passenger vehicles which was constrained in a specific volume. The objective function involved the damping force, dynamic range, and inductive time constant of the damper. In recent years, there have also been a number of studies that investigated the design optimization of rotary and translational MR-based dampers and absorbers [98]–[100]. While conventional MR-based vibration absorbers have been widely investigated before, there is a very limited study on MR-based continuous vibration absorbers. Hirunyapruk et al. [78] proposed a sandwich beam-shaped MRF-based vibration absorber and mainly investigated its feasibility in vibration attenuation of structures and systems.

Looking into the literature, studies on the MRE-based vibration absorbers are limited to the conventional designs which are mostly in the initial stages and have not been optimized to be used in practical applications [57], [70], [71]. Moreover, reported studies mainly focused on the controllability features of MREs in providing variable stiffness vibration absorbers [56], [101] and did not look into MRE-ATVAs as a magneto-mechanical multidisciplinary system. In the present chapter, three different novel configurations for an MRE-based sandwich beam type ATVA are

proposed, and a multidisciplinary optimization framework is developed to maximize their frequency bandwidth under specific design constraints. To this end, comprehensive models of the proposed MRE-ATVAs including (a) finite element (FE) model of the sandwich beam, and (b) mathematical formulation for magnetic analysis of the electromagnets; are developed. The core layer of the sandwich beam is treated with a MRE layer and two electromagnets are installed at the tips of the beam to generate the required magnetic field. Deforming the sandwich beam results in shear deformation in the MRE layer whose shear modulus varies under the applied magnetic field. Thus, the natural frequency of the absorber can be continuously changed and controlled through the application of magnetic field. The electromagnets on the beam ends play a two-fold role by providing the required magnetic field on the MRE layer, as well as oscillating as the absorber mass. To have insights on the flexible design of the proposed absorber device, three different design configurations are considered for the electromagnets. The developed model of the absorber is then utilized to formulate the multidisciplinary design optimization problem. It considers both the structural geometry and electromagnet parameters as design variables and aiming at maximizing the frequency range of the absorber while respecting constraints on the total mass, static deflection, and maximum stress in the beam. To accurately identify the optimal design, the optimization problem is solved using a combination of genetic algorithm (GA) and powerful sequential quadratic programming (SQP) methods. Finally, the performance of the optimally designed MRE-ATVAs with respect to the frequency range and final mass of the device are compared and discussed.

In this chapter, first, the configuration of the proposed MRE-ATVAs with three potential designs of the electromagnet are introduced. Second, the FE model of the sandwich beam and magnetic model of the electromagnets are developed and validated. By integrating the FE model of the beam with the magnetic model of the electromagnets, the high-fidelity model of the absorber device is obtained which is subsequently utilized for the development of the optimization problem. Finally, the multidisciplinary optimization problem is formulated considering both structural and magnetic parameters as design variables aiming at maximizing the frequency bandwidth of the proposed MRE-ATVAs under constraints of mass, size, beam deflection and maximum stress. The optimization results are obtained using the combination of a stochastic based genetic algorithm and a gradient-based SQP programming. Then, the relative performances of the optimal ATVAs are compared and discussed with respect to the frequency range and final mass of the device.

## 4.2 Configuration of the Proposed MRE-Based ATVA

The main components of the proposed MRE-ATVA are a three-layer sandwich beam and two electromagnets attached at its ends. The sandwich beam consists of an MRE core layer which is constrained between two thin steel layers. The MRE-based sandwich beam provides a unique opportunity to provide distributed control force through variation in the stiffness and damping of the MRE layer. Two electromagnets are installed on both ends of the sandwich beam which not only provide the required magnetic field for the activation of the MRE but also acts as the absorber's active mass. Moreover, the locations of the electromagnets across the length of the beam may also be different to enhance the authority of the proposed MRE-ATVA for different frequency ranges. The schematic design of the proposed MRE-ATVA is illustrated in Figure 4.1. The MRE core layer is under shear deformation while the magnetic flux lines, shown by arrows in Figure 4.1, are perpendicular to the shear direction. The shear stiffness of the MRE is adjusted by varying the magnetic field through changing the current supplied to the coils of the electromagnets. Hence, the stiffness and subsequently the natural frequency of the absorber can be tuned to the desired frequency. The proposed MRE-ATVA may be attached from its middle point to the host system to mitigate vibration within the operating frequency range.

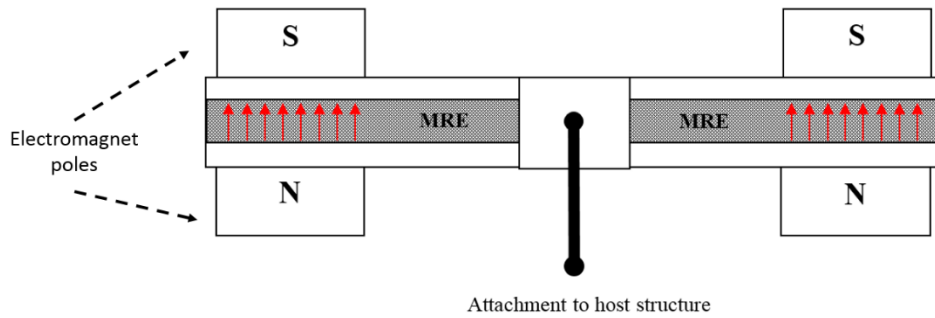


Figure 4.1 Schematic of the proposed MRE-based sandwich beam type ATVA.

Three different shapes including H-shaped, C-shaped, and U-shaped designs are considered for the electromagnets in the present study. In-plane (2D) and in-space (3D) sketches of the proposed configurations are illustrated in Figure 4.2. The characteristics and performance of each design might be different in terms of the induced magnetic flux density in the gap and mass of the electromagnet.

As shown in Figure 4.2, the H-shaped electromagnet has four coils of two different sizes. The C-shaped electromagnet has three coils from which two of them are of the same size. The U-shaped electromagnet has four similar coils. The conductive core of the electromagnets has a square cross

section with an edge size of  $t$ . The path of magnetic flux in the core of each electromagnet is shown with dashed line.

The schematics of the assembled structure of the MRE-ATVA with each of the three electromagnet configurations, are also shown in Figure 4.3. As it can be realized, the proposed MRE-ATVAs are symmetric from the center of the sandwich beam and thus each behaves similar to two connected cantilever beams. Therefore, half of the MRE-ATVA which is a cantilever sandwich beams with one electromagnet, attached at the free end, will be considered for the optimization problem in the modeling and optimization formulation.

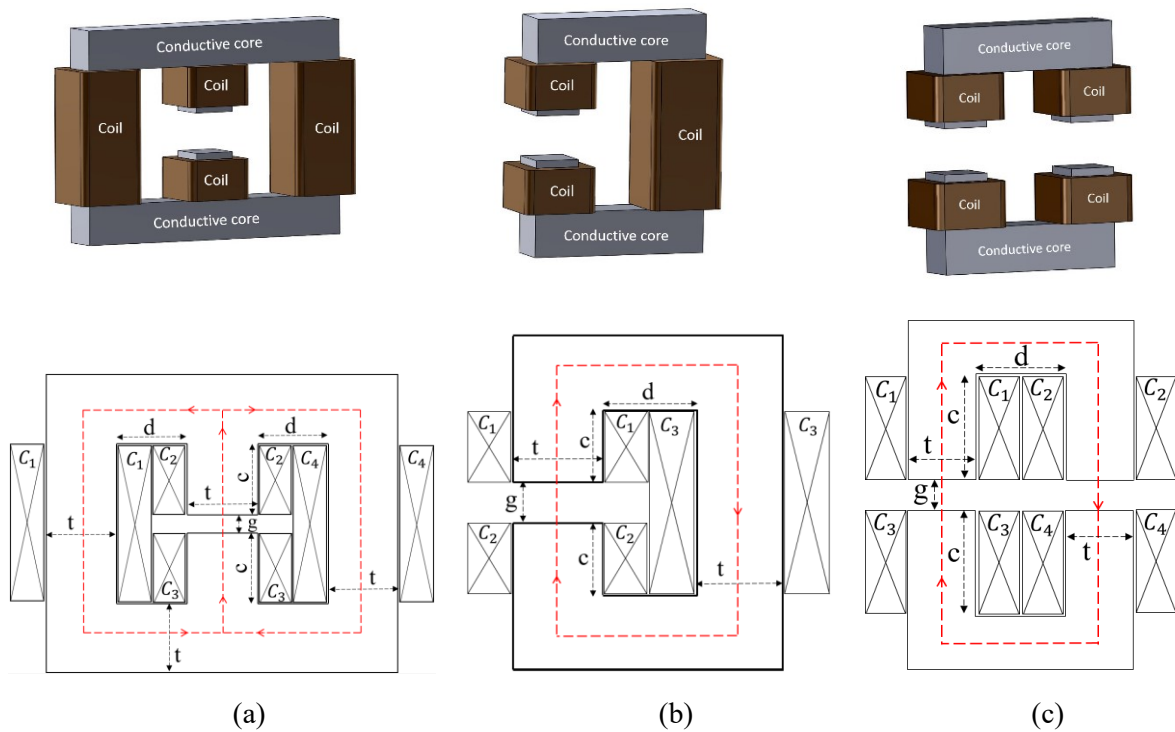
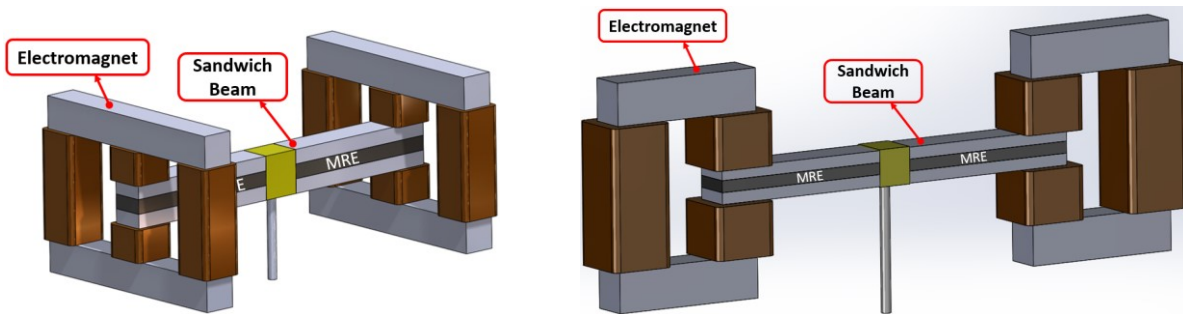


Figure 4.2 Three electromagnet designs considered for the ATVA; (a) H-shaped electromagnet, (b) C-shaped electromagnet, and (c) U-shaped electromagnet.



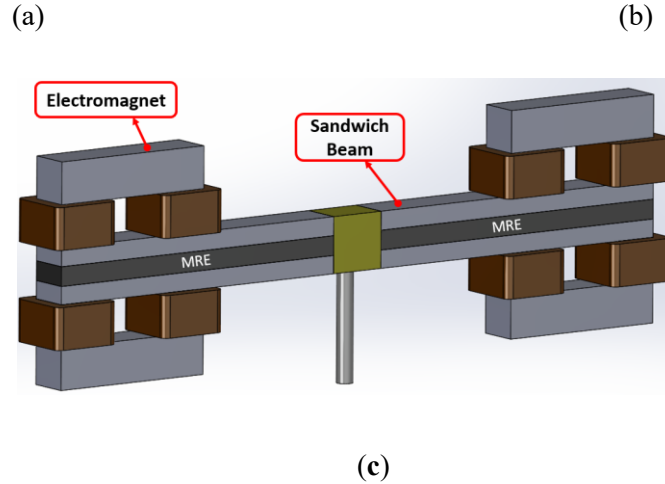


Figure 4.3 Schematics of the assembled ATVA structure with three different electromagnet designs; (a) H-shaped electromagnet, (b) C-shaped electromagnet, and (c) U-shaped electromagnet.

### 4.3 Mechanical and Magnetic Properties of Materials

In this section, mechanical and magnetic properties of the MRE and steel materials which are respectively used as the core and surface layers of the sandwich beam, are provided. These material properties are utilized in the modeling and design optimization of the MRE-ATVA in the next sections of this chapter. An isotropic MRE sample with 40% volume fraction of iron particles from CHAPTER 2 is considered and its properties are adopted to be used here. This MRE sample has shown the maximum MR effect which is important to get a wide frequency range for the ATVA. The sample was fabricated using silicone rubber as the elastomeric matrix material and soft type ferromagnetic carbonyl iron particles as the magnetic fillers. The selected silicone rubber has low viscosity which facilitates the distribution of magnetic fillers in the matrix and ensures easy mixing and degassing. Density of the MRE sample is  $3500 \text{ kg/m}^3$ . Figure 4.4 shows the variation of its storage modulus ( $G'$ ) with respect to the applied magnetic flux density ( $B$ ) taken from the experimental characterization tests presented in CHAPTER 2.

A fourth-order polynomial is fitted to the experimental data to accurately estimate the storage modulus as a function of applied magnetic flux density as follows:

$$G' = -1.36 \times 10^7 B^4 + 2.47 \times 10^7 B^3 - 9.66 \times 10^6 B^2 + 1.52 \times 10^6 B + 9.35 \times 10^4$$

$$0 \leq B \leq 1 \text{ T} \quad (4.1)$$

where  $G'$  is in kPa and  $B$  in Tesla (T). It is assumed that for the flux density values more than 1.0 T, the MRE sample is magnetically saturated and so the storage modulus remains constant and



equal to its value at 1.0 T of magnetic field. The performance of the polynomial function in obtaining the storage modulus is presented in Figure 4.4.

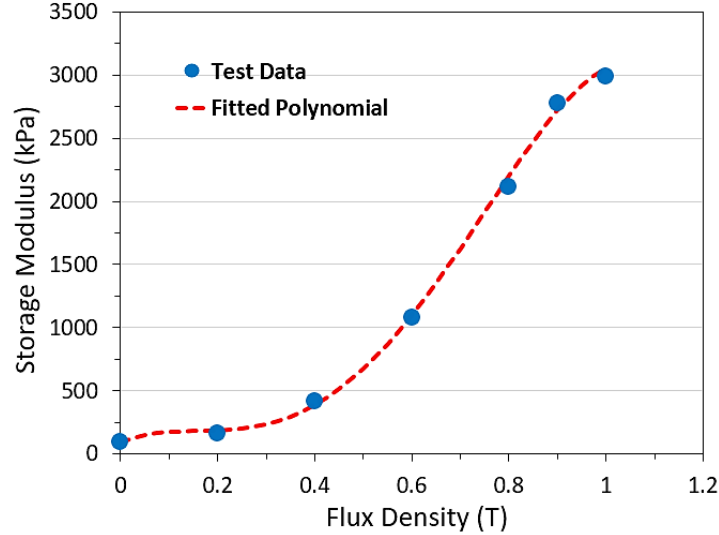


Figure 4.4 Storage modulus in terms of flux density for isotropic MRE sample with 40% volume fraction of CIPs.

In addition to the mechanical properties, magnetic characteristics are also required for modeling and optimization of the proposed MRE-ATVA. Considering that MRE and MRF both have similar mechanisms for responding to a magnetic field and due to the lack of appropriate data for MRE, the B-H curve shown in Figure 4.5 which is for a MRF with the trade name of MRF-132DG from Lord Corporation (Cary, NC, United States) [102] is used in the present work. For the sake of modeling, a second order polynomial, shown by dashed line in Figure 4.5, is fitted to the B-H curve that represents the magnetic intensity,  $H$  (kA/m), as a function of flux density,  $B$  (T), in the following form:

$$H_{\text{MRE}} = 2.89 \times 10^2 B^2 + 3.4 \times 10 B \quad (4.2)$$

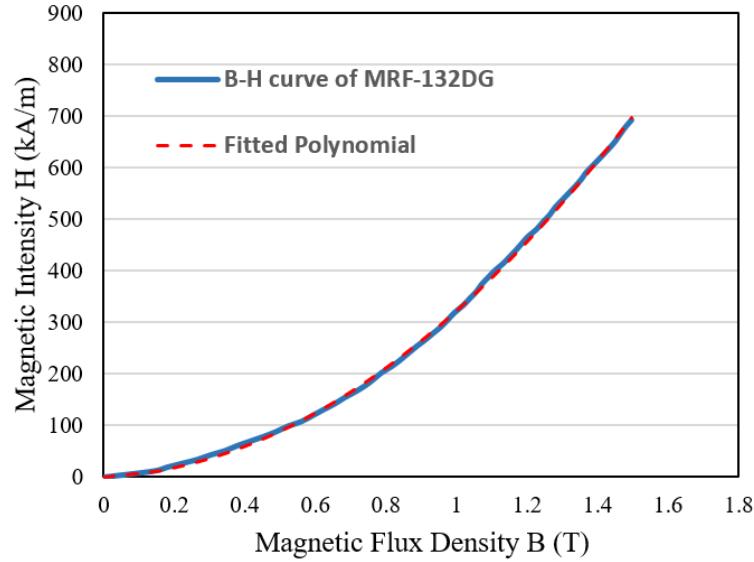


Figure 4.5 The B-H curve of MRF-132DG from Lord Corporation.

The conductive core of the electromagnet and elastic face layers of the sandwich beam are assumed to be made of 1008 steel material with a density of  $7861 \text{ kg/m}^3$ , elastic modulus of 200 GPa, and yield strength of 285 MPa. Data of B-H curve of this steel type is taken from [103] as demonstrated in Figure 4.6. The relationship between the magnetic field intensity,  $H$  (kA/m), and magnetic flux density,  $B$  (T), of the 1008 steel is obtained by a curve fitting in [103] with the following polynomial as:

$$H_{\text{steel}} = R_{s0}B^5 + R_{s1}B^4 + R_{s2}B^3 + R_{s3}B^2 + R_{s4}B + R_{s5} \quad (4.3)$$

where the coefficients are defined as below:

$$R_s = \begin{cases} [0 \ 1.82 \ -3.63 \ 1.782 \ 0.387 \ 0] & B \leq 1.5 \text{ T} \\ [-1419.52 \ 13551.37 \ -50744.31 \ 93520.50 \ -85032.46 \ 30566.42] & B > 1.5 \text{ T} \end{cases}$$

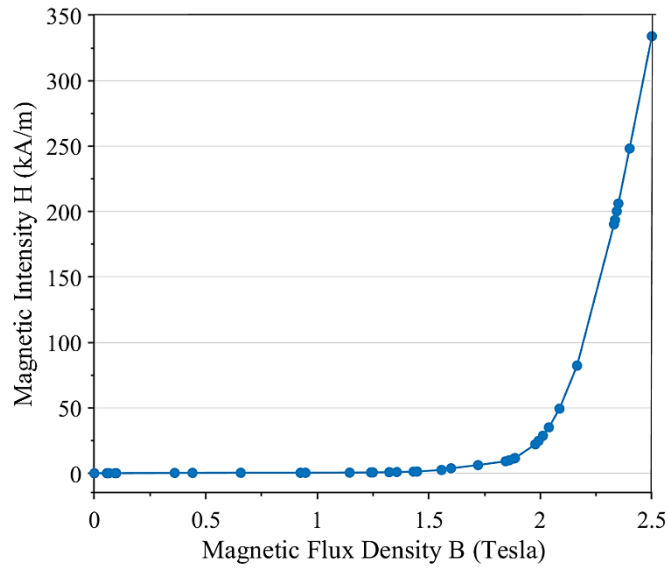


Figure 4.6 The B-H curve of 1008 steel.

It is noted that coils of the electromagnets are made of 17 AWG wire with an approximate diameter of  $D = 1.15$  mm [104] and density of  $7100$  kg/m<sup>3</sup>. With this size, the maximum current that the wire can withstand is expected to be 5 A. The material properties given above will be used in the modeling and optimization of the MRE-ATVA in the following sections.

#### 4.4 Finite Element Modeling of the Three-Layer Sandwich Beam

A three-layer sandwich beam with MRE in the core layer is considered as shown in the Figure 4.7. Since magnetic field is provided only on specific parts of the MRE layer where the electromagnets are installed, those portions exposed to the magnetic field will be activated and the rest of the beam will be inactive with constant properties. Considering this, the FE model is developed for sandwich beam with the ability to change the stiffness of only active parts of the MRE core layer. This is similar to the situations where the sandwich beam is partially treated with MRE in the core layer. The location of electromagnets and thus the position of active parts of MRE could be varied along the beam.

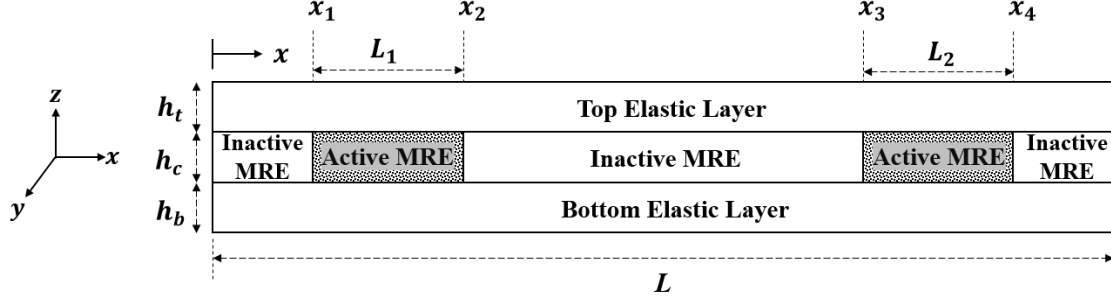


Figure 4.7 Schematic of the sandwich beam structure with MRE-core layer.

Logical simplifying assumptions including (a) no slippage between the core layer and the elastic layers, (b) uniform transverse displacement in a given cross section of the beam, (c) negligible normal stresses in the core layer, and (d) negligible transverse shear strain in the two elastic layers; are considered to obtain the governing equations of motion of the sandwich beam through FE analysis [105]–[107]. Using the first order shear deformation theory, the displacement field for each layer at an arbitrary section along the beam span can be expressed as:

$$u_i(x, z_i, t) = u_i^0(x, t) - z_i \frac{\partial w_i(x, t)}{\partial x} \quad i = t, c, b \quad (4.4)$$

$$w_i(x, z_i, t) = w(x, t) \quad i = t, c, b \quad (4.5)$$

where  $u_i$  is the longitudinal displacement along the  $x$  direction and  $u_i^0$  is the displacement of the mid-plane of the layer which is also the origin of the coordinate  $z_i$  for each layer.  $w_i$  is the transverse displacement of each layer equal to the uniform transverse displacement of the beam  $w$ . The subscripts  $i = t, c$ , and  $b$  refers to the corresponding top, core, and bottom layers, respectively. The condition of No-slippage at the interfaces of the three layers yields the following relation:

$$u_c \Big|_{z_c = \frac{h_c}{2}} = u_t \Big|_{z_t = -\frac{h_t}{2}} \quad ; \quad u_c \Big|_{z_c = -\frac{h_c}{2}} = u_b \Big|_{z_b = \frac{h_b}{2}} \quad (4.6)$$

By substituting Eq. (4.6) into Eqs. (4.4) and (4.5), displacement of the mid-plane of the core layer can be obtained based on the displacement of the bottom and top layers as:

$$u_c^0 = \frac{u_t^0 + u_b^0}{2} + \frac{1}{4} \frac{\partial w}{\partial x} (h_t - h_b) \quad (4.7)$$

Movements of the elastic top and bottom layers results in shear deformation in the core layer. The transverse shear strain of the core layer in the  $x$ - $z$  plane can thus be calculated by taking derivatives of the displacements as:

$$\gamma_c^{xz} = \frac{\partial w}{\partial x} + \frac{\partial u_c}{\partial z_c} \quad (4.8)$$

in which,

$$\frac{\partial u_c}{\partial z_c} = \frac{(h_t + h_b)}{2h_c} \frac{\partial w}{\partial x} + \frac{(u_t^0 - u_b^0)}{h_c} \quad (4.9)$$

Thus, the transverse shear strain in Eq. (4.8) can be described as follows using Eq. (4.9):

$$\gamma_c^{xz} = \frac{D}{h_c} \frac{\partial w}{\partial x} + \frac{(u_t^0 - u_b^0)}{h_c} \quad (4.10)$$

where  $D = h_c + \frac{1}{2}(h_t + h_b)$ . The shear stress in the core layer can be obtained as:

$$\tau_c^{xz} = G_c^* \gamma_c^{xz} \quad (4.11)$$

where  $G_c^*$  is the complex shear modulus of the core layer which can be described as:

$$G_c^* = G_c' + jG_c'' = G_c'(1 + j\hat{\beta}) \quad (4.12)$$

where  $G_c'$  and  $G_c''$  are the storage and loss moduli of the viscoelastic core layer, respectively, and  $\hat{\beta}$  is the loss factor of the core layer.

Total strain energy comprises three different parts including bending and extension of the elastic layers and shear deformation of the core layer. The strain energy due to the bending and extension of the top and bottom layers can be written as:

$$V_{t,b} = \frac{1}{2} \int_0^L \left( E_t A_t \left( \frac{\partial u_t}{\partial x} \right)^2 + E_b A_b \left( \frac{\partial u_b}{\partial x} \right)^2 \right) dx + \frac{1}{2} \int_0^L (E_t I_t + E_b I_b) \left( \frac{\partial^2 w}{\partial x^2} \right)^2 dx \quad (4.13)$$

where  $E_i$  is the elastic modulus of the  $i$ -th layer ( $i = t, b$ ),  $A_i$  is the cross sectional area, and  $I_i$  is the second moment of inertia around the centroid of the layer's cross section. The strain energy of the viscoelastic core layer is mainly due to the shear deformations, which can be expressed as:

$$\begin{aligned} V_c &= \frac{1}{2} \int_0^L \tau_c^{xz} \gamma_c^{xz} A_c dx \\ &= \frac{1}{2} \int_0^L (G_c^* A_c \gamma_c^{xz2}) dx = \frac{1}{2} \int_0^L G_c^* A_c \left[ \frac{D}{h_c} \frac{\partial w}{\partial x} + \frac{(u_t^0 - u_b^0)}{h_c} \right]^2 dx \end{aligned} \quad (4.14)$$

Now, the total strain energy of the sandwich beam can be calculated as:

$$V = V_{t,b} + V_c \quad (4.15)$$

Similarly, the kinetic energy is mainly due to the axial and transverse displacements of the elastic and core layers. The kinetic energy associated with the axial displacement of the elastic top

and bottom layers,  $T_{ax}$ , and also due to the transverse displacement of two elastic layers and viscoelastic core layer,  $T_{tran}$ , can be written as:

$$T_{ax} = \frac{1}{2} \int_0^L \left( \rho_t A_t \left( \frac{\partial u_t}{\partial t} \right)^2 + \rho_b A_b \left( \frac{\partial u_b}{\partial t} \right)^2 \right) dx \quad (4.16)$$

and,

$$T_{tran} = \frac{1}{2} \int_0^L (\rho_t A_t + \rho_c A_c + \rho_b A_b) \left( \frac{\partial w}{\partial t} \right)^2 dx \quad (4.17)$$

Now, the total kinetic energy can be described as:

$$T = T_{ax} + T_{tran} \quad (4.18)$$

To construct the FE model of the structure, a one-dimensional two-node sandwich beam element with three layers has been considered. Each node at the terminals of the element, has four degrees of freedom including the longitudinal displacements of the top and bottom layers ( $u_t, u_b$ ), transverse displacement ( $w$ ), and slope ( $\frac{\partial w}{\partial x} = w_x$ ) of the beam. Accordingly, the element nodal displacement vector can be written as:

$$q^e(t) = \{q^1 \ q^2\}^T = \{u_t^1, u_b^1, w^1, w_x^1, u_t^2, u_b^2, w^2, w_x^2\}^T \quad (4.19)$$

where  $q^1 = \{u_t^1, u_b^1, w^1, w_x^1\}^T$ , and  $q^2 = \{u_t^2, u_b^2, w^2, w_x^2\}^T$  are the nodal displacement vector at node 1 and 2 of the sandwich beam element, respectively. The longitudinal and transverse displacements of the mid-plane at each point can be expressed in terms of the elemental displacement vector  $q^e(t)$  and shape functions as below:

$$\begin{aligned} u_t^0(x, t) &= N_{ut}(x)q^e(t) \\ u_b^0(x, t) &= N_{ub}(x)q^e(t) \\ w(x, t) &= N_w(x)q^e(t) \end{aligned} \quad (4.20)$$

Here, we have utilized linear shape function for the longitudinal displacements and cubic shape function for the transverse displacement as:

$$\begin{aligned} N_{ut}(x) &= \left[ \left(1 - \frac{x}{L_e}\right), 0, 0, 0, \left(\frac{x}{L_e}\right), 0, 0, 0 \right] \\ N_{ub}(x) &= \left[ 0, \left(1 - \frac{x}{L_e}\right), 0, 0, 0, \left(\frac{x}{L_e}\right), 0, 0 \right] \\ N_w(x) &= \left[ 0, 0, \left(1 - \frac{3x^2}{L_e^2} + \frac{2x^3}{L_e^3}\right), \left(x - \frac{2x^2}{L_e} + \frac{x^3}{L_e^2}\right), 0, 0, \left(\frac{3x^2}{L_e^2} - \frac{2x^3}{L_e^3}\right), \left(-\frac{x^2}{L_e} + \frac{x^3}{L_e^2}\right) \right] \end{aligned} \quad (4.21)$$

where  $L_e$  is length of the element. Substituting Eqs. (4.20) and (4.21) into Eqs. (4.4) and (4.5), and then by substituting the resulting displacement field into energy relations, the potential energy described in Eq. (4.15) can be found in the matrix form with respect to the element nodal displacement vector as:

$$V = \frac{1}{2} \{q^e\}^T ([K_1] + [K_2] + [K_3] + [K_4]) \{q^e\} \quad (4.22)$$

where  $[K_i]$ ,  $i = 1,2,3,4$  are obtained as:

$$\begin{aligned} [K_1] &= \int_0^{L_e} \left( E_t A_t \left[ \frac{dN_{ut}}{dx} \right]^T \left[ \frac{dN_{ut}}{dx} \right] + E_b A_b \left[ \frac{dN_{ub}}{dx} \right]^T \left[ \frac{dN_{ub}}{dx} \right] \right) dx \\ [K_2] &= \int_0^{L_e} \left( \frac{h_t^2}{12} + \frac{h_b^2}{12} \right) \left[ \frac{d^2 N_w}{dx^2} \right]^T \left[ \frac{d^2 N_w}{dx^2} \right] dx \\ [K_3] &= \int_0^{L_e} (E_t I_t + E_b I_b) \left[ \frac{d^2 N_w}{dx^2} \right]^T \left[ \frac{d^2 N_w}{dx^2} \right] dx \\ [K_4] &= \int_0^{L_e} G_c^* A_c \left[ \frac{D}{h_c} \left[ \frac{dN_w}{dx} \right] + \left( \frac{[N_{ut}] - [N_{ub}]}{h_c} \right) \right]^T \left[ \frac{D}{h_c} \left[ \frac{dN_w}{dx} \right] + \left( \frac{[N_{ut}] - [N_{ub}]}{h_c} \right) \right] dx \end{aligned} \quad (4.23)$$

Similarly, the kinetic energy of the element given in Eq. (4.18) yields the following relation:

$$T = \frac{1}{2} \{\dot{q}^e\}^T ([M_1] + [M_2] + [M_3] + [M_4]) \{\dot{q}^e\} \quad (4.24)$$

where  $[M_i]$ ,  $i = 1,2,3,4$  are defined as:

$$\begin{aligned} [M_1] &= \int_0^{L_e} (\rho_t A_t [N_{ut}]^T [N_{ut}] + \rho_b A_b [N_{ub}]^T [N_{ub}]) dx \\ [M_2] &= \int_0^{L_e} (\rho_t A_t + \rho_c A_c + \rho_b A_b) [N_w]^T [N_w] dx \\ [M_3] &= \int_0^{L_e} \frac{1}{12} \left( \rho_t A_t h_t^2 \left[ \frac{dN_w}{dx} \right]^T \left[ \frac{dN_w}{dx} \right] + \rho_b A_b h_b^2 \left[ \frac{dN_w}{dx} \right]^T \left[ \frac{dN_w}{dx} \right] \right) dx \\ [M_4] &= \int_0^{L_e} \frac{\rho_c A_c h_c^2}{12} \left[ \frac{D}{h_c} \left[ \frac{dN_w}{dx} \right] + \left( \frac{[N_{ut}] - [N_{ub}]}{h_c} \right) \right]^T \left[ \frac{D}{h_c} \left[ \frac{dN_w}{dx} \right] + \left( \frac{[N_{ut}] - [N_{ub}]}{h_c} \right) \right] dx \end{aligned} \quad (4.25)$$

Finally, the governing equations of motion can be obtained using Lagrange's energy method as follows:

$$\frac{d}{dt} \left( \frac{\partial T}{\partial \dot{q}_i} \right) - \frac{\partial T}{\partial q_i} + \frac{\partial V}{\partial q_i} = F_i \quad i = 1, \dots, n \quad (4.26)$$

where  $q_i$  is the  $i$ -th degree of freedom of an element,  $F_i$  is the generalized force corresponding to the  $i$ -th degree of freedom and  $n$  is the total number of degrees of freedom of the element. By

using energy terms in matrix forms in Eqs. (4.22) and (4.24) into Lagrange's equations, the governing equations of motion for the sandwich beam element can be written in FE form as:

$$[M^e]\{\ddot{q}_e\} + [K^e]\{q^e\} = \{F^e\} \quad (4.27)$$

where  $[M^e] = [M_1] + [M_2] + [M_3] + [M_4]$  is the element mass matrix and  $[K^e] = [K_1] + [K_2] + [K_3] + [K_4]$  is the element stiffness matrix.  $\{q^e\}$  and  $\{\ddot{q}_e\}$  are the vectors of nodal displacements and nodal accelerations, respectively, and  $\{F^e\}$  is the elemental force vector. By assembling the mass and stiffness matrices for all the elements, the governing equations of motion of the sandwich structure are obtained as:

$$[M]\{\ddot{Q}\} + [K]\{Q\} = \{F\} \quad (4.28)$$

where  $[M]$  is the system mass matrix,  $[K]$  is the system stiffness matrix,  $\{Q\}$  and  $\{\ddot{Q}\}$  are the system vectors of nodal displacements and accelerations, respectively, and  $\{F\}$  is the system load vector. It should be noted that the elemental mass and stiffness matrices should be assembled respecting the partial or full treatment of the core layer with MRE.

To find the natural frequency and loss factor of the sandwich beam, the problem of free vibration is studied considering  $\{F\} = \vec{0}$  in Eq. (4.28). Then, the resulting eigenvalue problem is solved to calculate the eigenvalues of the system. The square root of the real part of the eigenvalues provides the natural frequencies of the system while the ratio of the imaginary part to the real part of the eigenvalues yields the loss factor. It is noted that the developed FE model of the sandwich beam is programmed in a MATLAB<sup>®</sup> environment.

#### 4.4.1 Validation of the developed FE model

The developed FE model of the sandwich beam has been validated through comparison of the results with those reported by Mead and Markus [108] using analytical approach for a clamped-clamped sandwich beam with two elastic face layers and a viscoelastic core layer. Figure 4.8 shows the results for the resonant frequency of the sandwich beam with respect to dimensionless shear parameter which is defined in the Eqs. (3a) and (3b) in page 101 of [108]. Results are shown for three different values of geometric parameter  $Y$  as defined in Eq. (4a) in [108] and the loss factor of the core layer is set at  $\beta=1$ . As it can be realized, excellent agreement exists between FE and analytical results.



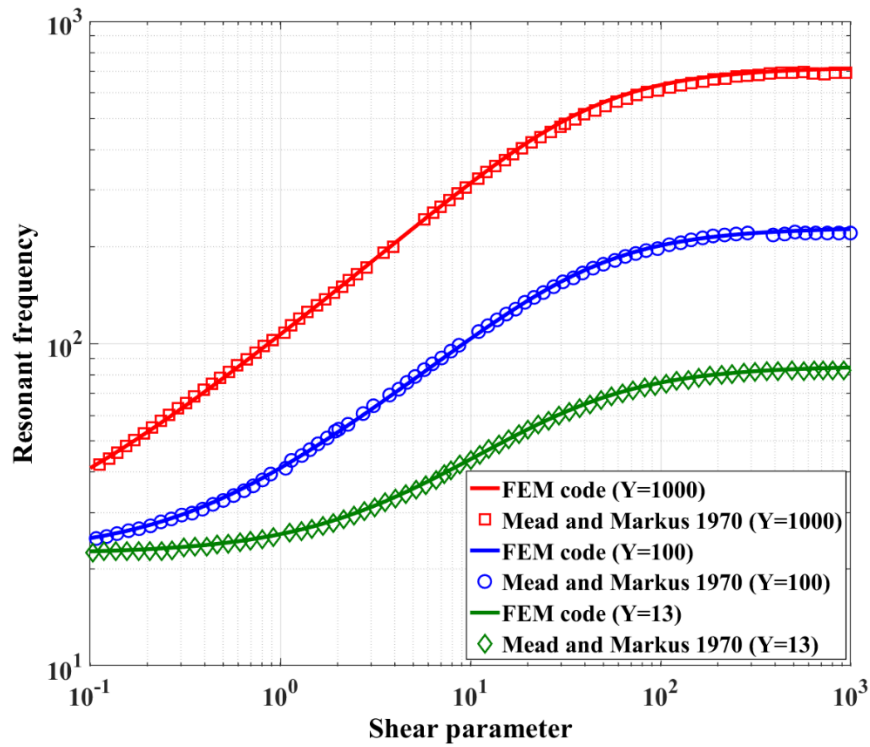


Figure 4.8 Comparison of the results of developed FE model with the analytical results of Mead and Markus [108].

#### 4.5 Magnetostatic Modeling and Analysis of the Electromagnets

The shear modulus of the active portions of the MRE core layer depends on the applied magnetic field by the electromagnets. Here, the analytical magnetic circuit model for different proposed configuration of electromagnets is presented and then validated using magnetostatic FE analysis. The analytical models can then be effectively utilized to evaluate the applied magnetic flux density at the center of the gap where the sandwich beam is located for the given applied current and magnetic circuit parameters.

Two fundamental laws governing the performance of the electromagnets are the Ampere's and Gauss's laws that involve magnetic field and magnetic flux, respectively. The Ampere's circuit law states that the line integral of the magnetic field intensity over any closed path is equal to the net current enclosed by that path which can be mathematically expressed as [109]:

$$\oint_C \vec{H} \cdot d\vec{l} = I_{enc} \quad (4.29)$$

where  $\vec{H}$  is the vector of magnetic field intensity,  $\vec{dl}$  is an incremental segment of the closed path  $C$ , and  $I_{enc}$  is the total current flowing through the surface that is enclosed by the closed path. In Eq. (4.29), the sign of  $I_{enc}$  is determined by the right-hand rule. On the other hand, the Gauss's law states that over any closed volume, the surface integral of flux density is zero which can be expressed as:

$$\oint_S \vec{B} \cdot \vec{dA} = 0 \quad (4.30)$$

where  $B$  is the magnetic flux density,  $dA$  is an infinitesimal element of the closed surface  $S$  that encloses the volume. Generally, it is a complex problem to solve Eqs. (4.29) and (4.30) because of having different sections in the electromagnet as well as the variation of magnetic parameters. However, in the present electromagnet devices, we only need the magnetic field at the center of the gap where the MRE core layer is located.

As a simplifying assumption, we consider that the magnetic field is constant for specific parts along the center line of the conductive core of each electromagnet (dashed lines in Figure 4.2). As a result, we may write Eq. (4.29) in a discretized form by replacing the integration with a summation which is basically the analog of Kirchhoff's voltages law for magnetic circuits and can be expressed as:

$$\sum H_i l_i = \sum N_i I_i \quad (4.31)$$

where  $H_i$  is the magnetic field in the  $i$ -th portion along the core's center line with constant magnetic flux. The parameters  $l_i$ ,  $N_i$ ,  $I_i$  stand for the length of the portion, number of turns of wire included, and input current to the coil, respectively. Eq. (4.31) states that the sum of magnetomotive force drops ( $H_i l_i$ ) around a closed loop is equal to the sum of the magnetomotive force sources ( $N_i I_i$ ) in that loop.

On the other hand, the Eq. (4.30) states that the sum of the fluxes ( $\hat{\phi}$ ) flowing into any closed volume in the space must be zero. Considering a node (very small volume) in the path of the magnetic flux flow, the sum of the fluxes into or out of the node must be zero, which is the analog of Kirchhoff's current law for magnetic circuits. This can be mathematically described as:

$$\sum \hat{\phi}_i = 0 \quad (4.32)$$

Eqs. (4.31) and (4.32) are used in the analysis of the electromagnets. Here, the development of the analytical circuit model is presented for the H-shaped electromagnet as shown in Figure 4.9.

The path of the magnetic flux which flows through the core sections is shown in the figure with dashed line. There are two closed loops for the H-shaped electromagnet as shown in Figure 4.9. For the closed loop number 1, starting from point  $n$  and moving in counterclockwise direction along the path  $nopqrmn$ , Eq. (4.31) can be expanded over different segments along the path as:

$$N_{c1}I + N_{c2}I + N_{c3}I = H_{core_{op}}l_{op} + H_{core_{pqrm}}l_{pqrm} + H_{core_{mn}}l_{mn} + H_{gap}l_{gap} \quad (4.33)$$

where  $I$  is the input current to the coils, and  $N_{c_i}$  ( $i = 1,2,3,4$ ) is the number of turns of wire in the coil  $C_i$ . Magnetic field ( $H$ ) and length ( $l$ ) for each segment are shown with corresponding subscripts. The magnetic flux density is assumed to be constant at any cross section along the core's centerline, i.e.  $\phi = BA$ . Moreover, at juncture points  $m$  or  $p$ , considering Eq. (4.32), we may write:

$$\hat{\phi}_1 = \hat{\phi}_2 + \hat{\phi}_3 \quad (4.34)$$

in which  $\frac{\hat{\phi}_1}{2} = \hat{\phi}_2 = \hat{\phi}_3$  due to the symmetry of the electromagnet. The same relation exists for the magnetic flux density considering that the cross section is the same all around the closed path.

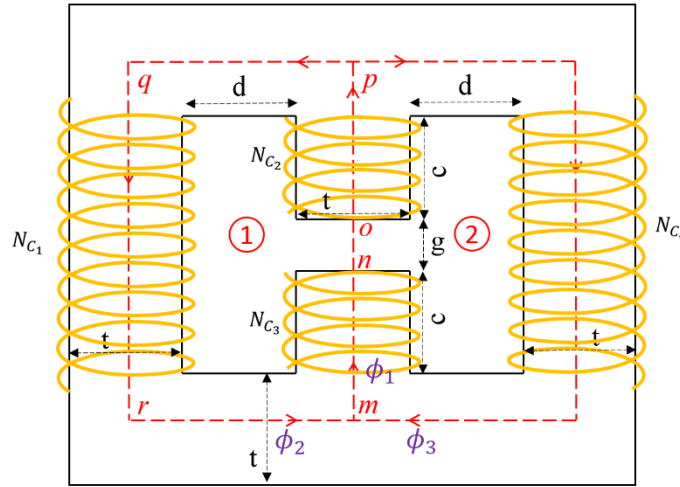


Figure 4.9 The H-shaped electromagnet with the path of magnetic flux penetration discretized by letters for magnetic analysis.

According to the geometrical parameters in Figure 4.2(a) and Figure 4.9, the number of turns of wire in the coils of the electromagnet can be determined as below:

$$N_{c1} = N_{c4} = \frac{d(2c + g)}{2D^2} \quad (4.35)$$

$$N_{c2} = N_{c3} = \frac{cd}{2D^2}$$

where  $c$ ,  $d$ , and  $g$  are geometric parameters shown in Figure 4.9 and  $D$  is the wire diameter. In addition, the total mass of the electromagnet can be formulated as:

$$M_{el} = \frac{\pi}{4} D^2 L_w \rho_w + V_{sc} \rho_{sc} \quad (4.36)$$

where  $\rho_w$  and  $\rho_{sc}$  are densities of the wire and steel core of the electromagnet.  $L_w$  is the length of wire and can be found using the following relation:

$$L_w = \frac{2d(2c+g)}{D^2} (t + t + d) + \frac{2cd}{D^2} (t + t + d) \quad (4.37)$$

and  $V_{sc}$  is the volume of the steel core which can be expressed as:

$$V_{sc} = t((2d + 3t)(2t + 2c + g) - 2d(2c + g) - gt) \quad (4.38)$$

Using Eqs. (4.33) to (4.38), the H-shaped electromagnet can be analyzed to find the magnetic flux density at the center of the gap while the input current to the coil is known.

Here, the results for the developed analytical magnetic circuit model is compared with the obtained results using magnetostatic FE analysis. For this purpose, the H-shaped electromagnet with dimensions of  $c = d = t = 2$  cm and a gap of  $g = 0.5$  cm is considered. Figure 4.10 shows the FE magnetic analysis performed by the FEMM software [110] which is a popular open source FE-based software for magnetic analysis. Here, the input current to the coil is set at 5 A.

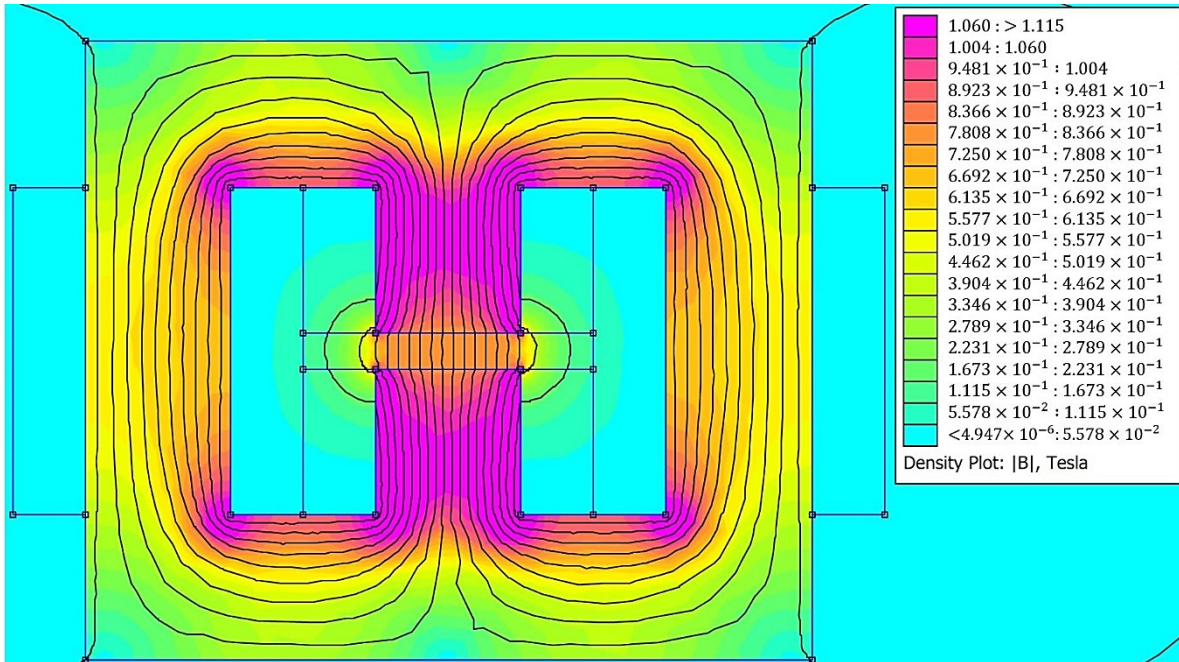


Figure 4.10 Magnetic analysis of the H-shaped electromagnet using FEMM software.

The magnetic flux density at the center of the gap has been evaluated using both analytical and FE models for different applied currents and results are provided in Table 4.1. As it is observed, although the presented analytical formulation does not consider the phenomena of fringing and leakage of the magnetic flux, very good agreement exists between analytical and FE results.

It should be noted that similar analysis can be conducted for the C-shaped and U-shaped electromagnets. The formulation for the C-shaped and U-shaped electromagnets are provided in Appendix B. Similar to the H-shaped electromagnet, negligible error has been observed between analytical and FE magnetic circuit results for the C- and U-shaped electromagnets as provided in Appendix B.

Table 4.1 Comparison of flux density values at the center of the air-gap of the H-shaped electromagnet obtained by analytical magnetic circuit model (Eqs. (4.33) to (4.38)) and FE model.

Input Current (A)	Flux Density (mT)		Error %
	Analytical magnetic circuit model, Eqs. (4.33) to (4.38)	FE analysis	
2.5	399	402	0.77
3	479	482	0.73
3.5	559	563	0.71
4	640	643	0.53
4.5	720	724	0.55
5	801	804	0.37

By combining the developed FE model for the MRE-based sandwich beam (Section 4.4) with the analytical magnetic circuit model of the electromagnet (Eqs. (4.33) to (4.38)), a full model of the MRE-ATVA is obtained. This high-fidelity model will be then utilized to formulate the objective function (natural frequency of the MRE-ATVA) and constraints (total weight of the MRE-ATVA as well as the static deflection and stresses experienced in the sandwich beam due to the weight of the electromagnet) of the multidisciplinary design optimization problem.

#### 4.6 Multidisciplinary Design Optimization of the Proposed MRE-Based ATVAs

Here, a multidisciplinary design optimization problem involving the electromagnet and sandwich beam structure design parameters has been formulated to maximize the frequency bandwidth of the proposed MRE-ATVA under mass, deflection and stress constraints. Due to the symmetry in the proposed configurations for the MRE-ATVA as shown in Figure 4.3, half of the absorber structure which is a cantilever MRE-sandwich beam with one electromagnet installed at

the free end has been considered. The active part of the MRE layer (see Figure 4.7) will be at the free end of the sandwich beam where the electromagnet is installed. The design optimization will be conducted on different design configurations of the electromagnets (H-, C-, and U-shaped) to identify the optimal configuration.

There are several important practical factors in the design optimization of the proposed MRE-ATVA such as weight, operating frequency range, static tip deflection of the cantilever beam, and maximum stress in the elastic layers of the beam. In the proposed optimization problem, the objective is to maximize the frequency bandwidth of the proposed MRE-ATVA under mass, deflection, and stress constraints. In order to realize a light weight MRE-ATVA, the total mass of the device is considered to be less than 700 g. Moreover, to avoid large deflections that may cause geometric nonlinearities, the static tip deflection of the beam is expected to be not more than 10% of the beam length. On the other hand, the maximum stress in the elastic face layers which occurs at the root of the cantilever sandwich beam should not surpass the yield strength of the material. Finally, since the proposed ATVA is considered for vibration control applications in the low frequency ranges, the absorber's frequency in the off-state condition, i.e. the natural frequency under zero current applied to the coils (electromagnets are off), is restricted to be less than 10 Hz.

Figure 4.2 and Figure 4.7 show all the important geometric dimensions in the configuration of the electromagnets and sandwich beam, respectively. The parameters of the core of the electromagnets,  $c$  and  $d$ , and the thickness of the beam layers  $h_t$ ,  $h_c$ ,  $h_b$  are identified as the important design variables in the optimization problem. By having a symmetric sandwich beam with equal thickness in the top and bottom elastic layers, i.e.  $h_t = h_b$ , there will be four design variables ( $c, d, h_t, h_c$ ) in the optimal design problem. It should be noted that the gap of the electromagnet,  $g$ , is occupied by the sandwich beam and thus it would be a dependent parameter ( $g = 2h_t + h_c$ ). The other independent parameters and dimensions are assumed to be fixed. The design optimization problem of the proposed MRE-ATVA can be formally formulated as:

Find the design variables:  $[c, d, h_t, h_c]$

$$\text{To minimize: } \begin{bmatrix} (f)_{B_1=0} \\ (f)_{B_2} \end{bmatrix} \quad (4.39)$$

Subject to the following behavior constraints:

$$M_{total} \leq 700 \text{ g} \quad (4.40)$$

$$(f)_{B_1=0} \leq 10 \text{ Hz} \quad (4.41)$$

$$\text{maximum stress in the elastic layers} \leq 285 \text{ MPa} \quad (4.42)$$

$$\text{static tip deflection} \leq 0.1 L \quad (4.43)$$

and side constraints:

$$[c_{\min}, d_{\min}, h_{t_{\min}}, h_{c_{\min}}] \leq [c, d, h_t, h_c] \leq [c_{\max}, d_{\max}, h_{t_{\max}}, h_{c_{\max}}] \quad (4.44)$$

where  $M_{total}$  is the total mass of the ATVA which is sum of the sandwich beam mass and the electromagnet mass.  $(f)_{B_i}$ ,  $i = 1, 2$  is the natural frequency of the ATVA when flux density of  $B_i$  is applied on the MRE layer by the electromagnet.  $B_1 = 0$  is when the electromagnet is off and  $B_2$  is the flux density that is generated by the electromagnet when maximum allowable current is supplied to the coils. Minimizing the ratio of  $\left[ \frac{(f)_{B_1=0}}{(f)_{B_2}} \right]$  as the objective function, infers the lowest value for  $(f)_{B_1=0}$  and highest value for  $(f)_{B_2}$  which is indeed maximization of the frequency range of the ATVA. The design variables are bounded by reasonable lower and upper limits. In the present study, the values for the lower limits are:  $c_{\min} = d_{\min} = 5 \text{ mm}$ ,  $h_{t_{\min}} = h_{c_{\min}} = 0.5 \text{ mm}$ , and for the upper limits:  $c_{\max} = d_{\max} = 30 \text{ mm}$ ;  $h_{t_{\max}} = h_{c_{\max}} = 3 \text{ mm}$ .

The combination of GA and SQP techniques is utilized in the present study to accurately catch the true optimum solution. The GA is a random-based evolutionary algorithm which can approximately identify the global optimum solution. On the other hand, SQP is a powerful derivative-based algorithm developed for constrained nonlinear optimization problems. Depending on the starting initial point, SQP can accurately identify the nearest local optimum solution, without any mechanism to search for global solution. In this study, the merits of both algorithms have been exploited in which the GA is first run to identify the near global optimum solution and then the optimum solution from GA is fed into the SQP algorithm as the initial point to capture accurately the global optimum solution.

The complete model of the ATVA which consists of the FE model of the sandwich beam and magnetic analysis of the electromagnet is used to develop two MATLAB<sup>®</sup> functions; one to calculate the objective function defined in Eq. (4.39) and the other includes constraints defined in Eqs. (4.40) to (4.44). The optimization problem for each configuration of the electromagnet is first solved by the genetic algorithm using the GA optimization platform in MATLAB<sup>®</sup>. Then the optimal result of GA is used as the initial point to run the “Fmincon” command with SQP algorithm using MATLAB<sup>®</sup>.

## 4.7 Optimization Results and Discussion

In this section, optimum results for different configurations of the MRE-ATVA are presented and compared. In all cases, the length and width of the three-layer sandwich beam is fixed to be  $L = 15$  cm and  $w = 2$  cm, respectively. Edge size of the square cross section of the conductor core is set at  $t = 2$  cm for all the electromagnet designs. Maximum applied current is considered to be 5 A. The material properties for different parts of the ATVA and their mechanical and magnetic properties were introduced in Section 4.3.

To demonstrate the non-convexity nature of the problem and existence of multiple local optimum solutions, SQP optimizer has been first executed for MRE-ATVA with H-shaped electromagnet using different initial points. Figure 4.11 shows iteration history (objective function versus number of iterations). The three initial points have been selected from the beginning, middle, and end of the design variables' ranges. As it can be realized, starting from different initial points, SQP method identifies different local optimum solutions.

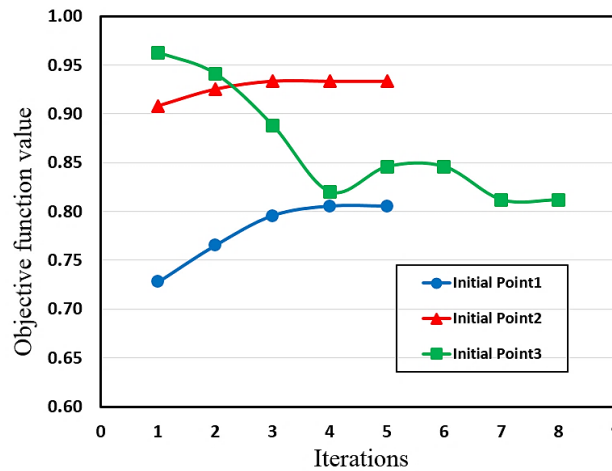


Figure 4.11 Performance of the SQP method when starting from different initial points.

On the other hand, executing GA which uses random population of points, has resulted to optimum solutions which are near to the global optimum solution. However, once different optimum solutions from GA is used as initial points for SQP algorithm, a unique global optimum solution is obtained.

Table 4.2 shows the optimization results for different configurations of the proposed MRE-ATVA obtained using combined GA and SQP methods. The optimal value of the design variables is reported on the top part of the table which are used to calculate the corresponding performance



of the optimal MRE-ATVAs provided at the bottom of the table. Results suggest that the optimal MRE-ATVA with U-shaped electromagnet presents 42.1% frequency increase while the C-shaped and H-shaped types show 28% and 24% increase in the frequency, respectively. Therefore, the ATVA having U-shaped electromagnet shows the maximum frequency range in comparison with the other configurations where the natural frequency of the absorber could vary from 5.73 Hz to 8.14 Hz. Besides, the optimal C-shaped design shows the minimum mass of 423 g while the U-shaped and H-shaped designs give a mass of 596 g and 643 g, respectively.

The reason behind higher frequency bandwidth of the optimal U-shaped configuration over the C- and H-shaped designs might be due to wider interaction surface of the U-shaped electromagnet with the MRE core layer. This type of electromagnet, due to its U-shaped structure, has two contact surfaces on its poles with the sandwich beam where the magnetic field flows through the MRE core layer. Therefore, the MRE layer being activated in a wider span of the sandwich beam which will cause higher MR effect in the system and finally greater change in the natural frequency. Moreover, it should be noted that the constraint of maximum stress in the steel face layers at the root of the beam is an active constraint for the optimal design of all the three ATVA configurations presented in Table 4.2. It is seen from the results of Table 4.2 that the optimal ATVA with U-shaped electromagnet, thanks to its location on the beam with a center of mass closer to the beam root, allows for thicker MRE layer (higher  $h_c$ ) before reaching the limit of maximum stress. A thicker MRE core layer brings higher MR effect in the system which results in greater change in the natural frequency.

Table 4.2 Optimization results of the MRE-ATVA with the three different electromagnets.

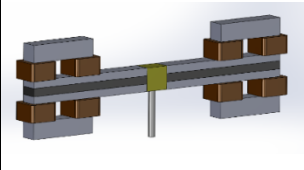
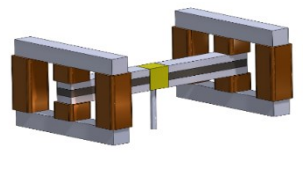
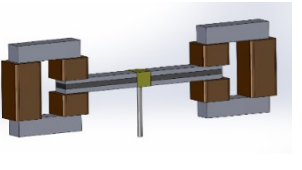
		ATVA with U-shaped electromagnet	ATVA with H-shaped electromagnet	ATVA with C-shaped electromagnet
				
Optimal values (mm)	$h_t = h_b$	0.85	0.95	0.79
	$h_c$	1.10	0.50	0.50
	$c$	5.00	5.00	5.00
	$d$	18.00	5.00	5.00
ATVA performance	Total Mass (g)	596.0	643.0	423.0
	Frequency Range [ $f_1 - f_2$ ] (Hz)	[5.73 – 8.14]	[5.38 – 6.68]	[5.23 – 6.69]
	Frequency Shift $\Delta f$ (Hz)	2.41	1.30	1.46
	Frequency Shift $\frac{\Delta f}{f_1}$ (%)	42.1	24.0	28.0

Figure 4.12 illustrates the optimal frequency shift for the MRE-ATVAs with different values of the input current to the coils of the electromagnets. As it can be realized, on the one hand, the optimal ATVA with U-shaped electromagnet has the highest frequency shift for all current inputs compared with those of C- and H-shaped designs. On the other hand, comparison of the C- and H-shaped configurations shows that they have a similar performance at the low current values, whereas the C-shaped design precedes the H-shaped configuration for the current values more than 2.5 A. For all three configurations, the slope of the graphs is greater at small current values and

gradually decreases with an increase of the input current which can be attributed to the magnetic saturation of the MRE at high values of magnetic excitation, as discussed in Section 4.3.

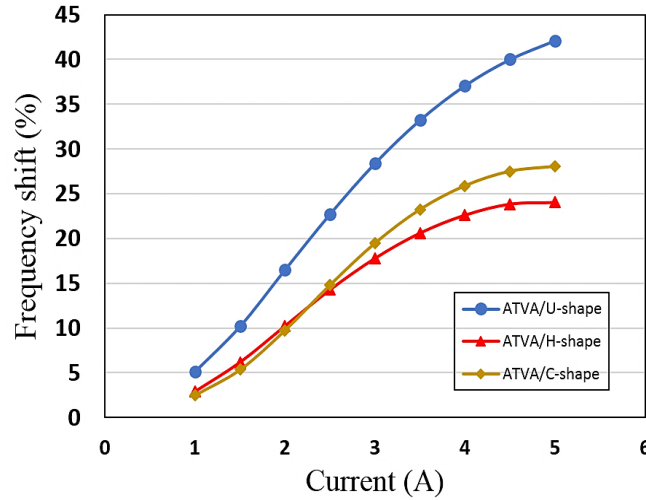


Figure 4.12 Frequency shift versus input current for the three optimal MRE-ATVAs.

#### 4.8 Conclusions

In this chapter, a comprehensive design optimization process for a novel MRE-ATVA is investigated. The proposed MRE-ATVA consists of a three-layer sandwich beam with MRE in the core layer and two electromagnets placed on both ends of the beam to provide the required magnetic field and to serve as the active mass of the absorbers. Three potential designs for the electromagnets are investigated in the optimization problem including electromagnets with U-, H-, and C-shaped designs. A FE model of the sandwich beam is presented and validated with the analytical solution from the literature. Magnetic analysis of the electromagnets is performed using a developed formulation based on the Ampere’s circuital law and Gauss’s law. The results of the magnetic analysis of the electromagnets are validated with the simulation results using a FE magnetic analysis. By combining the FE model of the sandwich beam and the magnetic model of the electromagnets, a high-fidelity model of the proposed MRE-ATVAs is constructed, which is subsequently employed to calculate the natural frequency of the absorber and constraint functions.

Finally, a multidisciplinary design optimization problem is formulated to identify the optimal values of the considered geometric structural and magnetic design parameters to maximize the frequency range of the proposed MRE-ATVAs. A combined GA and SQP algorithm was used to find accurate global optimal solutions of the proposed MRE-ATVAs with three different electromagnet configurations. The results suggest that the optimal MRE-ATVA with U-shaped electromagnet can provide the highest frequency shift (42%) in the range of 5.73 to 8.14 Hz. The

C- and H-shaped configurations present 28% and 24% increase in the natural frequency, respectively. The optimal ATVAs are all lightweight as their masses are below 700 g. In addition, the performance of the optimized MRE-ATVA at different input currents is investigated. The results show that the optimal MRE-ATVA with U-shaped electromagnet provides the highest frequency shift irrespective of the applied current. Such optimized lightweight MRE-ATVAs with significant frequency shift in the low frequency range pave the way for realization of the compact practical adaptive vibration absorbers that are very effective and reliable for vibration and noise control applications.

## CHAPTER 5

### CONTRIBUTIONS, CONCLUSIONS AND RECOMMENDATIONS FOR FUTURE WORKS

#### 5.1 Major Contributions and Achievements

The present research dissertation provided a comprehensive investigation on the fabrication, characterization, and microstructure-based modeling of MREs for both of quasi-static and dynamic loading conditions. In addition, the application of MREs in adaptive vibration absorption was studied by presenting the design optimization of a novel sandwich beam-based ATVA treated with MRE. The major contributions of this research dissertation over the current state of MRE knowledge are summarized below:

1. A microstructure-based model was developed for predicting the quasi-static magneto-elastic properties of the MREs. The model considers the magnetic interaction between filler particles in the material by assuming ideal distribution of magnetizable particles according to lattice configurations. For the first time, a complete set of different types of lattice models were considered to represent the distribution of magnetic fillers in the matrix. For the isotropic MREs, seven lattices, including SC, BCC, FCC, ECC, BECC, FECC, and BFECC lattices, were considered. For the anisotropic MREs, chain-like structure of particles was used as idealized dispersion of fillers. Both elastic and magnetic parts of the model were formulated using an energy approach and the shear modulus was obtained for the various lattices in terms of magnetic flux density, volume fraction of particles, and material properties. The performance of the proposed lattices were explained in detailed physical and mathematical discussion. The variation in MREs properties under the applied magnetic field was well clarified based on magnetic interaction between particles in the network. The results of shear modulus from the proposed microstructure model were validated with the experimental data measured using in-house fabricated MRE samples. In addition, the efficiency of the lattices were evaluated quantitatively by comparing their performance in predicting the experimental results.

2. A microstructure modeling approach was also developed to investigate the dynamic magneto-viscoelastic properties of the MREs. The Langevin dynamic of particles' motion were formulated using a Lagrange's approach and solved to obtain the field-dependent relaxation times of the particles distributed in a cubic and chain-like network for both isotropic and anisotropic MREs, respectively. Particles in the network were connected with springs representing the elasticity of the host matrix and each particle has a viscous constant providing the damping effects associated with particles' motion and that of the material. After deriving the equations of motion of particles and finding the relaxation times, a dipole magnetic saturation model was introduced into the model to relate the eigenvalues and relaxation times to the magnetic flux density which is directly measurable in practice. The frequency- and magnetic field-dependent storage and loss moduli of the MRE material were extracted from the relaxation modulus. To validate the dynamic model, first, isotropic and anisotropic MRE samples with different volume fraction of iron particles have been fabricated and then experimentally characterized under wide range of excitation frequencies and external magnetic flux densities using an advanced rheometer device integrated with an electromagnet unit. The material model parameters were estimated using the experimental data and finally, the theoretical results based on the proposed model were compared with empirical data which unveiled the accuracy of the model. The proposed dynamic microstructure-based model advances the existing coarse-grained network models in the literature.

3. A novel MRE-cored sandwich beam type ATVA is designed and optimized for maximum frequency bandwidth. The proposed MRE-ATVA includes flexible and light weight MRE-based sandwich beam with electromagnets installed on beam ends. The role of electromagnets is twofold: providing the require magnetic field to activate the MRE core layer and also serving as the active mass of the absorber. Three different configurations were proposed for the electromagnets. FE model of the sandwich beam, and the mathematical formulation for magnetic analysis of the electromagnets were established and combined to achieve a comprehensive model for the MRE-ATVA able to capture variation in the natural frequency of the beam under change in the magnetic field and other parameters of the absorber. Thereafter, a multidisciplinary optimal design problem which considers both the structural geometry and electromagnet

parameters as design variables, was formulated aiming at maximizing the frequency range of the absorber, while respecting constraints on the total mass, static deflection, and maximum stress in the beam. To accurately identify the optimal design, the optimization problem is solved using a combination of GA and SQP methods. Finally, the performance of the identified optimal designs for the proposed MRE-ATVAs were compared and discussed.

## 5.2 Major Conclusions

The major conclusions extracted from the results of this research dissertation are summarized below:

- MRE samples fabricated in the lab using spherical shape carbonyl iron powders and low viscous silicone rubber were stable and appropriate for shear mode characterization with rheometer. The microstructure images exhibited well dispersion of particles in the medium.
- Fabrication of samples with high volume fraction of particles, particularly beyond 40%, becomes challenging due to the enhanced agglomeration of filler particles.
- Under quasi-static shear strain and applied magnetic field, the stiffness of MREs have increased which was significantly pronounced for samples with higher volume fraction of particles. For instance, an MRE sample with  $\phi = 5\%$  provided around 70% increase in the elastic modulus while a sample with  $\phi = 40\%$  improved the shear modulus by around 3000 % under applied magnetic flux density varying from 0 to 1 T.
- Anisotropic MRE samples have shown superior increase in the shear modulus compared to the isotropic MREs with similar particle participation due to the chain-like distribution of particles in the structure. However, the anisotropic samples become magnetically saturated at lower magnetic inductions.
- Increasing the level of applied magnetic flux density and volume fraction of iron particles also enhances the nonlinearity of the elastic response of the MREs.
- Magnetic saturation of MRE samples with higher particle population occurs at higher magnetic flux densities in comparison with samples having lower particle content.

- Regarding the elastic response of the MRE samples in the absence of magnetic induction, the two-term  $I_1$ -based model showed superior performance in predicting the nonlinear stress-strain response of MREs compared to the Neo-Hookean and one-term Ogden models.
- Not all the idealized distribution of particles considered in the microstructure-based model showed acceptable performance in predicting the variation of elastic shear modulus of the isotropic MRE materials in terms of magnetic flux density.
- Seven lattices were investigated to represent the isotropic distribution of particles in the material including: SC, BCC, FCC, ECC, BECC, FECC, and BFECC. For the anisotropic MREs, ideal chain-like structure of particles was used in the model.
- Among the lattices, the BCC and FCC have shown decrease in the elastic shear modulus by the magnetic field which is in contradiction with experimental results.
- Variation in the properties of MREs under magnetic field is explained from a microstructure point of view by studying the magnetic interaction between particles in the network. Differences in the performance of the lattices were also explained on the basis of the magnetic interaction between particles.
- Among the considered lattice types, only the ECC lattice which also showed the maximum MR effect was able to predict the variation of shear modulus of MRE samples versus external magnetic flux density for all samples with various volume fraction of particles. Indeed, other lattices such as the SC lattice cannot represent truly the distribution of particles at high volume fractions such as  $\phi = 40\%$ . However, the ECC lattice is a better idealized representation of particles distribution at high volume fractions and could better predict the shear modulus test data.
- By calculating the RMSE index for all the lattices, the relative performance of the lattices in predicting the experimental data of the fabricated MRE samples was quantitatively evaluated and compared.
- Regarding dynamic magneto-mechanical properties of MREs, experimental characterization and microstructural modeling of linear viscoelastic response of isotropic and anisotropic MREs were performed.
- In dynamic situation, a microstructure-based model was derived based on cubic network of particles for isotropic MREs and chain-like structure of particles for anisotropic MREs.



For this purpose, particles were connected with elastic springs and a friction coefficient was assigned to the motion of each particle.

- Lagrange's approach was used to derive the dynamic equation of motion associated with the motion of particles in the network around their equilibrium positions. After linearization and transforming from Cartesian coordinates to normal coordinates, equations of motion were solved to obtain eigenvalues (inverse relaxation times) in terms of magnetic flux density.
- The behavior of normal modes relaxation spectrum illustrated splitting of the spectrum under application of magnetic field into two branches. The eigenvalues associating with the particle motions along the direction of external magnetic field decreased (increase of relaxation time) and those associating with the motions normal to the field direction increased (decrease of relaxation time). Both the external magnetic field and volume fraction of particles intensified the breaking level of relaxation spectrum.
- Variation in eigenvalues with respect to the applied magnetic field was explained considering that the relaxation time is inversely related to the effective stiffness along a direction.
- Anisotropic MREs exhibited higher zero-field eigenvalue (lower relaxation time) and also greater splitting of relaxation spectrum under magnetic field compared to the isotropic MREs. This suggests that as the particles arrangement moves toward chains, the eigenvalues (relaxation times) become more sensitive to the magnetic field.
- At high external magnetic field, the model may result in negative eigenvalues and subsequently negative relaxation time which shows the instability of the particle network. A parameter was introduced named critical magnetic flux density, at which the eigenvalues become negative. The critical magnetic flux density was calculated to show the critical threshold of the model.
- Considering a situation where an MRE material is under oscillatory shear deformation and magnetic field is applied normal to the shearing deformation, relations for storage and loss moduli were derived from the relaxation modulus by using the information of relaxation time spectrum.

- The few tuning parameters of the proposed model were identified by minimizing the error between theoretical results and experiment data taken from real isotropic and anisotropic MRE samples fabricated in the lab.
- The storage and loss moduli of the MRE samples showed increasing behavior with magnetic flux density and saturation at high magnetic fields. The increase in the dynamic moduli was improved for higher volume fraction of particles and for anisotropic chain-like dispersion of particles in the material.
- The developed microstructure-based model showed a remarkable performance in predicting the experiment data of storage and loss moduli in a wide range of excitation frequency ranging from 2 Hz to 100 Hz and magnetic flux density varying up to 1 T. Also, the model was successful in predicting the magnetic saturation of the MRE materials.
- A sandwich beam with MRE core layer having two electromagnets installed on both ends was designed as an MRE-ATVA. The electromagnets provided the required magnetic field and also served as the active mass of the absorbers. Three potential designs including electromagnets with U-, H-, and C-shaped designs were considered.
- FE model of the sandwich beam and magnetic analysis of the electromagnets were developed and validated by simulation data and available results in the literature. A comprehensive model of the MRE-ATVA was developed by combining the aforementioned models of the beam and electromagnets.
- A multidisciplinary design optimization problem using combined GA and SQP algorithm was finally formulated to identify the optimal values of the considered geometric structural and magnetic design parameters to maximize the frequency range of the proposed MRE-ATVA. Constraints of mass, deflection, size and stress were applied in the optimization problem.
- The optimal MRE-ATVA with U-shaped electromagnet provided the highest frequency shift of 42% in the range of 5.73 Hz to 8.14 Hz. The C- and H-shaped configurations presented 28% and 24% increase in the natural frequency varying in the range of 5.23 Hz to 6.69 Hz and 5.38 Hz to 6.68, respectively.
- Regarding the optimal frequency shift of the MRE-ATVAs in terms of input current to the coils of the electromagnets, the optimal ATVA having U-shaped electromagnet showed the highest frequency shift for all current inputs. On the other hand, the C- and H-shaped

configurations showed similar frequency shift at the low current values, whereas for the current values more than 2.5 A, the C-shaped design surpassed the H-shaped configuration. Magnetic saturation of the MRE at high values of magnetic excitation was observed from the variation of absorber's frequency shift at high input currents.

### **5.3 Recommendations for the future works**

In this dissertation, magneto-mechanical properties of smart MRE materials were systematically investigated through performing experiments as well as theoretical modeling in both static and dynamic situations. The application of MRE in adaptive vibration absorption was also illustrated by proposing design optimization of a sandwich beam type adaptive tuned vibration absorber treated with MRE material. The developed experiments, models, analysis and design optimization formulations provide a unique platform to fundamentally analyze these emerging materials and to design the next generation of lightweight, semi-active vibration absorbers for optimal vibration suppression. Although the developed analytical, computational and experimental techniques have significantly advanced the state of the art in the field of smart MREs, nevertheless, the following interesting aspects which are natural extension of the current work have been identified:

- i. The developed quasi-static and dynamic microstructure-based models can be extended to analyze the MRE properties in tension-compression modes.
- ii. The different lattice types such as ECC lattice that were used in the quasi-static model of MRE can be also employed in the dynamic model. In this case, particles' equations of motion have to be updated to address the new configuration of particles in the network.
- iii. Regarding the inconsistencies occurred in predicting the loss modulus of anisotropic MREs at high magnetic field and low frequencies (as observed in Figure 3.11 and Figure 3.12) more research can be done to find the damping mechanisms of the MREs and how to incorporate those mechanisms into the developed microstructure-based model.
- iv. In the modeling approaches of the current research, spherical filler particle with identical diameter were used which is reasonable to represent average diameter of the fabricated filler particles. However, in real MRE samples usually particles exist in a specific narrow range of diameters. On the other hand, during fabrication of MREs, some aggregates of particles may form in the matrix as can be observed from microstructural images (Figure

- 3.7). Future research can be done to investigate the effect of randomness in particle size and filler aggregations on the magnetic and mechanical properties of MREs as initiated by a few researchers in the past [61], [111]–[113].
- v. Semi-active control strategies based on different control techniques such as observer-based linear quadratic regulator (LQR), optimal control or fuzzy logic-based control can be developed to enhance vibration damping of the optimized MRE-ATVA in a closed-loop system under different loading conditions.
  - vi. The optimal MRE-ATVA can be prototyped to be implemented in a hardware-in-the-loop system to evaluate its performance in mitigating the vibrations of a main system.

## References

- [1] R. Ahamed, S.-B. Choi, and M. M. Ferdaus, “A state of art on magneto-rheological materials and their potential applications,” *J. Intell. Mater. Syst. Struct.*, vol. 29, no. 10, pp. 2051–2095, 2018.
- [2] A. Hooshiar, A. Alkhalaf, and J. Dargahi, “Development and assessment of a stiffness display system for minimally invasive surgery based on smart magneto-rheological elastomers,” *Mater. Sci. Eng. C*, vol. 108, p. 110409, 2020.
- [3] T. Xu, J. Zhang, M. Salehizadeh, O. Onaizah, and E. Diller, “Millimeter-scale flexible robots with programmable three-dimensional magnetization and motions,” *Sci. Robot.*, vol. 4, no. 29, 2019.
- [4] H. Frahm, “Device for damping vibrations of bodies,” Apr. 18, 1911.
- [5] J. Q. Sun, M. R. Jolly, and M. A. Norris, “Passive, adaptive and active tuned vibration absorbers—a survey,” 1995.
- [6] J. M. Ginder, W. F. Schlotter, and M. E. Nichols, “Magnetorheological elastomers in tunable vibration absorbers,” in *Smart structures and materials 2001: damping and isolation*, 2001, vol. 4331, pp. 103–110.
- [7] M. Behrooz, X. Wang, and F. Gordaninejad, “Performance of a new magnetorheological elastomer isolation system,” *Smart Mater. Struct.*, vol. 23, no. 4, p. 045014, 2014.
- [8] B. Nayak, S. K. Dwivedy, and K. Murthy, “Dynamic analysis of magnetorheological elastomer-based sandwich beam with conductive skins under various boundary conditions,” *J. Sound Vib.*, vol. 330, no. 9, pp. 1837–1859, 2011.
- [9] A. Dargahi, R. Sedaghati, and S. Rakheja, “On the properties of magnetorheological elastomers in shear mode: design, fabrication and characterization,” *Compos. Part B Eng.*, vol. 159, pp. 269–283, 2019.
- [10] G. Shi, W. Wang, H. Lu, G. Wang, F. Yang, and X. Rui, “Study of crosslink structure and dynamic mechanical properties of magnetorheological elastomer: effect of vulcanization system,” *J. Intell. Mater. Syst. Struct.*, vol. 30, no. 8, pp. 1189–1199, 2019.

- [11] G. Riesgo, J. Carrizo, L. Elbaile, R. D. Crespo, R. Sepúlveda, and J. A. García, “Magnetostrictive properties of FeAl/polyester and FeAl/silicone composites,” *Mater. Sci. Eng. B*, vol. 215, pp. 56–63, 2017.
- [12] J. Sutrisno, A. Purwanto, and S. A. Mazlan, “Recent progress on magnetorheological solids: materials, fabrication, testing, and applications,” *Adv. Eng. Mater.*, vol. 17, no. 5, pp. 563–597, 2015.
- [13] X. Lu *et al.*, “Mechanical and structural investigation of isotropic and anisotropic thermoplastic magnetorheological elastomer composites based on poly (styrene-*b*-ethylene-co-butylene-*b*-styrene)(SEBS),” *Rheol. Acta*, vol. 51, no. 1, pp. 37–50, 2012.
- [14] I. Bica and E. M. Anitas, “Magnetic field intensity and  $\gamma$ -Fe<sub>2</sub>O<sub>3</sub> concentration effects on the dielectric properties of magnetodielectric tissues,” *Mater. Sci. Eng. B*, vol. 236, pp. 125–131, 2018.
- [15] Z. Varga, G. Filipcsei, and M. Zrínyi, “Magnetic field sensitive functional elastomers with tuneable elastic modulus,” *Polymer*, vol. 47, no. 1, pp. 227–233, 2006.
- [16] H. Meharthaj, S. M. Sivakumar, and A. Arockiarajan, “Significance of particle size on the improved performance of magnetorheological gels,” *J. Magn. Magn. Mater.*, vol. 490, p. 165483, 2019.
- [17] M. Arana, P. G. Bercoff, and S. E. Jacobo, “Thermomagnetic characterization of organic-based ferrofluids prepared with Ni ferrite nanoparticles,” *Mater. Sci. Eng. B*, vol. 215, pp. 1–8, 2017.
- [18] M. A. Khanouki, R. Sedaghati, and M. Hemmatian, “Experimental characterization and microscale modeling of isotropic and anisotropic magnetorheological elastomers,” *Compos. Part B Eng.*, vol. 176, p. 107311, 2019.
- [19] A. Bellelli and A. Spaggiari, “Magneto-mechanical characterization of magnetorheological elastomers,” *J. Intell. Mater. Syst. Struct.*, vol. 30, no. 17, pp. 2534–2543, 2019.
- [20] S. Samal, M. Kolinova, and I. Blanco, “The magneto-mechanical behavior of active components in iron-elastomer composite,” *J. Compos. Sci.*, vol. 2, no. 3, p. 54, 2018.
- [21] A. K. Bastola, M. Paudel, and L. Li, “Dot-patterned hybrid magnetorheological elastomer developed by 3D printing,” *J. Magn. Magn. Mater.*, vol. 494, p. 165825, 2020.

- [22] A. K. Bastola, M. Paudel, and L. Li, "Development of hybrid magnetorheological elastomers by 3D printing," *Polymer*, vol. 149, pp. 213–228, 2018.
- [23] A. K. Bastola, V. T. Hoang, and L. Li, "A novel hybrid magnetorheological elastomer developed by 3D printing," *Mater. Des.*, vol. 114, pp. 391–397, 2017.
- [24] M. Norouzi, S. M. Sajjadi Alehashem, H. Vatandoost, Y. Q. Ni, and M. M. Shahmardan, "A new approach for modeling of magnetorheological elastomers," *J. Intell. Mater. Syst. Struct.*, vol. 27, no. 8, pp. 1121–1135, 2016.
- [25] B. L. Walter, J.-P. Pelteret, J. Kaschta, D. W. Schubert, and P. Steinmann, "Preparation of magnetorheological elastomers and their slip-free characterization by means of parallel-plate rotational rheometry," *Smart Mater. Struct.*, vol. 26, no. 8, p. 085004, 2017.
- [26] H. Vatandoost, M. Hemmatian, R. Sedaghati, and S. Rakheja, "Dynamic characterization of isotropic and anisotropic magnetorheological elastomers in the oscillatory squeeze mode superimposed on large static pre-strain," *Compos. Part B Eng.*, vol. 182, p. 107648, 2020.
- [27] W. H. Li, Y. Zhou, and T. F. Tian, "Viscoelastic properties of MR elastomers under harmonic loading," *Rheol. Acta*, vol. 49, no. 7, pp. 733–740, 2010.
- [28] C. Y. Yang, J. Fu, M. Yu, X. Zheng, and B. X. Ju, "A new magnetorheological elastomer isolator in shear–compression mixed mode," *J. Intell. Mater. Syst. Struct.*, vol. 26, no. 10, pp. 1290–1300, 2015.
- [29] G. Schubert and P. Harrison, "Large-strain behaviour of magneto-rheological elastomers tested under uniaxial compression and tension, and pure shear deformations," *Polym. Test.*, vol. 42, pp. 122–134, 2015.
- [30] L. Bodelot, J.-P. Voropaieff, and T. Pössinger, "Experimental investigation of the coupled magneto-mechanical response in magnetorheological elastomers," *Exp. Mech.*, vol. 58, no. 2, pp. 207–221, 2018.
- [31] Y. Shen, M. F. Golnaraghi, and G. R. Heppler, "Experimental research and modeling of magnetorheological elastomers," *J. Intell. Mater. Syst. Struct.*, vol. 15, no. 1, pp. 27–35, 2004.
- [32] X. L. Gong, X. Z. Zhang, and P. Q. Zhang, "Fabrication and characterization of isotropic magnetorheological elastomers," *Polym. Test.*, vol. 24, no. 5, pp. 669–676, 2005.

- [33] J. Kaleta, M. Królewicz, and D. Lewandowski, “Magnetomechanical properties of anisotropic and isotropic magnetorheological composites with thermoplastic elastomer matrices,” *Smart Mater. Struct.*, vol. 20, no. 8, p. 085006, 2011.
- [34] I. Agirre-Olabide, J. Berasategui, M. J. Elejabarrieta, and M. M. Bou-Ali, “Characterization of the linear viscoelastic region of magnetorheological elastomers,” *J. Intell. Mater. Syst. Struct.*, vol. 25, no. 16, pp. 2074–2081, 2014.
- [35] E. Coquelle, G. Bossis, D. Szabo, and F. Giulieri, “Micromechanical analysis of an elastomer filled with particles organized in chain-like structure,” *J. Mater. Sci.*, vol. 41, no. 18, pp. 5941–5953, 2006.
- [36] Y. Li, J. Li, W. Li, and H. Du, “A state-of-the-art review on magnetorheological elastomer devices,” *Smart Mater. Struct.*, vol. 23, no. 12, p. 123001, 2014.
- [37] J. M. Ginder, M. E. Nichols, L. D. Elie, and J. L. Tardiff, “Magnetorheological elastomers: properties and applications,” in *Smart Structures and Materials 1999: Smart Materials Technologies*, 1999, vol. 3675, pp. 131–138.
- [38] S. Chen, X. Wang, Z. Zhang, W. Mu, and R. Li, “Optimal design of laminated-MRE bearings with multi-scale model,” *Smart Mater. Struct.*, vol. 25, no. 10, p. 105037, 2016.
- [39] M. A. Cantera, M. Behrooz, R. F. Gibson, and F. Gordaninejad, “Modeling of magneto-mechanical response of magnetorheological elastomers (MRE) and MRE-based systems: a review,” *Smart Mater. Struct.*, vol. 26, no. 2, p. 023001, 2017.
- [40] E. Galipeau and P. P. Castañeda, “A finite-strain constitutive model for magnetorheological elastomers: magnetic torques and fiber rotations,” *J. Mech. Phys. Solids*, vol. 61, no. 4, pp. 1065–1090, 2013.
- [41] K. Danas, S. V. Kankanala, and N. Triantafyllidis, “Experiments and modeling of iron-particle-filled magnetorheological elastomers,” *J. Mech. Phys. Solids*, vol. 60, no. 1, pp. 120–138, 2012.
- [42] I. A. Brigadnov and A. Dorfmann, “Mathematical modeling of magneto-sensitive elastomers,” *Int. J. Solids Struct.*, vol. 40, no. 18, pp. 4659–4674, 2003.
- [43] A. Dorfmann and R. W. Ogden, “Magnetoelastic modelling of elastomers,” *Eur. J. Mech.-ASolids*, vol. 22, no. 4, pp. 497–507, 2003.
- [44] P. Saxena, M. Hossain, and P. Steinmann, “A theory of finite deformation magneto-viscoelasticity,” *Int. J. Solids Struct.*, vol. 50, no. 24, pp. 3886–3897, 2013.



- [45] L. Borcea and O. Bruno, “On the magneto-elastic properties of elastomer–ferromagnet composites,” *J. Mech. Phys. Solids*, vol. 49, no. 12, pp. 2877–2919, 2001.
- [46] A. Beheshti, R. Sedaghati, and S. Rakheja, “Finite deformation analysis of isotropic magnetoactive elastomers,” *Contin. Mech. Thermodyn.*, pp. 1–16, 2020.
- [47] A. Beheshti, R. Sedaghati, and S. Rakheja, “Transversely isotropic magnetoactive elastomers: theory and experiments,” *Arch. Appl. Mech.*, pp. 1–18, 2020.
- [48] H. Vatandoost, M. Norouzi, S. M. S. Alehashem, and S. K. Smoukov, “A novel phenomenological model for dynamic behavior of magnetorheological elastomers in tension–compression mode,” *Smart Mater. Struct.*, vol. 26, no. 6, p. 065011, 2017.
- [49] I. Agirre-Olabide, A. Lion, and M. J. Elejabarrieta, “A new three-dimensional magneto-viscoelastic model for isotropic magnetorheological elastomers,” *Smart Mater. Struct.*, vol. 26, no. 3, p. 035021, 2017.
- [50] L. Chen and S. Jerrams, “A rheological model of the dynamic behavior of magnetorheological elastomers,” *J. Appl. Phys.*, vol. 110, no. 1, p. 013513, 2011.
- [51] M. R. Jolly, J. D. Carlson, B. C. Muñoz, and T. A. Bullions, “The magnetoviscoelastic response of elastomer composites consisting of ferrous particles embedded in a polymer matrix,” *J. Intell. Mater. Syst. Struct.*, vol. 7, no. 6, pp. 613–622, 1996.
- [52] M. R. Jolly, J. D. Carlson, and B. C. Munoz, “A model of the behaviour of magnetorheological materials,” *Smart Mater. Struct.*, vol. 5, no. 5, p. 607, 1996.
- [53] J. M. Ginder and L. C. Davis, “Shear stresses in magnetorheological fluids: role of magnetic saturation,” *Appl. Phys. Lett.*, vol. 65, no. 26, pp. 3410–3412, 1994.
- [54] J. M. Ginder, L. C. Davis, and L. D. Elie, “Rheology of magnetorheological fluids: models and measurements,” *Int. J. Mod. Phys. B*, vol. 10, no. 23n24, pp. 3293–3303, 1996.
- [55] L. C. Davis, “Model of magnetorheological elastomers,” *J. Appl. Phys.*, vol. 85, no. 6, pp. 3348–3351, 1999.
- [56] S. Sun *et al.*, “An adaptive tuned vibration absorber based on multilayered MR elastomers,” *Smart Mater. Struct.*, vol. 24, no. 4, p. 045045, 2015.
- [57] H. Deng, X. Gong, and L. Wang, “Development of an adaptive tuned vibration absorber with magnetorheological elastomer,” *Smart Mater. Struct.*, vol. 15, no. 5, p. N111, 2006.

- [58] Y. Zhu, X. Gong, H. Dang, X. Zhang, and P. Zhang, “Numerical analysis on magnetic-induced shear modulus of magnetorheological elastomers based on multi-chain model,” *Chin. J. Chem. Phys.*, vol. 19, no. 2, pp. 126–130, 2006.
- [59] E. Allahyarov, H. Löwen, and L. Zhu, “A simulation study of the electrostriction effects in dielectric elastomer composites containing polarizable inclusions with different spatial distributions,” *Phys. Chem. Chem. Phys.*, vol. 17, no. 48, pp. 32479–32497, 2015.
- [60] S. W. Chen, R. Li, Z. Zhang, and X. J. Wang, “Micromechanical analysis on tensile modulus of structured magneto-rheological elastomer,” *Smart Mater. Struct.*, vol. 25, no. 3, p. 035001, 2016.
- [61] P. Metsch, K. A. Kalina, C. Spieler, and M. Kästner, “A numerical study on magnetostrictive phenomena in magnetorheological elastomers,” *Comput. Mater. Sci.*, vol. 124, pp. 364–374, 2016.
- [62] D. Ivaneyko, V. Toshchevnikov, M. Saphiannikova, and G. Heinrich, “Effects of particle distribution on mechanical properties of magneto-sensitive elastomers in a homogeneous magnetic field,” *ArXiv Prepr. ArXiv12101401*, 2012.
- [63] D. Ivaneyko, V. P. Toshchevnikov, M. Saphiannikova, and G. Heinrich, “Magneto-sensitive Elastomers in a Homogeneous Magnetic Field: A Regular Rectangular Lattice Model,” *Macromol. Theory Simul.*, vol. 20, no. 6, pp. 411–424, 2011.
- [64] D. Ivaneyko, V. Toshchevnikov, D. Borin, M. Saphiannikova, and G. Heinrich, “Mechanical Properties of Magneto-Sensitive Elastomers in a Homogeneous Magnetic Field: Theory and Experiment,” in *Macromolecular Symposia*, 2014, vol. 338, no. 1, pp. 96–107.
- [65] D. Ivaneyko, V. Toshchevnikov, and M. Saphiannikova, “Dynamic moduli of magneto-sensitive elastomers: a coarse-grained network model,” *Soft Matter*, vol. 11, no. 38, pp. 7627–7638, 2015.
- [66] D. Ivaneyko, V. Toshchevnikov, and M. Saphiannikova, “Dynamic-mechanical behaviour of anisotropic magneto-sensitive elastomers,” *Polymer*, vol. 147, pp. 95–107, 2018.
- [67] M. Cianchetti, C. Laschi, A. Menciassi, and P. Dario, “Biomedical applications of soft robotics,” *Nat. Rev. Mater.*, vol. 3, no. 6, pp. 143–153, 2018.
- [68] J. Yang *et al.*, “Development and evaluation of an MRE-based absorber with two individually controllable natural frequencies,” *Smart Mater. Struct.*, vol. 27, no. 9, p. 095002, 2018.

- [69] A. A. Lerner and K. A. Cunefare, "Performance of MRE-based vibration absorbers," *J. Intell. Mater. Syst. Struct.*, vol. 19, no. 5, pp. 551–563, 2008.
- [70] S. S. Sun *et al.*, "The development of an adaptive tuned magnetorheological elastomer absorber working in squeeze mode," *Smart Mater. Struct.*, vol. 23, no. 7, p. 075009, 2014.
- [71] S. Sun, H. Deng, J. Yang, W. Li, H. Du, and G. Alici, "Performance evaluation and comparison of magnetorheological elastomer absorbers working in shear and squeeze modes," *J. Intell. Mater. Syst. Struct.*, vol. 26, no. 14, pp. 1757–1763, 2015.
- [72] F.-L. Xin, X.-X. Bai, and L.-J. Qian, "Principle, modeling, and control of a magnetorheological elastomer dynamic vibration absorber for powertrain mount systems of automobiles," *J. Intell. Mater. Syst. Struct.*, vol. 28, no. 16, pp. 2239–2254, 2017.
- [73] J. Fu, M. Yu, X. M. Dong, and L. X. Zhu, "Magnetorheological elastomer and its application on impact buffer," in *J. Phys.: Conf. Ser.*, 2013, vol. 412, p. 012032.
- [74] A. A. Gurtovenko and A. Blumen, "Generalized gaussian structures: Models for polymer systems with complex topologies," in *Polymer Analysis Polymer Theory*, Springer, 2005, pp. 171–282.
- [75] J. D. Ferry, *Viscoelastic properties of polymers*. John Wiley & Sons, 1980.
- [76] W. Hu, G. Z. Lum, M. Mastrangeli, and M. Sitti, "Small-scale soft-bodied robot with multimodal locomotion," *Nature*, vol. 554, no. 7690, pp. 81–85, 2018.
- [77] H. Du, W. Li, and N. Zhang, "Semi-active variable stiffness vibration control of vehicle seat suspension using an MR elastomer isolator," *Smart Mater. Struct.*, vol. 20, no. 10, p. 105003, 2011.
- [78] C. Hirunyapruk, M. J. Brennan, B. R. Mace, and W. H. Li, "A tunable magnetorheological fluid-filled beam-like vibration absorber," *Smart Mater. Struct.*, vol. 19, no. 5, p. 055020, 2010.
- [79] A. Boczkowska, S. F. Awietjan, S. Pietrzko, and K. J. Kurzydłowski, "Mechanical properties of magnetorheological elastomers under shear deformation," *Compos. Part B Eng.*, vol. 43, no. 2, pp. 636–640, 2012.
- [80] M. Asadi Khanouki, R. Sedaghati, and M. Hemmatian, "Multidisciplinary Design Optimization of a Novel Sandwich Beam-Based Adaptive Tuned Vibration Absorber Featuring Magnetorheological Elastomer," *Materials*, vol. 13, no. 10, p. 2261, 2020.

- [81] S. Cesmeci, F. Gordaninejad, K. L. Ryan, and W. Eltahawy, "Design of a fail-safe magnetorheological-based system for three-dimensional earthquake isolation of structures," *Mechatronics*, vol. 64, p. 102296, 2019.
- [82] W. Li, K. Kostidis, X. Zhang, and Y. Zhou, "Development of a force sensor working with MR elastomers," in *2009 IEEE/ASME international conference on advanced intelligent mechatronics*, 2009, pp. 233–238.
- [83] A. D. Charles, A. N. Rider, S. A. Brown, and C. H. Wang, "Multifunctional Magneto-Polymer Matrix Composites for Electromagnetic Interference Suppression, Sensors and Actuators," *Prog. Mater. Sci.*, p. 100705, 2020.
- [84] R. W. Ogden, *Non-linear elastic deformations*. Courier Corporation, 1997.
- [85] O. Lopez-Pamies, "A new I1-based hyperelastic model for rubber elastic materials," *Comptes Rendus Mec.*, vol. 338, no. 1, pp. 3–11, 2010.
- [86] R. E. Rosensweig, *Ferrohydrodynamics*. Courier Corporation, 2013.
- [87] D. Jiles, *Introduction to magnetism and magnetic materials*. CRC press, 2015.
- [88] M. Asadi Khanouki, R. Sedaghati, and M. Hemmatian, "Characterization of Magneto-Mechanical Properties and Quasi-Static Physical Modelling of MR Elastomers," in *AIAA Scitech 2019 Forum*, 2019, p. 1114.
- [89] M. Lokander and B. Stenberg, "Improving the magnetorheological effect in isotropic magnetorheological rubber materials," *Polym. Test.*, vol. 22, no. 6, pp. 677–680, 2003.
- [90] U. R. Poojary and K. V. Gangadharan, "Integer and fractional order-based viscoelastic constitutive modeling to predict the frequency and magnetic field-induced properties of magnetorheological elastomer," *J. Vib. Acoust.*, vol. 140, no. 4, 2018.
- [91] A. Dargahi, S. Rakheja, and R. Sedaghati, "Development of a field dependent Prandtl-Ishlinskii model for magnetorheological elastomers," *Mater. Des.*, vol. 166, p. 107608, 2019.
- [92] T. H. Nam, I. Petříková, and B. Marvalová, "Experimental characterization and viscoelastic modeling of isotropic and anisotropic magnetorheological elastomers," *Polym. Test.*, vol. 81, p. 106272, 2020.
- [93] X. B. Nguyen, T. Komatsuzaki, and N. Zhang, "A nonlinear magnetorheological elastomer model based on fractional viscoelasticity, magnetic dipole interactions, and adaptive smooth Coulomb friction," *Mech. Syst. Signal Process.*, vol. 141, p. 106438, 2020.

- [94] V. P. Toshchevikov and Y. Y. Gotlib, “Shear dynamic modulus of nematic elastomers: modified Rouse model,” *Macromolecules*, vol. 42, no. 9, pp. 3417–3429, 2009.
- [95] J. Dutta, T. Chatterjee, and K. Naskar, “LDH as a multifunctional additive in EVA/TPU blends: Influence on mechanical, thermal, rheological and flame retardancy properties,” *Mater. Sci. Eng. B*, vol. 236, pp. 84–94, 2018.
- [96] Z. Parlak, T. Engin, and İ. Çalli, “Optimal design of MR damper via finite element analyses of fluid dynamic and magnetic field,” *Mechatronics*, vol. 22, no. 6, pp. 890–903, 2012.
- [97] Q.-H. Nguyen and S.-B. Choi, “Optimal design of a vehicle magnetorheological damper considering the damping force and dynamic range,” *Smart Mater. Struct.*, vol. 18, no. 1, p. 015013, 2008.
- [98] F. Imaduddin, S. A. Mazlan, and H. Zamzuri, “A design and modelling review of rotary magnetorheological damper,” *Mater. Des.*, vol. 51, pp. 575–591, 2013.
- [99] C. M. Elliott and G. D. Buckner, “Design optimization of a novel elastomeric baffle magnetorheological fluid device,” *J. Intell. Mater. Syst. Struct.*, vol. 29, no. 19, pp. 3774–3791, 2018.
- [100] Z. Dong, Z. Feng, Y. Chen, K. Yu, and G. Zhang, “Design and Multiobjective Optimization of Magnetorheological Damper considering the Consistency of Magnetic Flux Density,” *Shock Vib.*, vol. 2020, 2020.
- [101] M. Behrooz, X. Wang, and F. Gordaninejad, “Modeling of a new semi-active/passive magnetorheological elastomer isolator,” *Smart Mater. Struct.*, vol. 23, no. 4, p. 045013, 2014.
- [102] Lord Magnetorheological (MR) Store, “Data Sheet for MRF-132DG Magnetorheological Fluid,” Apr. 20, 2020. <http://www.lordmrstore.com/lord-mr-products/mrf-132dg-magneto-rheological-fluid> (accessed Apr. 20, 2020).
- [103] P.-B. Nguyen and S.-B. Choi, “A new approach to magnetic circuit analysis and its application to the optimal design of a bi-directional magnetorheological brake,” *Smart Mater. Struct.*, vol. 20, no. 12, p. 125003, 2011.
- [104] ASTM International, “Standard Specification for Standard Nominal Diameters and Cross-Sectional Areas of AWG Sizes of Solid Round Wires Used as Electrical Conductors.” ASTM International, 2018.

- [105] J. S. Grewal, R. Sedaghati, and E. Esmailzadeh, "Vibration analysis and design optimization of sandwich beams with constrained viscoelastic core layer," *J. Sandw. Struct. Mater.*, vol. 15, no. 2, pp. 203–228, 2013.
- [106] B. Nayak, S. K. Dwivedy, and K. Murthy, "Vibration analysis of a three-layer magnetorheological elastomer embedded sandwich beam with conductive skins using finite element method," *Proc. Inst. Mech. Eng. Part C J. Mech. Eng. Sci.*, vol. 227, no. 4, pp. 714–729, 2013.
- [107] M. Eshaghi, S. Rakheja, and R. Sedaghati, "An accurate technique for pre-yield characterization of MR fluids," *Smart Mater. Struct.*, vol. 24, no. 6, p. 065018, 2015.
- [108] D. J. Mead and S. Markus, "Loss factors and resonant frequencies of encastre damped sandwich beams," *J. Sound Vib.*, vol. 12, no. 1, pp. 99–112, 1970.
- [109] S. D. Sudhoff, *Power magnetic devices: a multi-objective design approach*. John Wiley & Sons, 2014.
- [110] "Web Page : Finite Element Method Magnetics." <https://www.femm.info/wiki/HomePage> (accessed Jan. 12, 2021).
- [111] K. A. Kalina, P. Metsch, and M. Kästner, "Microscale modeling and simulation of magnetorheological elastomers at finite strains: A study on the influence of mechanical preloads," *Int. J. Solids Struct.*, vol. 102, pp. 286–296, 2016.
- [112] E. Galipeau, S. Rudykh, G. deBotton, and P. P. Castañeda, "Magnetoactive elastomers with periodic and random microstructures," *Int. J. Solids Struct.*, vol. 51, no. 18, pp. 3012–3024, 2014.
- [113] H. R. Lusti, I. A. Karmilov, and A. A. Gusev, "Effect of particle agglomeration on the elastic properties of filled polymers," *Soft Mater.*, vol. 1, no. 1, pp. 115–120, 2002.

## Appendix A

In this section, average particle polarization is computed in terms of average flux density. As it has been presented in [51], all polarization of the MRE can be considered due to the polarization of the particles. Therefore, B-H relation in a material can be written as:

$$\mu_0 H = B - \phi J_p \quad (\text{A.1})$$

where  $\mu_0 = 4\pi \times 10^{-7}$  is the vacuum permeability.  $J_p$  is the average polarization density of the particles and may be calculated by performing integration over half volume of a particle and regarding both saturated and unsaturated regions inside a particle:

$$J_p = \frac{1}{v_0/2} \left( \int J_x dV_x + \int J_s dV_s \right) = \frac{1}{\frac{2}{3}\pi r^3} \left( \int_0^{r_s} J_x \pi(r^2 - x^2) dx + \int_{r_s}^r J_s \pi(r^2 - x^2) dx \right) \quad (\text{A.2})$$

where,  $\frac{v_0}{2} = \frac{2}{3}\pi r^3$  stands for the half of a particle volume, and  $J_s$  is the saturation polarization of the particles.  $J_x$  is the polarization density at a distance  $x$  within the unsaturated region of the particle. Neglecting the reluctance of the unsaturated portion of the particle compared to that of the saturated region ( $B_s \approx J_s + \mu_0 H$ ) and substituting  $J_x = \frac{(r^2 - r_s^2)}{(r^2 - x^2)} B_s$ , Eq. (A.1) can be written as follows:

$$\mu_0 H = B - \frac{3\phi}{2r^3} \left( (J_s + \mu_0 H) \int_0^{r_s} (r^2 - r_s^2) dx + J_s \int_{r_s}^r (r^2 - x^2) dx \right) \quad (\text{A.3})$$

Performing integrations in Eq. (A.3) and using  $\alpha = r_s/r$  in the formulation yields:

$$\mu_0 H = \frac{B - \phi(1 - \alpha^3)J_s}{1 + \frac{3\phi}{2}(\alpha - \alpha^3)} \quad (\text{A.4})$$

By substituting Eq. (A.1) into Eq. (A.4), the average particle polarization density can be simply obtained as:

$$J_p = \frac{\frac{3}{2}(\alpha - \alpha^3)B + (1 - \alpha^3)J_s}{1 + \frac{3}{2}\phi(\alpha - \alpha^3)} \quad (\text{A.5})$$

In this equation, particle polarization,  $J_p$ , is obtained based on the averaged flux density,  $B$ . In [51], Eq. (A.4) and (A.5) were presented as follows:

$$\mu_0 H = \frac{B - \phi(1 - \alpha^3)J_s}{1 + \frac{3\phi}{2}\alpha^3} \quad (\text{A.6})$$

$$J_p = \frac{\frac{3}{2}\alpha^3 B + (1 - \alpha^3)J_s}{1 + \frac{3}{2}\phi\alpha^3} \quad (\text{A.7})$$

which are different from the derivation presented above. It seems that a minor mistake is occurred in [51] for integrations of Eq. (A.3) and derivation of the particle polarization,  $J_p$ . Considering that the MRE samples with various volume fraction of particles will saturate at different levels of magnetic induction as discussed in the Section 2.2.2, in the present study the coefficient of the saturation polarization is used to correct the saturation polarization of the MREs with respect to the volume fraction of CIPs. Therefore, Eq. (A.5) is modified as Eq. (2.19).



## Appendix B

In this appendix, required formulation for magnetic analysis of the C- and U-shaped electromagnets is provided, similar to the equations developed for the H-shaped electromagnet in Section 4.5. Parameters have the same meaning as in the case of H-shaped electromagnet unless otherwise mentioned.

For the C-shaped electromagnet, according to Figure 4.2 (b), since there is only one closed loop in the path of magnetic flux without any node, the amount of flux is constant around the loop. In addition, Equation (4.31) could be written for the C-shaped electromagnet in the following format:

$$N_{c1}I + N_{c2}I + N_{c3}I = H_{core}l_{core} + H_{gap}l_{gap} \quad (B.1)$$

The number of turns of wire in the coils of the electromagnet can be estimated as:

$$N_{c1} = N_{c2} = \frac{cd}{2D^2} \quad (B.2)$$
$$N_{c3} = \frac{d(2c + g)}{2D^2}$$

In addition, the total mass of the electromagnet can be formulated as:

$$M_{el} = \frac{\pi}{4}D^2L_w\rho_w + V_{sc}\rho_{sc} \quad (B.3)$$

where  $L_w$  and  $V_{sc}$  could be found with the following relations:

$$L_w = \frac{2cd}{D^2}(t + t + d) + \frac{d(2c + g)}{D^2}(t + t + d) \quad (B.4)$$

$$V_{sc} = t((2t + d)(2t + 2c + g) - d(2c + g) - gt) \quad (B.5)$$

Similar to what was presented for the H-shaped electromagnet in Figure 4.10, here, the FE magnetic analysis for the C-shaped electromagnet, performed by the FEMM software, is demonstrated in Figure B.1. The input current to the coil is set at 5 A. The considered C-shaped electromagnet has dimensions of  $c = d = t = 2$  cm and a gap of  $g = 0.5$  cm.

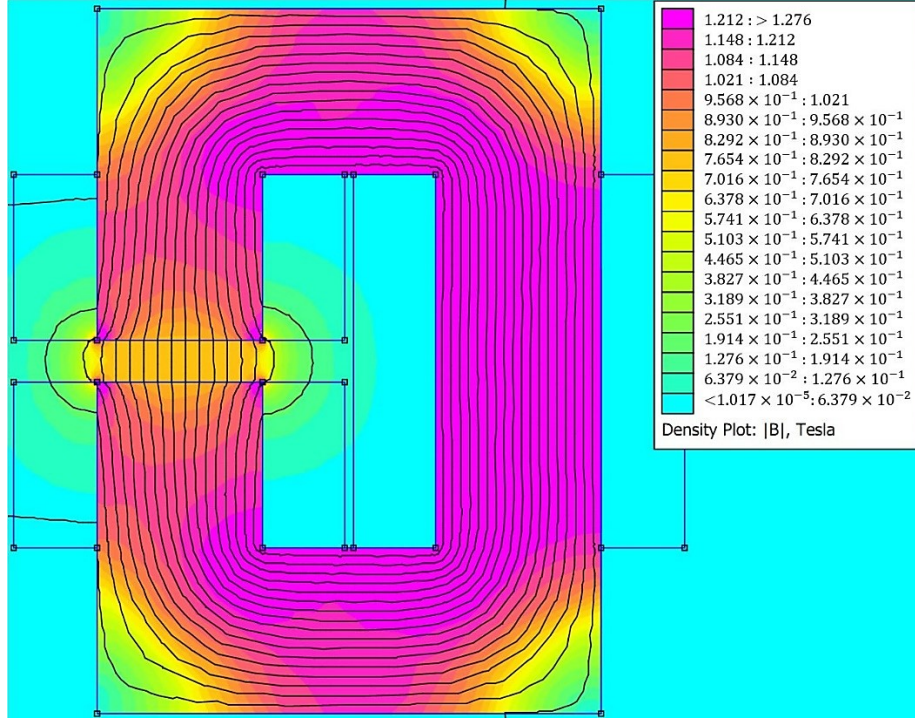


Figure B.1. Magnetic flux distribution for the C-shaped electromagnet using FEMM software.

Results of magnetic flux density at the center of the gap has also been calculated using both analytical model (Equations (B.1) to (B.5)) and FE analysis (with FEMM software) for different applied currents. Table B.1 shows the comparison of the results for the C-shaped electromagnet.

Table B.1. Comparison of flux density values at the center of the air gap of the C-shaped electromagnet obtained by analytical magnetic circuit model (Equations (B.1) to (B.5)) and FE model.

Input Current (A)	Flux Density (mT)		Error%
	Analytical Magnetic Circuit Model Equations (B.1) to (B.5)	Flux Density (mT) FE Analysis	
2.5	394	400	1.50
3	474	480	1.25
3.5	554	560	1.07
4	635	645	1.55
4.5	716	726	1.38
5	798	806	0.99

For the U-shaped design, considering the U-shaped electromagnet as in Figure 4.2 (c), the analytical magnetic model can be presented with the following equations:

$$N_{c1}I + N_{c2}I + N_{c3}I + N_{c4}I = H_{core}l_{core} + H_{gap}l_{gap} \quad (B.6)$$

The number of turns of wire in the coils of the electromagnet can be found as:

$$N_{c1} = N_{c2} = N_{c3} = N_{c4} = \frac{cd}{2D^2} \quad (\text{B.7})$$

Moreover, the total mass of the electromagnet can be formulated as:

$$M_{el} = \frac{\pi}{4}D^2L_w\rho_w + V_{sc}\rho_{sc} \quad (\text{B.8})$$

where length of wire  $L_w$  and volume of the steel core  $V_{sc}$  could be found with the following relations:

$$L_w = \frac{4cd}{D^2}(t + t + d) \quad (\text{B.9})$$

$$V_{sc} = 2t((2t + d)(c + t) - cd) \quad (\text{B.10})$$

Figure B.2 shows the FE magnetic analysis for the U-shaped electromagnet, performed by the FEMM software when the input current to the coil is set at 5 A.

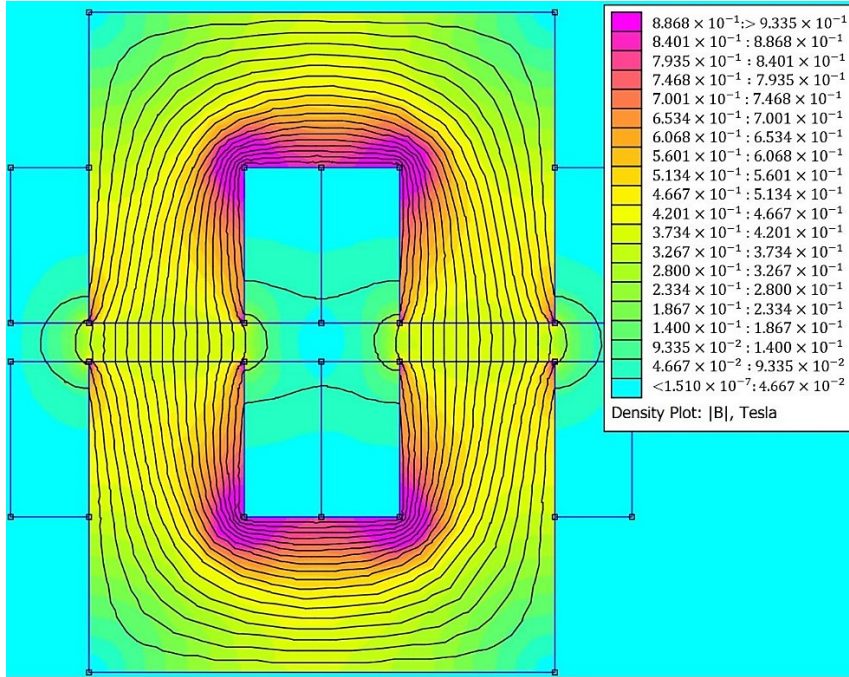


Figure B.2. Magnetic flux distribution for the U-shaped electromagnet using FEMM software.

In addition, the results of magnetic flux density at the center of the gap calculated by utilizing both analytical model (using Equations (B.6) to (B.10)) and FE analysis (with FEMM software) for different input currents are shown in Table B.2 for the U-shaped electromagnet.

Table B.2. Comparison of the flux density values at the center of the air gap of the U-shaped electromagnet obtained by analytical magnetic circuit model (Equations (B.6) to (B.10)) and FE model.

Input Current (A)	Flux Density (mT)		Error%
	Analytical Magnetic Circuit Model Equations (B.6) to (B.10)	Flux Density (mT) FE Analysis	
2.5	189	190	0.53
3	226	228	0.88
3.5	264	266	0.75
4	302	304	0.66
4.5	339	341	0.59
5	377	379	0.53